UNIVERSITY OF ROCHESTER
LABORATORY FOR LASER ENERGETICS

Volume 65
October–December 1995
DOE/SF/19460-117

LLE Review

Quarterly Report

UR
LLE

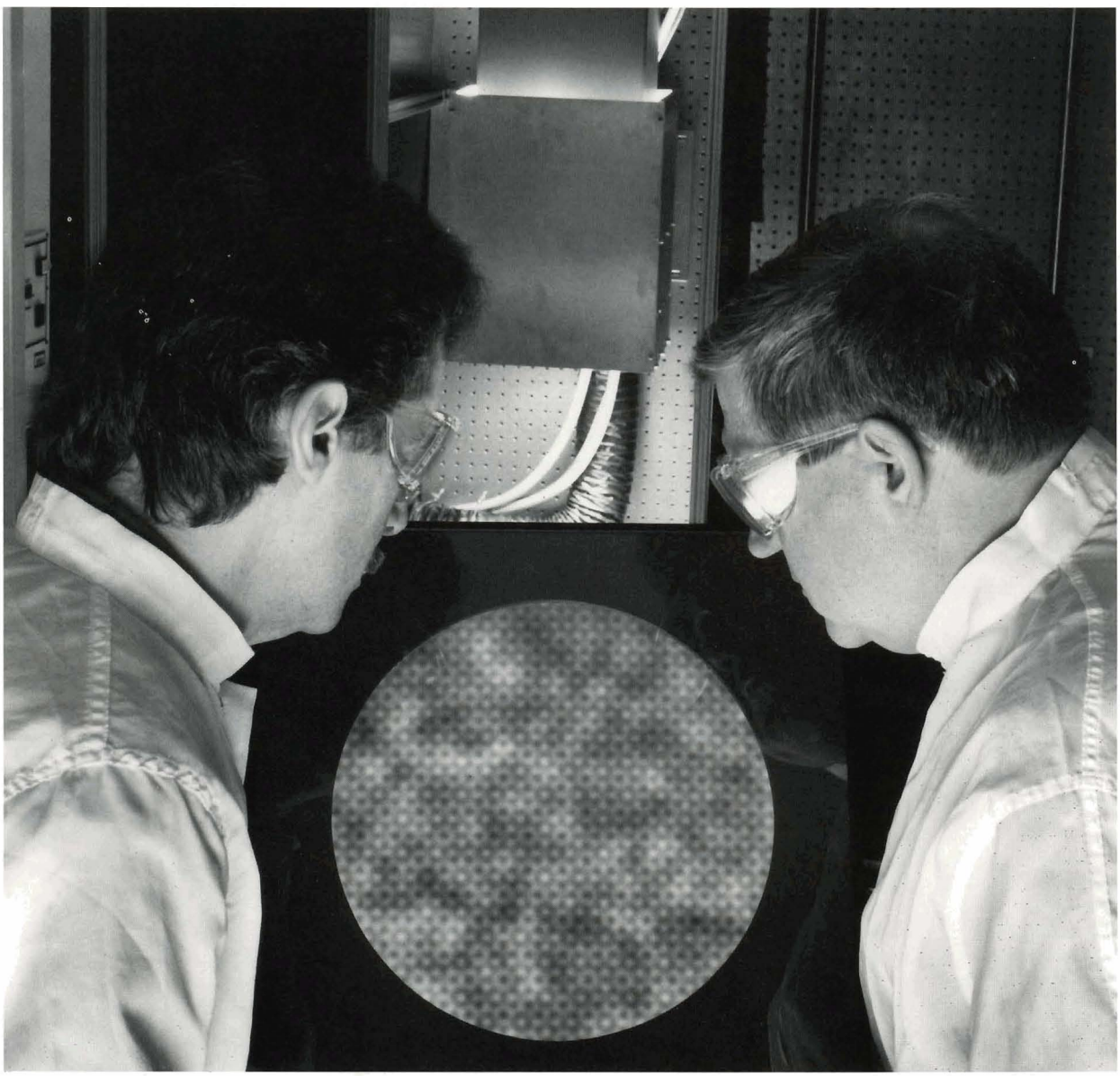

About the Cover:

Joe Barone (left) and Larry Iwan, members of the Optics and Imaging Sciences Group at LLE, examine a large-aperture photographic mask used to fabricate distributed phase plates (DPP's) for the OMEGA laser system. DPP's play a key role in the OMEGA experimental program. By modifying the spatial coherence of the individual UV beams, the DPP's increase the on-target irradiation uniformity and make possible other uniformity enhancements.

The work described in this volume includes current research at the Laboratory for Laser Energetics, which is supported by New York State Energy Research and Development Authority, the University of Rochester, the U.S. Department of Energy Office of Inertial Confinement Fusion under Cooperative Agreement No. DE-FC03-92SF19460, and other agencies.

Printed in the United States of America
Available from
National Technical Information Services
U.S. Department of Commerce
5285 Port Royal Road
Springfield, VA 22161

Price codes: Printed Copy A04
Microfiche A01

For questions or comments, contact Thomas R. Boehly, *Editor*, Laboratory for Laser Energetics, 250 East River Road, Rochester, NY 14623-1299, (716) 275-0254.

UNIVERSITY OF ROCHESTER
LABORATORY FOR LASER ENERGETICS

Volume 65
October–December 1995
DOE/SF/19460-117

LLE Review

Quarterly Report

Contents

In Brief

This volume of the LLE Review, covering the period October–December 1995, contains a description of the generation and characterization of continuous, deep-surface-relief phase plates that are more efficient and versatile than previous designs. The LLE program plan has scheduled a number of enhancements to OMEGA's performance and uniformity, the first of which is the implementation of these new distributed phase plates. Other articles in this volume include the discussion of an x-ray diagnostic method to measure shell-fuel mixing, the theoretical analysis of ablation-front stability, a description of a major subsystem in the OMEGA control system software, a study of the population inversions in intensely pumped Nd:YLF, and a description of a new ultrafast laser system and its uses.

Highlights of the research presented in this issue are

- New continuous phase plates have been manufactured and characterized for use on the OMEGA laser system. These components have demonstrated the ability to couple up to 25% more energy to the target than previous designs, and to operate over a wider range of target diameters.

- A method is proposed to diagnose shell-fuel mixing using x-ray spectroscopy. Emission and absorption lines from dopant material, localized in the target shell, diagnose the extent that shell material has mixed with the fuel of an imploded target.

- Analytic calculations of the stability of ablation fronts subjected to the Rayleigh-Taylor instability are presented. This model assumes an arbitrary power-law dependence of the electron thermal conduction, thus allowing application to both direct and indirect drive. Excellent agreement is demonstrated between the model's growth-rate formula and numerical results for a variety of conditions.

- One of the top-level subsystems in the new control system for the OMEGA laser is the Power Conditioning Executive—the software that controls the power conditioning hardware. It provides interface to the system operators and is responsible for the safe and reliable execution of laser shots.

- To simulate and investigate the intense pumping associated with diode-pumped lasers, a pump-probe experiment has been performed. The results show that, at high population inversions, two-body energy transfer upconversion (ETU) can be a significant loss mechanism for the $^4F_{3/2}$ upper state of the Nd:YLF laser.

- Using commercially available subsystems, a Ti:sapphire laser system has been configured to produce ultrashort pulses that are tunable to a wide region. Using nonlinear optical conversion processes, femtosecond pulses have been produced in the spectral range from the ultraviolet to the infrared, including terahertz pulses. These pulses have been used to perform ultrafast measurements of solid-state media used in optics, electro-optics, and electronics.

Thomas R. Boehly
Editor

High-Efficiency Distributed Phase Plate Generation and Characterization

An essential requirement for both direct-drive and indirect-drive laser fusion is the uniform irradiation of targets that are located at the far field and quasi far field of the laser system. Higher uniformity results in reduced Rayleigh-Taylor instabilities and improved spherical convergence of fuel capsules during high-density compression. For high-power, solid-state laser drivers, a major contribution to irradiation nonuniformity is the intensity distribution of the individual frequency-tripled beams at the target plane. The irradiance nonuniformities are caused primarily by spatial variations in the near-field phase front that accumulate as the pulse propagates through the air and laser optics. Optical phase conversion at the end of a laser system, using distributed phase plates (DPP's),[1] modifies the beam's field coherence, thereby changing its focusing properties and shifting energy toward the higher spatial frequencies that can be rapidly blurred using temporal beam-smoothing techniques.

In the past, the price of this coherence control was a loss of 20%–25% of the laser energy. The primary goal in the design of a new phase converter is to achieve lossless, wavefront-insensitive, phase conversion. This has been recently achieved with a new variety of DPP (continuous, deep-surface-relief phase plates) that has been generated and characterized for use in the 60-beam OMEGA laser system. The two-level binary phase plates previously deployed on the 24-beam OMEGA laser system provided coherence control but had significant losses and operated over a narrow range in the focal direction. These new continuous DPP's perform nearly lossless phase conversion of high-power laser beams,[2,3] providing a coupling efficiency to target of $\gtrsim$95%. They also operate over the full range of target diameters planned for the LLE experimental fusion-physics program.

OMEGA DPP Requirements

The requirements for this new generation of DPP's are high transmission to the target, a weak super-Gaussian irradiance profile, and operation over a range of target sizes. They must be significantly more efficient than the previous two-level DPP's whose overall coupling efficiency was limited to 78%. Of that lost energy (22%), 16% was due to diffraction rings produced by the edges of the binary elements. The goal was to retrieve all of this energy by implementing continuous features on the phase plates, thereby eliminating the diffraction loss. This would result in DPP's that have to-target transmission efficiencies of 94%–96%. The DPP design should provide an intrinsic efficiency of 100%; however, some loss is allowed to accommodate both alignment and manufacturing tolerances. Of the remaining 4% to 6% energy loss, approximately 3.5% must be allocated to beam-to-target alignment tolerances. Therefore, additional energy losses associated with the manufacturing process, such as surface scatter and reflection, must be limited to less than 2.5% of the incident energy.

The required irradiance envelope produced by the DPP's is mathematically represented by a rotationally symmetric supergaussian of order between 2 and 3. (An order 2 produces a Gaussian distribution.) It is also desired that the DPP provide the relatively flat power spectrum characteristic of the previous two-level DPP's. When these distributions are overlapped on a target, the amplitudes of the low- to mid-range modes ($\lambda > 20\ \mu$m) should not exceed the extremes produced by random statistics. High spatial frequencies ($\lambda < 20\ \mu$m) are less detrimental because of their fast smoothing times in the presence of temporal beam smoothing.

The DPP must also provide an irradiance distribution that adequately integrates over the full aperture of the input pupil so that the spectral modes, produced by spatial color cycling, overlap at the target plane. DPP's containing Fourier gratings inherently meet this requirement when used at or near the focal plane of a lens. Finally, the new DPP must provide the above efficiency, irradiance, power spectrum, and temporal beam-smoothing capability for target diameters ranging from 800 to 1000 μm. On OMEGA this necessitates operation in a range of ±4 mm along the optical axis of the lens.

Phase-Plate Concept

To achieve both high efficiency and the desired profile at the target plane, the continuous DPP was designed with a

specific combination of a Fourier grating phase plus a random phase. Produced by the surface relief on such a DPP, the phase consists of a random term combined with several spatially periodic terms. These two terms are superposed on a single surface but are shown in Fig. 65.1 on either side of a plate for clarity only. The purpose of the spatially periodic terms, or Fourier grating terms, is to diffract the collimated incident beam into multiple orders or multiple beamlets.[2] These orders are collected by the lens to form an array of foci at the Fourier plane of the lens. The lateral separation of these foci (d^*) can be expressed in terms of the wavelength λ of light used, the f number ($f_{\#}$) of the focusing lens, and the number of grooves or elements in the grating, N:

$$d^* = \lambda N f_{\#} = \frac{\lambda N f}{D} = \frac{\lambda f}{d}, \tag{1}$$

where N is equal to the diameter of the grating (D) divided by the groove spacing (d); $N = D/d$. The Fourier gratings separate an incident laser beam into a two-dimensional angular spectrum of beamlets that focus at the focal plane of a lens. As a result, the interference pattern produced by the coherent overlap of the beamlets depends primarily on the phase transfer function of the distributed phase plate rather than the wavefront of a typical laser beam.

In the simplest case, the surface-relief profile of a DPP can be composed of several sinusoidal components together with a random component. The phase retardation is distributed over the DPP surface by introducing optical path differences (OPD's) in the form of a thin film of varying thickness $t(x,y)$ and material refractive index n. The exact amount of phase retardation ϕ experienced by a transmitted wavefront depends upon the wavelength (λ) of light and is given by

$$\phi = \frac{2\pi}{\lambda}(\mathrm{OPD}) = \frac{2\pi}{\lambda}\left[t(x,y)(n-1)\right]. \tag{2}$$

Optical modeling shows that the energy coupled to a target using the new continuous distributed phase plate is substantially greater than that using a two-level binary phase plate as shown in Fig. 65.2. To allow for small beam and target misalignments, approximately 3.5% of the incident energy misses the target. This energy is accessible with the penalty of lower irradiation uniformity. Underfilling a spherical target causes an increase in the amplitude of medium-order spherical harmonic modes. Nevertheless, an increase in energy efficiency from 78% to 96% represents a 20%–25% increase in total energy delivered to the target. Simulations have shown that phase conversion with our new continuous DPP's meets the design requirements over a sufficiently long depth of focus to accommodate a wide range of target diameters.

DPP Generation

Optical lithography is an excellent means of generating complex surface-relief structures that subsequently can be replicated into polymers that are compatible with high-irradiance UV laser light. Using a combination of photographic and photolithographic techniques, both mask fabrication and photoresist patterning have been successfully demonstrated at

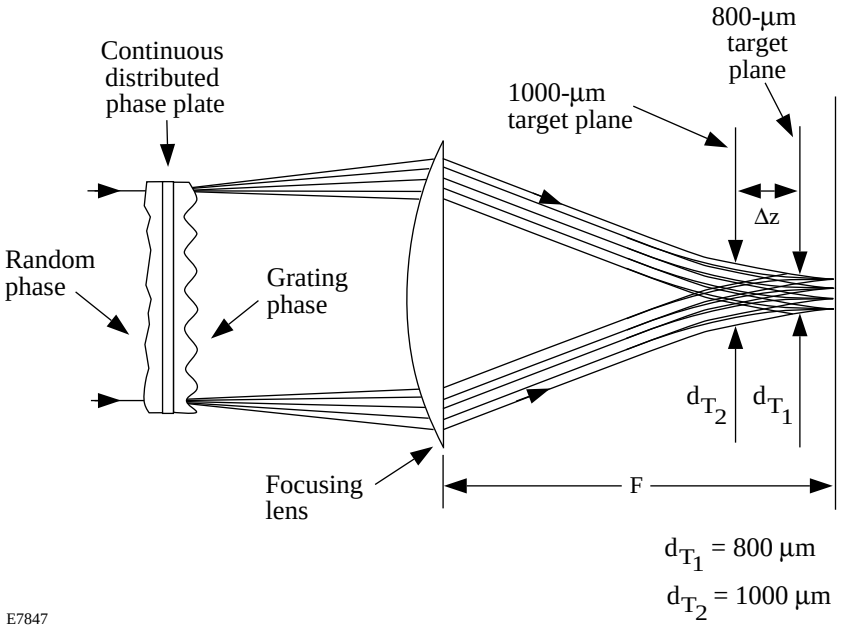

Figure 65.1
The surface of a continuous distributed phase plate consists of a random term combined with several periodic terms. These produce an irradiance distribution at the focal plane of a lens that efficiently couples laser light to targets in the range of 800 to 1000 μm in diameter. The two phase terms are shown on either side of the substrate for clarity only.

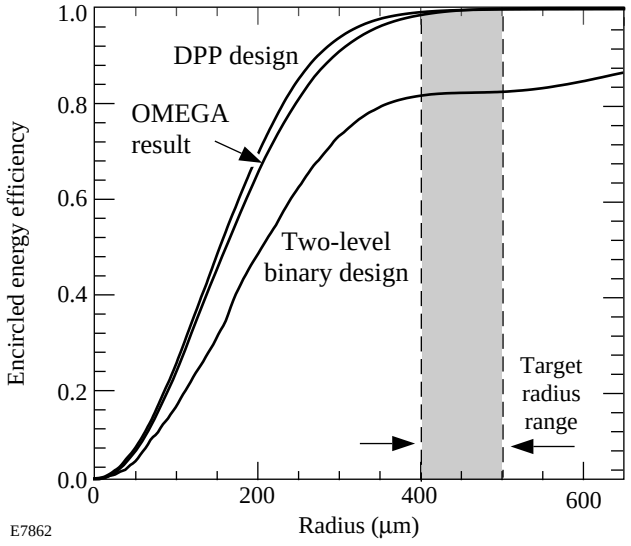

Figure 65.2
The energy coupled to a target using a continuous distributed phase plate is substantially greater than that using a two-level binary phase plate. Approximately 4% of the incident energy is distributed around the target to allow for minor beam and target misalignments. An increase in energy efficiency from 78% to 96% represents a 20%–25% increase in total energy delivered to the target.

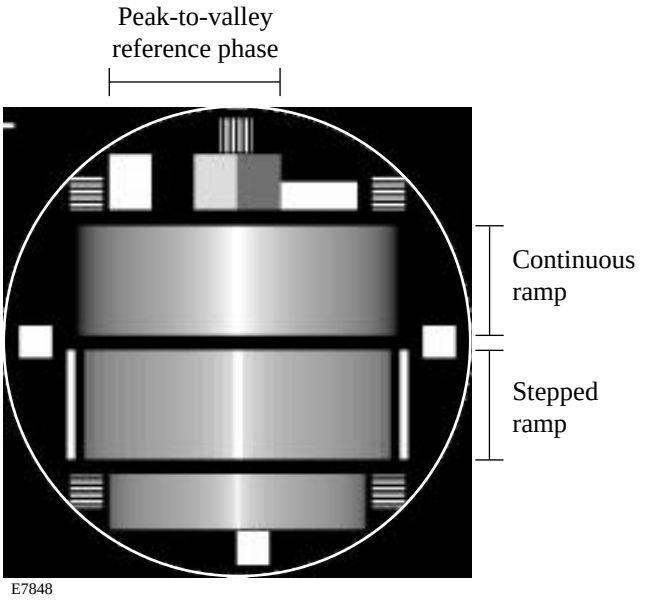

Figure 65.3
The calibration mask is a sheet of photographic film containing both continuous and stepped regions of varying density whose corresponding transmittance functions are used to characterize the linearity of the photolithographic process. A 9-in. enlargement made from a computer-generated, 35-mm negative is produced using standard silver-halide processing techniques.

LLE, resulting in the fabrication of 310-mm-diam continuous DPP's suitable for use in OMEGA.

The photolithographic process begins with the calibration of a Celco photographic-film writer, using, as a reference, the interferometric measurement of a test phase plate made in photoresist. The calibration mask used in this stage is a sheet of photographic film containing both continuous and stepped regions of varying density whose transmittance functions are used to characterize the linearity of the photolithographic process. An enlargement made from a computer-generated, 35-mm negative, shown in Fig. 65.3, is produced using standard silver-halide processing techniques. Following the chemical processing of the photoresist, Fizeau interferometry is used to characterize the optical path differences within the photoresist phase plate. The interference fringes, shown in Fig. 65.4, are computer analyzed to examine linearity of the transfer from mask transmittance to phase difference in the photoresist. These results are used to generate an end-to-end process inversion curve.

The final inversion curve, shown in Fig. 65.5, relates the Celco film writer's code values to the range of phase differences required in the DPP design. The inversions contained in

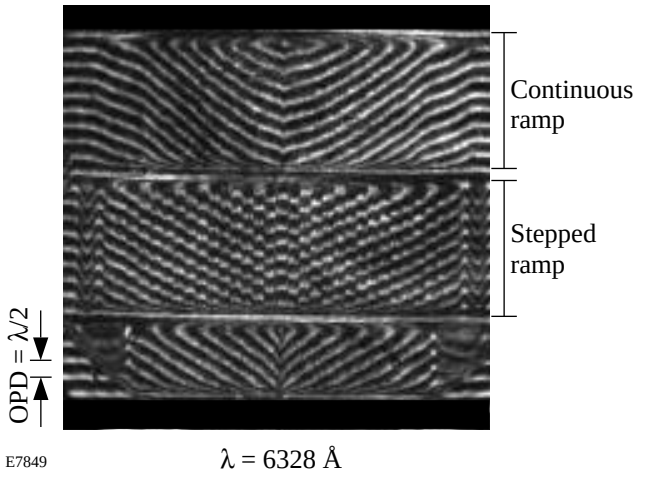

Figure 65.4
Fizeau interferometry is used to characterize the optical path differences that are photolithographically generated in a photoresist coating using the calibration mask shown in Fig. 65.3. The interference fringes are computer analyzed to examine linearity of the transfer from mask transmittance to photoresist phase difference.

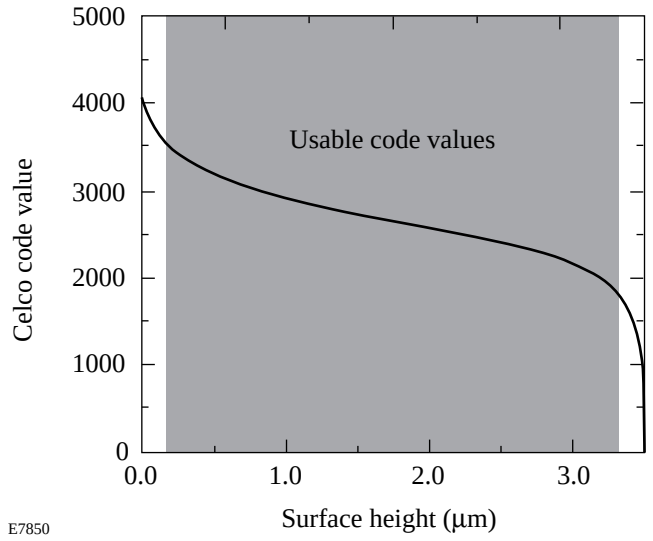

Figure 65.5
The final inversion curve relates the code values for the Celco film writer to the range of phase differences required in the DPP design. The multiple inversions contained in this final curve include nonlinearities in the film writer, recording film, enlargement film, and photoresist. Several iterations were required to yield a sufficiently linear relationship between the desired phase differences and the actual phase difference realized in the surface relief of the photoresist.

this final curve include the nonlinearities in the film writer, recording film, enlargement film, and photoresist. Several iterations were required to yield a sufficiently linear relationship between the desired phase differences and those produced in the surface relief of the photoresist. The mask used to generate the desired DPP surface relief is shown in Fig. 65.6. It is a sheet of silver halide film containing the distribution of densities that follow the range established by the previous calibration process. The mask transmittance function times the material removal function of the photoresist is linearly related to the phase difference produced in the DPP design.

Interferometric analysis of the DPP master is performed by positioning the edge of the master in a single-pass Mach-Zehnder interferometer. Spatial synchronous phase detection is used to analyze the high-frequency fringes that extend from the region of thick photoresist to the region of thin photoresist. Low-frequency fringes are shown in Fig. 65.7(a) to help the reader visualize the phase shifts. The peak-to-valley optical path difference, shown in Fig. 65.7(b), corresponds to the maximum phase difference contained in the photoresist DPP master.

The final steps to generate DPP's for the OMEGA laser system involves the transfer, or replication, of the surface relief into a suitable UV-compatible material. After extensive development of release mechanisms, the replication of photoresist

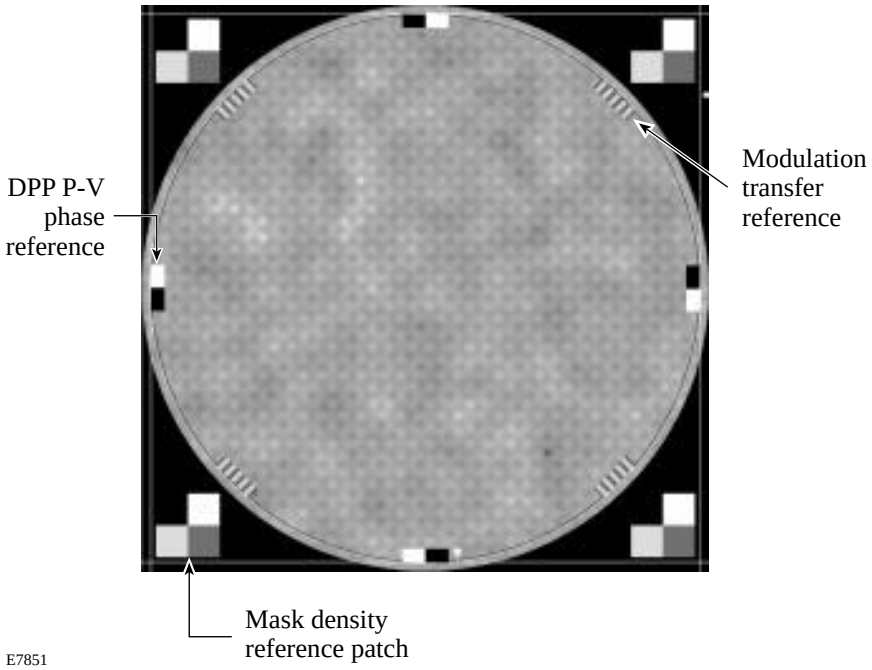

Figure 65.6
The mask used to generate the desired DPP surface relief is a sheet of photographic silver halide film containing a density distribution whose transmittance function follows the range established by the previous calibration iteration. The mask transmittance function times the material removal function of the photoresist is linearly related to the phase difference required in the DPP design.

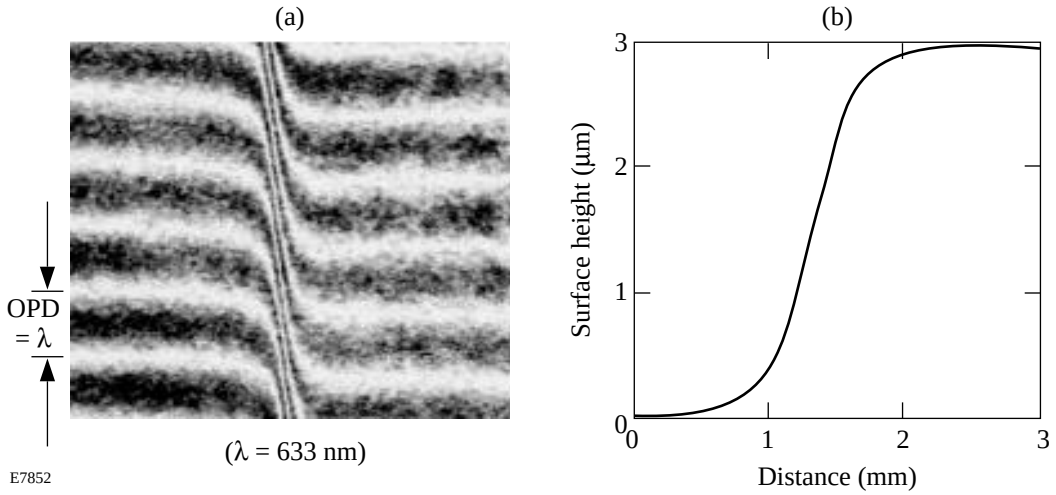

Figure 65.7
Interferometric analysis of the DPP master is performed by positioning the edge of the master within a single-pass Mach-Zehnder interferometer. Spatial synchronous phase detection is used to analyze the high-frequency interference fringes that extend from the region of thick photoresist to the region of thin photoresist. Low-frequency fringes are shown in (a) for clarity. The peak-to-valley optical path difference (b) measured here corresponds to the maximum phase difference contained in the DPP phase distribution.

masters into a UV epoxy succeeded using an evaporative-coating release-layer technology borrowed from the industrial sector.[4] The fabrication of DPP's is performed in class 100 to 1000 clean-room conditions to limit contamination that can cause losses due to surface-relief scattering, material scattering, and material absorption.

DPP Characterization

The on-target irradiation distribution from a single focused laser beam is measured with equivalent-target-plane photographic cameras. Experimental results from these cameras are shown in Fig. 65.8. Each element within the array represents the same spatial image recorded at successively lower exposures. Figure 65.8(a) shows a focal-spot distribution produced by a two-level binary phase plate, while Fig. 65.8(b) shows the more efficient pattern produced by the new continuous DPP. Note that the diffraction lobes are absent from the spot produced by the continuous DPP. These images were density-to-irradiance converted using a calibration curve derived from the known changes in exposure between images of each array. As can be seen in Fig. 65.9, a dynamic range of 10^4 is then obtained. This range is required to accurately measure the high-contrast speckle produced by phase conversion of the laser beam.

A photographic image generated with cw laser light [Fig. 65.10(a)] is compared with that from a beamline of the OMEGA laser system [Fig. 65.10(b)]. Although the wavelength of the cw (364-nm) laser is different than the OMEGA laser (351 nm), compensating diffractive and refractive effects

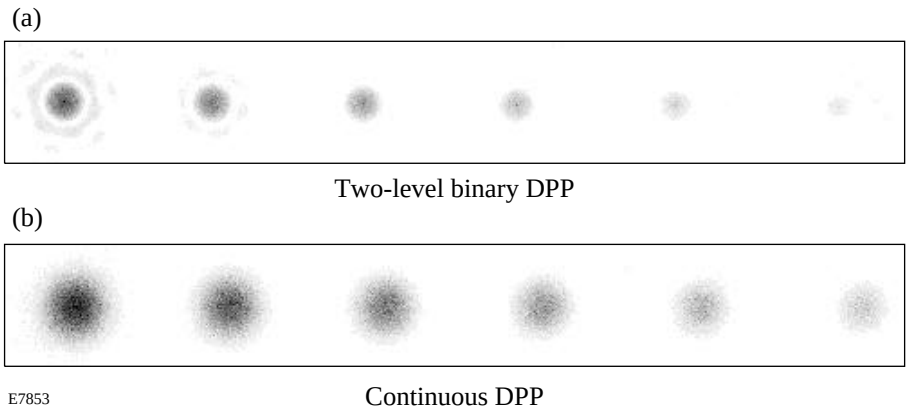

Figure 65.8
The on-target irradiation distribution from a single focused laser beam is measured with an equivalent-target-plane photographic camera. Each element within the array represents the same spatial image recorded at successively lower exposures. Figure 65.8(a) shows the lossy diffraction lobes produced by a two-level binary phase plate, while Fig. 65.8(b) shows the more efficient pattern produced by the new continuous DPP.

cause these results to be essentially equivalent. Orthogonal scans through the center of an equivalent-target-plane image show the irradiance modulation that is characteristic of laser speckle. The dominant visual characteristic for these phase plates is the random variation in irradiance, which obeys negative exponential statistics. Figures 65.11(a) and 65.11(b) show horizontal and vertical cross sections of the irradiance, respectively, for the OMEGA beam shown in Fig. 65.10(b). An individual cross section can contain a peak-to-average irradiance ratio of several hundred percent; however, only a small fraction of the total energy resides in these modulations. Figure 65.12 shows the total energy contained within a circle surrounding the center of the beam as a function of the radius of that circle. This is referred to as an encircled energy plot. Curve A is an experimental cw result, curve B is an experimental pulsed result, curve C is the result of theoretical calculation, and curve D is the desired encircled energy profile for the irradiation for direct-drive targets. Good agreement between these curves, near the 400-μm radius, indicates that a useful, highly efficient DPP has been generated.

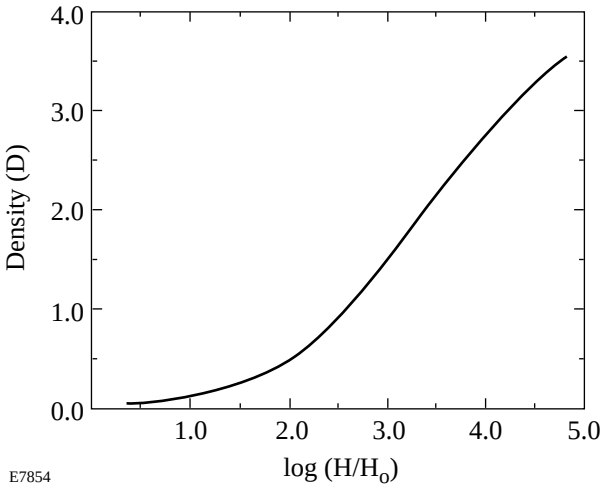

Figure 65.9
The photographic images generated by the equivalent-target-plane camera are density-to-irradiance converted using a calibration curve derived from the array of images. A dynamic range of 10^4 is obtained to accurately measure the high-contrast speckle produced by phase conversion of the laser beam.

Extensive testing of the DPP far-field performance is performed to ensure that accurate focusing can be accomplished on the OMEGA laser system. In addition to the photographic analysis described above, energy-transfer measurements are made by translating target-sized apertures along the optical axis. These measurements are used to determine both the minimum spot size and the energy-transfer efficiency of the DPP. Equation (3) shows the functional form of the relationship between target diameter and focal shift for a given DPP-specific minimum spot and a desired encircled energy on target:

$$\Delta Z_T = 6.429\left(D_m\right)\left[\left(\frac{D_T}{D_m}\right)^{N\left(E_c\right)} - 1\right]^{1/N\left(E_c\right)} + \Delta Z_p \ , \quad (3)$$

where D_m = minimum beam diameter containing E_c; D_T = target diameter (800 to 1000 μm); E_c = encircled energy on target; $N(E_c)$ = calculated order; and ΔZ_p = power-induced focal shift. The minimum spot size (D_m) is used in Eq. (3) to provide the correct position of the focus lens given a desired target diameter and a specific encircled energy. A limited amount of defocus can be used to compensate for DPP

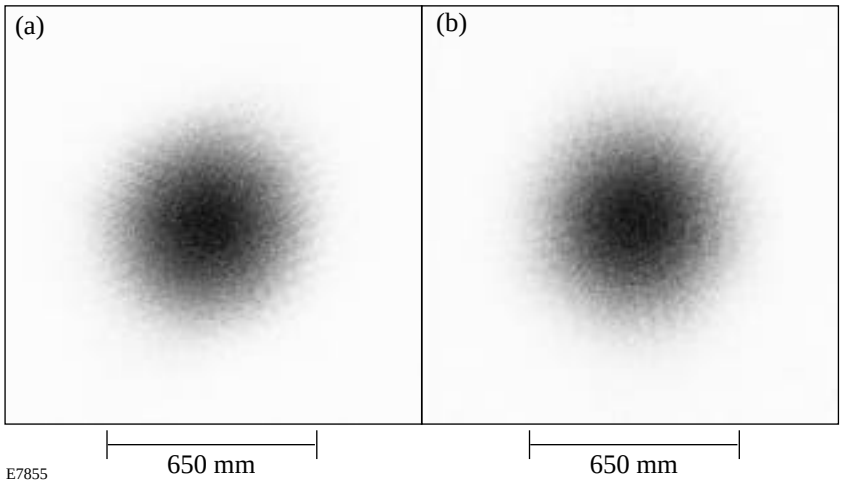

Figure 65.10
(a) The photographic image generated with cw laser light is compared with (b) that from a beamline of the OMEGA laser system. Although the wavelength of the cw (364-nm) laser is different than the 351-nm OMEGA laser, compensating diffractive and refractive effects cause these results to be essentially equivalent.

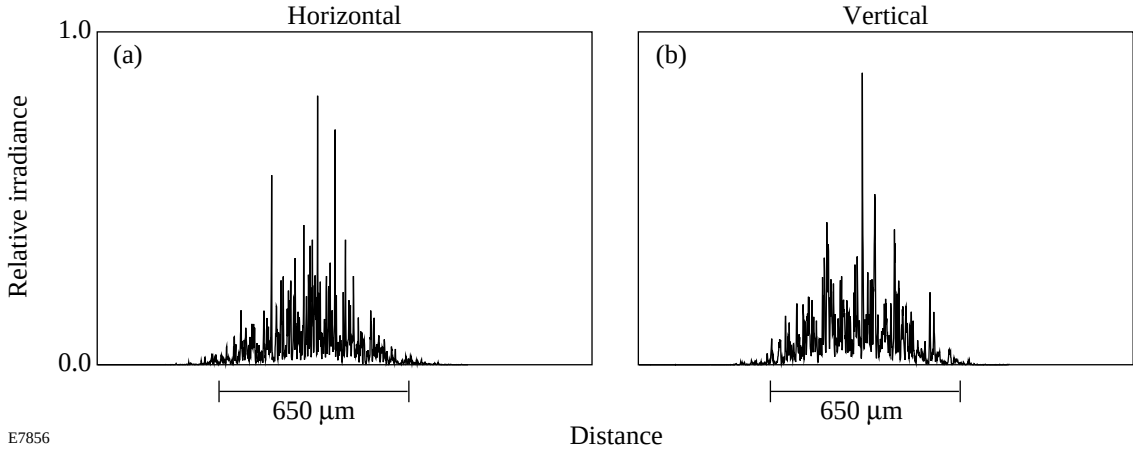

Figure 65.11
Orthogonal scans through the center of an equivalent-target-plane image show the irradiance modulation characteristic of laser speckle. Figures 65.11(a) and 65.11(b) show horizontal and vertical cross sections of the irradiance, respectively. An individual cross section can contain a peak-to-average irradiance ratio of several hundred percent; however, only a small fraction of the total energy is contained in these peaks.

phase undermodulation, thus providing a favorable manufacturing tolerance.

The family of hyperbolic curves shown in Fig. 65.13 represent a specific case of Eq. (3). The radius of the contour containing 96.6% of the energy is plotted as a function of the focus lens position along the optical axis. Minimum spot sizes of between 675 and 750 μm are represented here. The gradient of the curve in the vicinity of an 800-μm target is approximately a change in diameter of 10 μm per 100 μm of focal shift. Additional families of hyperbolic curves can be generated to allow flexibility in choosing an encircled energy on target; the limits, however, are the amount of energy that misses the target and the overall irradiation uniformity. A coupling efficiency of 96.6% (incident light that irradiates the target) is a compromise between these constraints.

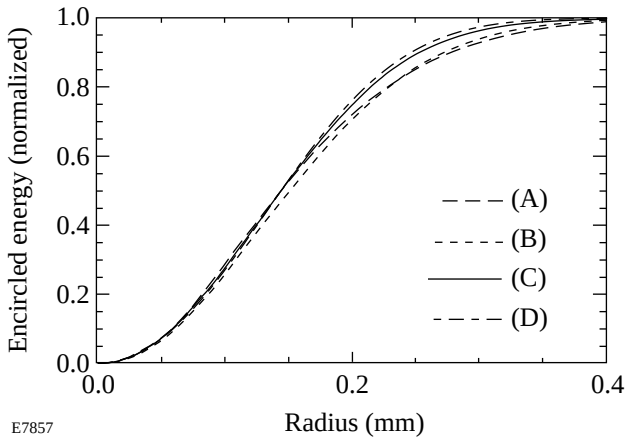

Figure 65.12
The total energy contained within a circle surrounding the center of the beam is plotted as a function of the radius of the circle. Curve A is an experimental cw result, curve B is an experimental pulsed result, curve C is the result of theoretical calculation, and curve D is the desired encircled energy profile.

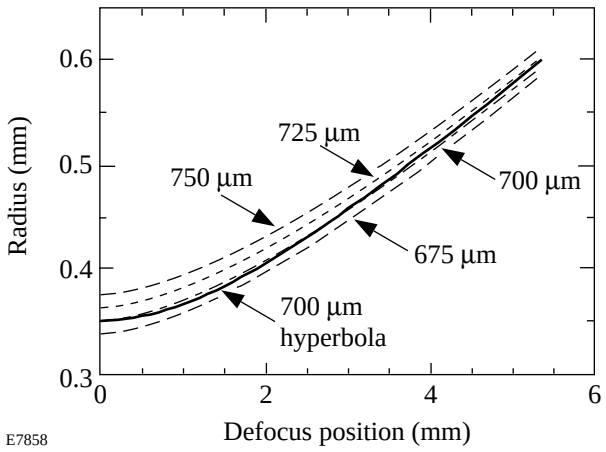

Figure 65.13
The radius of the contour containing 96.6% of the energy presented to the focal plane is plotted as a function of the shift of the focus lens along the optical axis. A range of target diameters between 800 and 1000 μm can be irradiated with the new continuous DPP. The gradient of the curve in the vicinity of an 800-μm target is approximately a change in diameter of 10 μm per 100 μm of focal shift.

Conclusions

An extensive development program has produced significantly improved DPP's that are characterized as continuous, deep-surface-relief phase plates. These DPP's can perform nearly lossless phase conversion of high-power UV laser beams, thus delivering up to 25% more energy than previous designs. These DPP's also provide the desired irradiance envelope and speckle distribution over the full 800- to 1000-μm range of target diameters envisioned for the near-term experimental target physics program at LLE. In addition, epoxy-replicated DPP's exhibit high damage thresholds and meet the design requirements for the upgraded OMEGA laser system. It is anticipated that near-term target experiments will be carried out on OMEGA to study the hydrodynamic benefits of these new DPP's with temporal beam smoothing and that additional criteria will be established to design fully optimized DPP's for the future.[5,6]

ACKNOWLEDGMENT

This work was supported by the U.S. Department of Energy Office of Inertial Confinement Fusion under Cooperative Agreement No. DE-FC03-92SF19460, the University of Rochester, and the New York State Energy Research and Development Authority. The support of DOE does not constitute an endorsement by DOE of the views expressed in this article.

REFERENCES

1. Laboratory for Laser Energetics LLE Review **33**, NTIS document No. DOE/DP/40200-65, 1988 (unpublished), p. 1

2. T. J. Kessler, Y. Lin, J. JArmstrong, and B. Velazquez, in *Laser Coherence Control: Technology and Applications*, edited by H. T. Powell and T. J. Kessler (SPIE, Bellingham, WA, 1993), Vol. 1870, pp. 95–104.

3. Laboratory for Laser Energetics LLE Review **55**, NTIS document No. DOE/DP/40200-257, 1993 (unpublished), p. 146.

4. Opticon Replication Center, 799 Middlesex Turnpike, Billerica, MA 01821.

5. Y. Lin, T. J. Kessler, and G. N. Lawrence, Opt. Lett. **20**, 764 (1995).

6. Laboratory for Laser Energetics LLE Review **64**, NTIS document No. DOE/SF/19460-99, 1995 (unpublished), p. 170.

Diagnosis of Shell-Core Mixing Using Absorption and Emission Spectra of a Doped Layer

A major limitation on fusion target performance is the mixing of shell material with the fuel during the final stage of the implosion. This mixing is the result of hydrodynamic instabilities that cause nonuniformities on the inner surface of the shell to grow as the shell decelerates. The seeds for this growth are nonuniformities that grow sufficiently during the acceleration phase to feed through the shell. This acceleration-driven growth is initially seeded by laser and target nonuniformities. The open geometry of planar targets has been used extensively to investigate growth during acceleration; however, to study deceleration-driven growth and shell-core mixing, implosions are required.[1] Recent experiments used the image of x-ray emission from the shell (enhanced by high-Z doping) to diagnose these effects experimentally.[2] We have subsequently shown theoretically[3] that when backlighter imaging is used in the experiment, additional information is obtained and the ability to detect shell-core mixing is enhanced. We have also shown[3–5] that in such a backlighting experiment, monochromatic imaging (using, for example, a diffracting crystal) is required because of the overwhelming self-emission from the target.

We present here the analysis of a different diagnostic method for detecting shell-core mixing that does not require backlighting; in effect, the central core emission is used as a backlighter for the surrounding shell. A particular target experiment is simulated and the expected experimental signature calculated and analyzed. This signature is the emerging x-ray spectrum rather than the target image, as was the case in the work cited above. The absorption spectrum produced when the core radiation traverses an embedded signature layer in the shell was reported earlier.[6] In that work (conducted in collaboration with LANL), we showed that when a KCl layer is embedded in a CH shell that is imploded as an exploding pusher, the continuum core radiation produces absorption lines of K and Cl ions that provide information on the temperature and $\rho\Delta r$ of the imploded shell. Here we show that, in doped targets that suffer shell-core mixing, emission lines of the dopant ions can appear due to inward migration of doped material. We show that for OMEGA experiments a small admixture of titanium dopant in a thin CH layer is sufficient for the measurement of titanium lines, yet creates minimal perturbation of the target behavior. We calculate the emerging spectra of a particular target implosion on the OMEGA laser. For this test case, *LILAC* results were used for the expected temperature and density profiles of the unmixed target. A post-processor code was developed[4] to calculate the emission and transport through the target. A simple procedure is used to simulate the mixing, and the radiation transport equation is then solved for unmixed as well as mixed targets.

The target is a polymer shell of 940-μm diameter and 30-μm thickness, filled with 80 atm DT gas. Within the CH polymer shell is a layer doped with titanium; the doped-layer thickness and position within the shell are varied. The concentration of titanium atoms, 1% by atom number, is such that a doped layer of a few-micron initial thickness would show significant absorption at the wavelengths of titanium lines. One-dimensional simulations by *LILAC* showed that the addition of such a layer made little change in hydrodynamic behavior. (This point is discussed further in the next section.) The choice of titanium was dictated by the fact that, at peak compression of the test target, radiation wavelengths shorter than ~3 Å are needed to avoid severe continuum absorption by the shell (as opposed to the much stronger line absorption). On the other hand, too high a Z (and thus too short wavelengths) would cause even the line absorption, essential to the method, to be insignificant.

For all simulations, the laser pulse is trapezoidal, rising linearly over 0.1 ns to 13.5 TW, then remaining constant for 2.2 ns, before dropping linearly over 0.1 ns. Figure 65.14 shows the density and electron-temperature profiles predicted for this target at peak compression. The shell material has been compressed to a mean radius of ~50 μm and a thickness of ~30 μm, with a density in the range of ~10 to 50 g/cm^3, corresponding to a $\rho\Delta r$ value of ~90 mg/cm^2. The electron temperature in the shell ranges from ~80 to ~800 eV. Most of the line absorption will occur within the colder, outer part of this compressed shell.

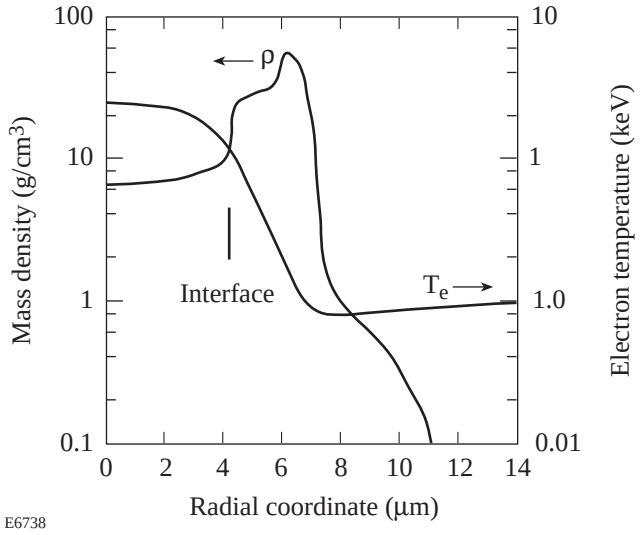

Figure 65.14
The density and electron-temperature profiles predicted by the *LILAC* code at peak compression for the case studied in this article. The vertical bar marks the position of the shell-fuel interface.

Modeling of Target Mixing and Radiation Transport

The procedure for modeling shell-core mixing was described in an earlier publication.[3] This procedure is applied to *LILAC*-calculated profiles of a particular implosion experiment; it does not include self-consistent feedback, i.e., the effect of mixing in one time step upon the hydrodynamics and radiation physics in subsequent steps. The limitations resulting from this simplification will be discussed. Briefly, mixing occurs during the deceleration (or burn) phase of the implosion. The model determines a radial region within which mixing is assumed to occur, the width of which is characterized by a parameter α. It is defined such that the deepest penetration of shell material into the fuel region spans a fraction α of the distance between the shell-core interface radius and the free-fall line (defined as the constant-velocity trajectory at the shell maximum velocity). As time progresses, this penetration increases; however, for the α values considered here, the penetration is not severe enough to reach the target center. Simulations of Rayleigh-Taylor unstable implosions[7] show that, in the nonlinear regime of the instability, the shell penetrates into the fuel in the form of spikes; between the spikes, the fuel penetrates into the shell region in the form of bubbles whose penetration is typically half that of the spikes (for an Atwood number close to 1). Within the mixed region, the fuel and shell material densities are assumed to decay linearly into each other's region. As explained in Ref. 3, this choice is more realistic than a uniformly mixed region. In particular, the resulting fraction of, say, fuel material as part of the total density is reasonably smooth and reaches the correct values at the boundaries of the mixed region. Furthermore, the effect of the mixing on the temperature and electron density distributions in the mixed region was also included. Finally, the model allows for the mixing of specific doped layers; namely, the dopant material follows the CH element in which it was embedded initially, and the percentage of doping remains the same.

To discern whether the discontinuity introduced by the doping increases any existing instability and thus mixing, the influence of doping on the growth rate of Rayleigh-Taylor instability was investigated. We note that the linear growth rate is proportional to $A^{1/2}$, where A is the Atwood number, defined as $(\rho_h - \rho_l)/(\rho_h + \rho_l)$ in terms of the high and low mass densities on each side of the discontinuity. In our case the density discontinuity caused by the doping is 2%, which by itself would give rise to an Atwood number of $A \sim \Delta\rho/2\rho \sim 0.01$. In typical target implosions, the Atwood number (determined by the density gradients near the ablation surface) is in the range of 0.5 to 1.0;[7,8] it can therefore be estimated that the growth-rate increase due to doping is less than 10%.

To simulate the emergent absorption and emission spectra, multigroup opacity tables were generated using the OPLIB opacity library.[9] The radiation transport model developed earlier[4] was used to calculate the emergent spectra. That model uses temperature and density profiles generated by *LILAC* and the multigroup opacity tables to calculate radiation emission and absorption. The use of the OPLIB opacity calculations requires the assumption of LTE conditions, the applicability of which is discussed in the following section.

Figures 65.15 and 65.16 show examples of OPLIB data for two density and two temperature values, relevant to the conditions of Fig. 65.14. The spectra consist of helium-like and hydrogen-like lines, including satellite lines that appear on the low-energy side of those lines. The major difference between the spectra at $T = 0.4$ keV and $T = 1$ keV is the appearance of the hydrogen-like (Lyman) lines; this is because, at the lower temperature, the population of the hydrogen-like specie is negligibly small. In going from a density of 0.4 to 12.8 g/cm^3, the plasma becomes less ionized, as indicated by a lower relative intensity of the Lyman lines when comparing the two $T = 1$ keV curves (the Lyman lines are absent from the lower temperature curves). Also, a comparison of the satellite manifold near the He-α line (especially for the two $T = 0.4$ keV

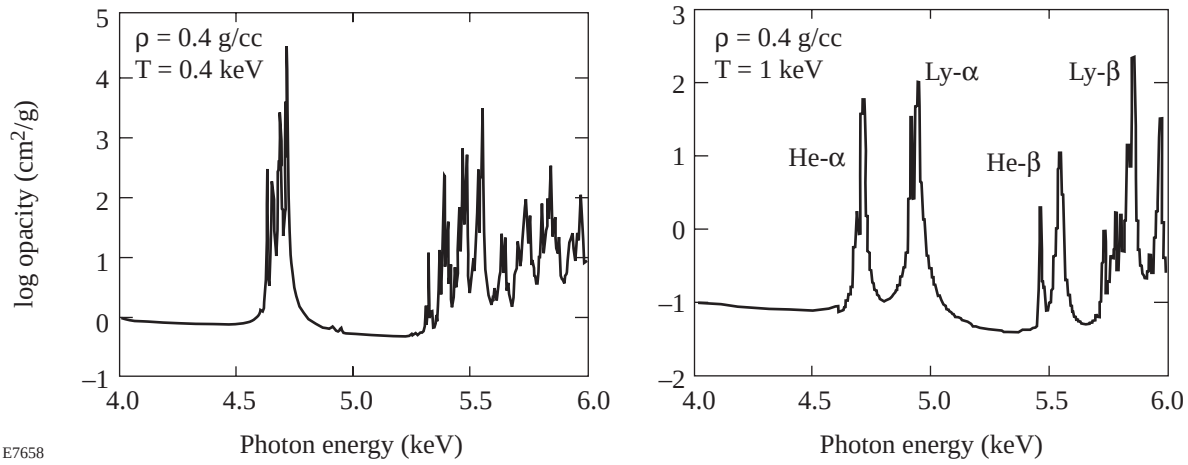

Figure 65.15
Examples of OPLIB opacity data for CH polymer containing 1% titanium (by number of atoms) for a density of 0.4 g/cm^3, at two temperatures.

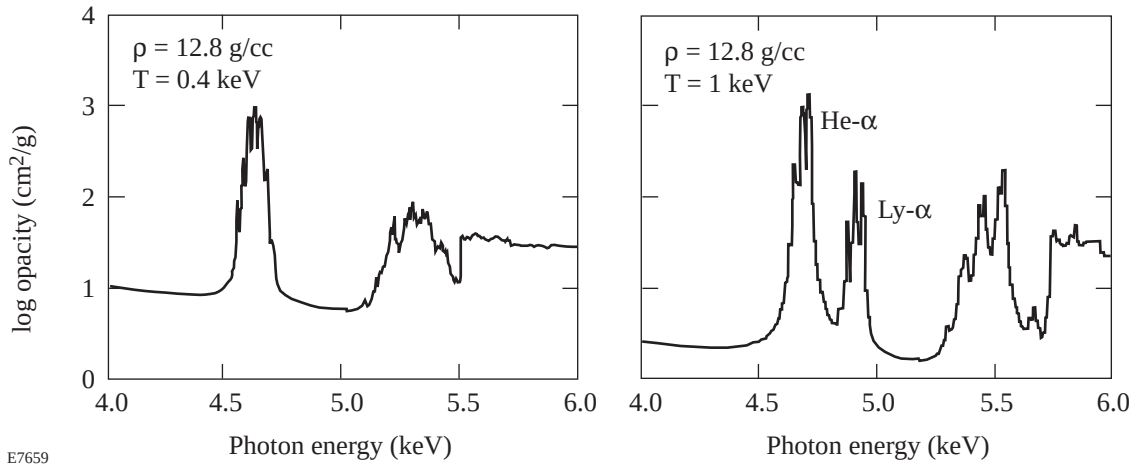

Figure 65.16
Examples of OPLIB opacity data for CH polymer containing 1% titanium (by number of atoms) for a density of 12.8 g/cm^3, at two temperatures.

curves) shows an intensity distribution of the peaks that is skewed more toward high energies for the lower-density case, again indicating decreased ionization with increasing density. This is the result of the increasing importance of three-body recombination, which rises faster with density than other, two-body processes. In the case for $T = 0.4$ keV and $\rho = 12.8$ g/cc, the combined effect of the low temperature and high density reduces the ionization to the point where even the He-α line is hardly visible. In that case, the spectrum consists mostly of satellite lines. Finally, we note that the absolute magnitude of the opacity tends to increase with increasing density and to decrease with increasing temperature, but these trends are modified by the changes in line ratios discussed above.

Satellite lines appear on the low-energy side of the various lines, such as the He-α line (at 4.7495 keV), the Lyman-α line (at 4.9733 keV), the He-β line (at 5.5821 keV), and the Lyman-β line (at 5.8915 keV). The satellite lines correspond to transitions similar to that of the nearby resonance line, in ion species that are progressively less ionized. For example, the He-α line corresponds to the transition $1s2p\ ^1P$–$1s^2\ ^1S$, whereas those of the nearby satellites correspond to transitions

of the type $1s(2l)^m$–$1s^2(2l)^{m-1}$, where m changes from 2 (Li-like specie) to 8 (F-like specie). Since the satellite lines correspond to L-shell ions, they are excited in colder target regions as compared with those of the K-shell ions. This is the basis for the mixing diagnostics described next.

Target Design for Mixing Diagnostics

The diagnostic method for mixing relies on the sharp temperature gradient at the shell-fuel interface within the imploded shell (see Fig. 65.14). Near that interface, the temperature is high enough (~0.5 to 1.0 keV) for the emission of helium-like and hydrogen-like titanium K-shell lines. In this method, the titanium layer is placed in the original target far enough from the interface, such that in a stable target, it never gets hot enough to significantly emit these lines. Then, mixing causes migration of doped polymer into the high-temperature regions closer to the fuel interface, thus causing emission of these lines.

Having chosen the doping material and concentration, we next determine the optimal location of the doped layer within the fabricated target. Figure 65.17 shows the spectra calculated using the OPLIB opacity tables and the radiation transport model described above, using the target profiles of Fig. 65.14 (peak compression in an unmixed target). A signature layer at different locations within the shell consists of 1% titanium doping (by atom number) in the CH polymer. The boundaries of the signature layer in the initial target, with respect to the shell-core interface, are (a) 0 to 1.12 μm, (b) 0.9 to 1.12 μm, (c) 0.92 to 1.12 μm, and (d) 0.94 to 1.12 μm. The continuous spectrum emitted by an undoped target is also shown. The curves represent the x-ray fluence per unit area along a line of sight through the center of the target (with unit magnification), normalized to a spectral intensity of 7.0×10^{20} keV/(keV ns cm^2 Ω).

Each spectrum shown in Fig. 65.17 contains two distinct features: (a) the absorption-line manifold in the range ~4.5 to 4.7 keV, and (b) the higher-energy emission lines. Feature (a) consists of satellite lines near the He-α line. These lines are absorbed within the colder, outer part of the compressed shell, as is evidenced by the fact that they are almost identical when comparing the four spectra of Fig. 65.17. The ionization energy of the Li-like to F-like species ranges from ~1.4 keV down to ~0.8 keV. These species will predominate in regions of temperatures lower than ~0.5 keV. Figure 65.14 shows that the temperature of the outer half of the compressed shell is indeed within this range; it is there that these satellite lines are absorbed. It should be noted that these satellite lines usually appear in absorption but not in emission. The temperature where species with $n = 2$ bound electrons can exist is insufficient for exciting $n = 1$ electrons. Thus, the satellite lines can be excited only by continuum radiation streaming from higher-temperature regions, leading to absorption lines at energies that are at resonance with satellite transitions. However, these lines can appear in emission in flat-target experiments[10] since

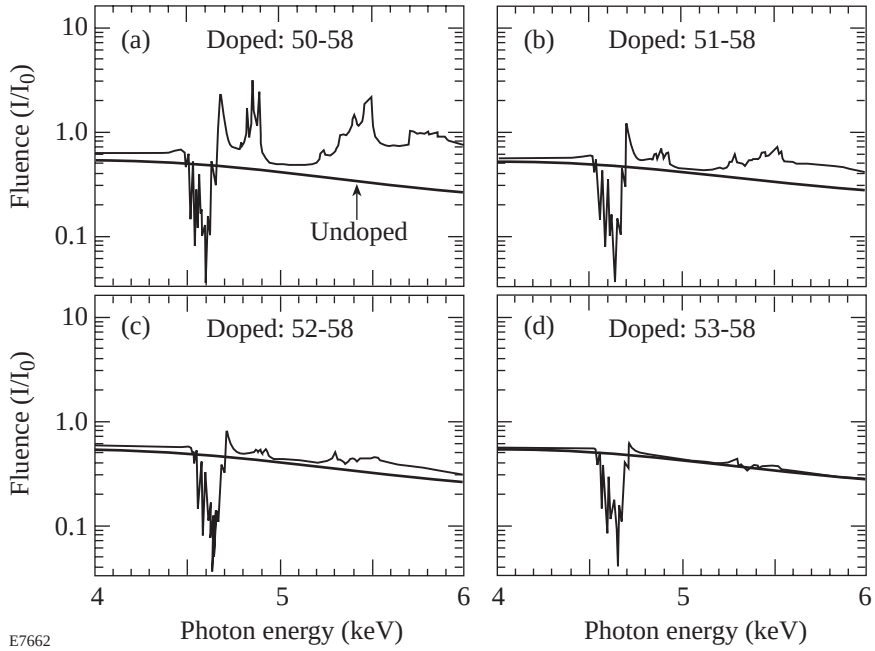

Figure 65.17
Predicted spectrum, at the time of peak compression, emitted by the imploded target of Fig. 65.14, with no mixing. A signature layer is added at different locations within the shell (Lagrangian code zone numbers are shown). The boundaries of the signature layer in the initial target, with respect to the shell-core interface are (a) 0 to 1.12 μm, (b) 0.9 to 1.12 μm, (c) 0.92 to 1.12 μm, and (d) 0.94 to 1.12 μm. The continuous spectrum due to an undoped target is also shown. The curves represent the target fluence per unit area along a line of sight through the center of the target (at the plane of the target), normalized to a spectral intensity of 7.0×10^{20} keV/(keV ns cm^2 Ω).

the exciting continuum is then moving into the target, and the detector sees only the fluorescent lines emitted as a consequence of the radiative excitation.

The spectral lines above ~4.7 keV (from helium-like and hydrogen-like ions) are seen in Fig. 65.17 to be emitted only close to the interface, where the temperature is sufficiently high to excite these lines. One may wonder why these lines are not seen to be absorbed far from the interface. The helium-like and hydrogen-like lines could be absorbed in regions where the temperature is sufficiently high to ionize all $n = 2$ electrons but not high enough to excite these lines; evidently the region of this intermediate temperature is too narrow for significant absorption.

The various features in Fig. 65.17 offer the possibility of diagnosing mixing: if the doped layer is placed as in the target of Fig. 65.17(d), the spectrum in the absence of mixing will show only the absorption lines in the range of ~4.5 to 4.7 keV. However, mixing could cause some of the titanium material to migrate to hotter regions, which will cause the appearance of emission lines in the range above 4.7 keV [as in Fig. 65.17(a)].

The titanium concentration should be high enough to yield substantial line absorption but low enough to minimize its effect on the target behavior. Figure 65.17 shows significant line absorption (attenuation by up to a factor of ~10) on the lines in the range of 4.5 to 4.7 keV. The minimal effect on the target behavior is evidenced by the negligible increase in continuum emission with respect to the no-doping case. The considerations for optimizing the doped-layer location within the fabricated target are as follows: The inner radius of the doped region should be far enough removed from the interface to show no emission of lines in the absence of mixing, yet not too far so as to require very severe mixing to yield a difference in the spectrum. Figure 65.17(d) shows an optimal choice for this distance. Finally, the outer radius of the doped layer should extend far enough from the interface to give rise to significant line absorption, otherwise the dopant concentration must be increased. The extent of the layer must be limited to minimize the effects on the stability of the ablating part of the target.

The applicability of the LTE assumption in using the OPLIB opacity library will be discussed in this section, in view of the spectra shown in Fig. 65.17. Generally speaking, the LTE approximation becomes valid for high-density, low-temperature, and low-nuclear-charge conditions. Note that the two groups of lines in the titanium spectrum originate from different ion species (see Fig. 65.17): absorption lines come from lower ionizations (Li-like to O-like species) and emission lines come from higher ionizations (He-like and H-like). We examined the equilibrium conditions for these two line groups separately (following Ref. 11) for the compressed-shell conditions in Fig. 65.14. The condition for complete LTE [Eq. (6-60) in Ref. 11] for a temperature of 300 eV and average excitation energy of 1 keV is that ρ be greater than ~7 g/cm^3. For the L-shell species giving rise to the absorption lines (Fig. 65.17), the condition is well satisfied for the compressed shell. It should be emphasized that the assumption of LTE is not critical when calculating the spectrum of absorption lines. Absorption lines depend on the ground-state populations that are almost equal to the total density of the pertinent ion specie, whereas, emission lines depend on the excited-state populations that can vary greatly between LTE and non-LTE model predictions. Furthermore, the absorption manifold observed in the spectrum corresponds to a range of ion species of successive ionizations. Therefore, small deviations from LTE would merely redistribute some of the absorption among neighboring ionic features, but the total amount of absorption will hardly change. Turning to the emission lines, we find by comparison with results obtained with the non-LTE code *POPION*[12] that the LTE model slightly overestimates the intensity of He-like lines and greatly overestimates that of the H-like lines. Thus, in comparing experimental spectra to theoretical results, emphasis should be placed on the helium-like lines.

Effect of Mixing on the Spectrum

We apply now the mixing model described earlier to the target experiment under consideration (Fig. 65.14) and calculate the emergent spectrum for various degrees of mixing. As mentioned, the portion of the CH layer from 0.94 μm to 1.12 μm away from the interface was doped with titanium at a concentration of 1% by atom number.

Figures 65.18 and 65.19 show the results of such calculations for two mixing severities: $\alpha = 0.2$ and $\alpha = 0.4$, respectively. The curve marked "undoped" corresponds to an undoped and unmixed target simulation that is shown as a reference. The mixing in the case $\alpha = 0.2$ (Fig. 65.18) is seen to be too weak to be diagnosed using the emitted spectrum. The main effect of mixing on the spectrum in Fig. 65.18 is a slight lowering of the intensity in the emergent continuum. This occurs because mixing causes the transfer of some titanium material to smaller radii, thus increasing its areal density ($\rho\Delta r$) and increasing the absorption of the core continuum by the titanium in the shell.

When the mixing level is increased to $\alpha = 0.4$, the effect, as seen in Fig. 65.19, is dramatic. For clarity, the curves for the

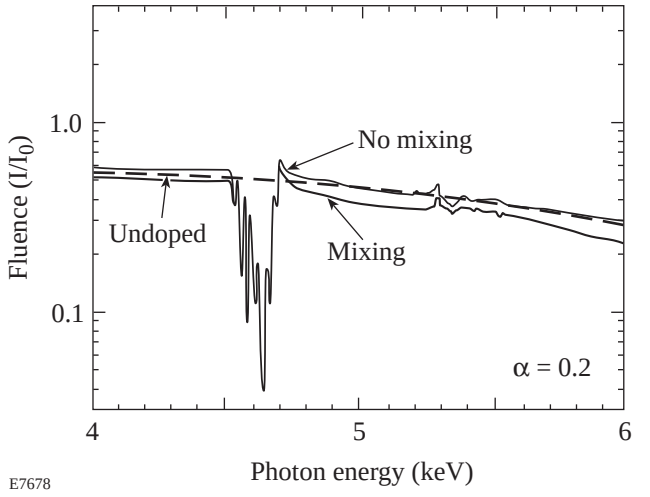

Figure 65.18
Effect of mixing on the spectrum shown in Fig. 65.17(d), for a mixing parameter $\alpha = 0.2$. The profiles of the absorption line manifold for the two cases essentially overlap. The curve marked "undoped" corresponds to an undoped as well as unmixed target run.

case of mixing and for the case of no mixing are shown separately, and on different scales, in Figs. 65.19(a) and 65.19(b). Mixing causes the level of the emitted continuum to rise because some of the titanium migrates into the high-temperature layer close to the interface. However, the main mixing signature is the appearance of emission lines above ~4.7 keV. More quantitatively, mixing can be indicated by the measured ratio of emission to absorption lines, for which only relative line intensities need to be measured. As seen in Fig. 65.19, the absorption-line manifold does not change appreciably due to mixing. Since the absorption of these titanium lines (relative to the continuum level) depends[6,13] mainly on the $\rho\Delta r$ of cold doped layer, this indicates that the $\rho\Delta r$ is not reduced appreciably due to the transfer of some cold doped material into the hot interface region. The appearance of this absorption manifold in the measured spectrum can thus serve to determine how much of the cold shell remained intact in spite of mixing.

The emission lines above 4.7 keV include helium-like and hydrogen-like lines, as well as satellites near the Lyman-α line and the He-β line. These latter satellites do not appear in absorption, as do the satellites near the He-α line, for the following reasons: The satellites near the Lyman-α line are due to transitions of the type $2p2l$–$1s2l$, so that the absorbing level $1s2l$ is an excited state; thus, the density of ions that can absorb these transitions is relatively small. On the other hand, satellites near the helium-like lines are absorbed by ions in ground configurations, $1s^2 2l$, whose relative density is high.

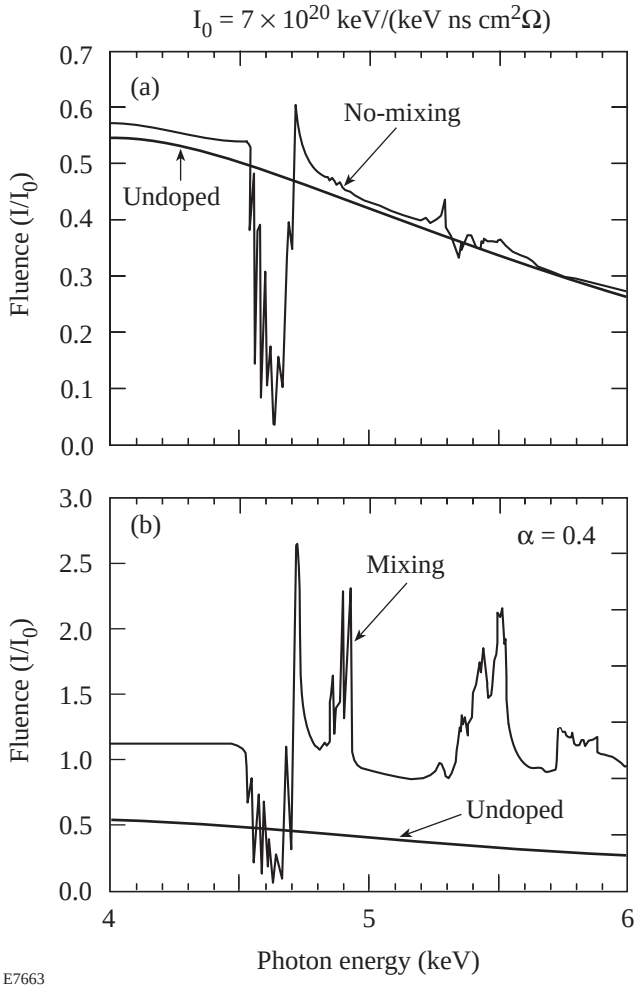

Figure 65.19
Effect of mixing (b) on the spectrum (a) from Fig. 65.17(d), for a mixing parameter $\alpha = 0.4$. The curve marked "undoped" corresponds to an undoped as well as unmixed target run.

The $\rho\Delta r$ of the absorption region is apparently high enough to absorb the satellite lines near the He-α line but not to absorb the weaker satellite lines near the He-β line (the latter, however, have previously been observed in absorption in argon[13]). In comparing the line absorption in Fig. 65.19(a) to that in Fig. 65.19(b), one would have expected less absorption in the latter case because the transfer of some titanium to the high-temperature layer necessarily reduces the amount of cool, absorbing titanium. However, the relative absorption in the two cases is comparable because some titanium moves inward but still remains within the absorbing layer, yielding a higher areal density of absorbing material.

We compare this method with a similar mixing experiment involving chlorine-doped, argon-filled targets.[14] Both meth-

ods are based on the observation of spectral lines of a shell dopant that moves into higher-temperature regions due to mixing. In the Cl/Ar method, the use of relative line intensities from the two elements obviates the need for absolute intensity measurement; here, a similar role is played by the comparison of emission and absorption lines. Generally, the choice of dopant has to be adjusted to the expected conditions: a higher-Z dopant is required to probe higher temperatures and to escape from higher-compression targets.

We finally consider an experiment based on the results presented here. Since the determination of mixing relies on comparison with code simulations, we have to allow for uncertainties in the modeling. In particular, results such as in Figs. 65.18 and 65.19 do not account for self-consistent hydrodynamic calculations. Thus, the core temperature can be expected to rise less if the compression is unstable. This effect would reduce the intensity of emitted titanium lines and counter the intensity rise due to mixing. To address this concern, the experiment should include a normalizing target, where the doping extends up to the interface [as in Fig. 65.17(a)]. We show in Fig. 65.20 the effect of mixing at a level of $\alpha = 0.4$ on such a doped target. As seen, the effect is minor since the interface contains doped material even without mixing. The line emission from this target is therefore dependent mostly on the core temperature rather than on mixing and can serve as a normalizing experiment. For example, if an experiment using the target of Fig. 65.17(a) shows strong line emission, but one using the target of Fig. 65.17(d) does not, we can surmise that the mixing is smaller than $\alpha = 0.4$ since the interface is hot enough for the emission of titanium lines. This assumes that the cooling effect of the instability on the two targets is comparable. This is to be expected since, as shown for the present level of doping, the effect on target energetics is small. More quantitatively, we can calculate the intensity ratio between emitted titanium lines in Fig. 65.19(b) and in Fig. 65.20(b) as a function of α. This ratio depends strongly on α since only the former case depends strongly on mixing; the latter is seen to be almost independent of mixing [by comparing Figs. 65.20(a) and 65.20(b)]. Self-consistent modeling would cool the core about equally in the two cases since the target energetics depend mostly on the mixing, not the doping.

The calculation results shown in Figs. 65.18 and 65.19 correspond to an axial view of the target at peak compression. To realize these conditions in the experiment, a spatially resolving slit should be placed in front of the spectrometer. Since the diameter of the core at peak compression in Fig. 65.14 is ~50 μm, the slit width need not be much narrower than that. To limit the measurement to the peak of the compression, the spectrum should be detected with a streak or framing camera; however, since most of the radiation from imploding targets such as in Fig. 65.14 is emitted around peak compression, a time-integrating instrument should also provide useful results.

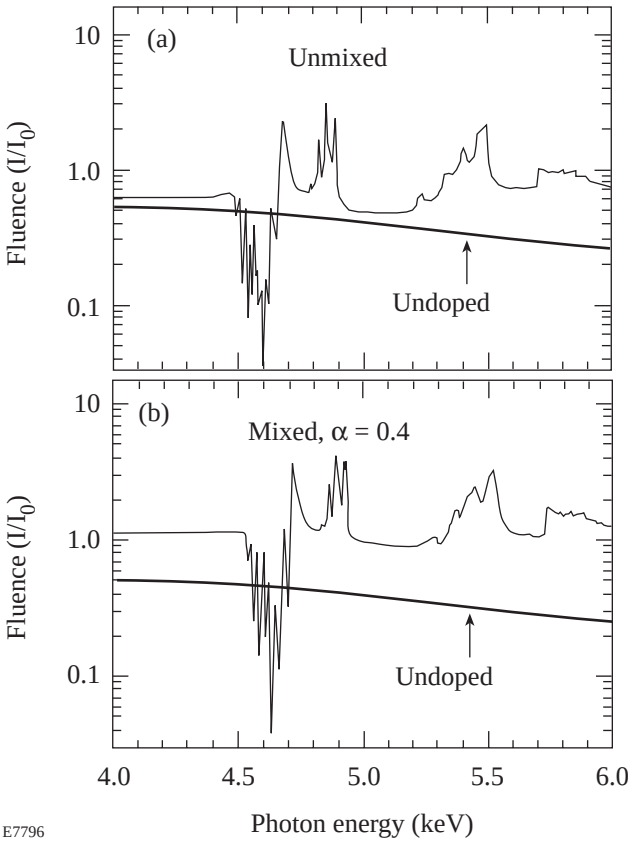

Figure 65.20
Effect of mixing on the spectrum shown in Fig. 65.17(a), for a mixing parameter $\alpha = 0.4$. The curve marked "undoped" corresponds to an undoped as well as unmixed target run.

ACKNOWLEDGMENT

This work was supported by the U. S. Department of Energy Office of Inertial Confinement Fusion under Cooperative Agreement No. DE-FC03-92SF19460, the University of Rochester, and the New York State Energy Research and Development Authority. The support of DOE does not constitute an endorsement by DOE of the views expressed in this article.

REFERENCES

1. J. D. Lindl, R. L. McCrory, and E. M. Campbell, Phys. Today **45**, 32 (1992).

2. O. L. Landen, W. K. Levendahl, and T. R. Dittrich, Bull. Am. Phys. Soc. **38**, 2083 (1993).

3. Laboratory for Laser Energetics LLE Review **59**, NTIS document No. DOE/SF/19460-36, 1994 (unpublished), p. 114 .

4. Laboratory for Laser Energetics LLE Review **58**, NTIS document No. DOE/SF/19460-17, 1994 (unpublished), p. 57.

5. B. Yaakobi, F. J. Marshall, Q. Su, and R. Epstein, J. X-Ray Sci. Technol. **5**, 73 (1995).

6. A. Hauer, R. D. Cowan, B. Yaakobi, O. Barnouin, and R. Epstein, Phys. Rev. A **34**, 411 (1986).

7. C. P. Verdon, R. L. McCrory, R. L. Morse, G. R. Baker, D. I. Meiron, and S. A. Orszak, Phys. Fluids **25**, 1653 (1982).

8. D. L. Youngs, Physica **12D**, 32 (1984); S. W. Haan, Phys. Rev. A **39**, 5812 (1989); N. Freed, D. Ofer, D. Shvarts, and S. A. Orszag, Phys. Fluids A **3**, 912 (1991).

9. M. F. Argo and W. F. Huebner, J. Quant. Spectrosc. Radiat. Transfer **16**, 1091 (1976).

10. B. Yaakobi, J. Delettrez, L. M. Goldman, R. L. McCrory, W. Seka, and J. M. Soures, Opt. Commun. **41**, 355 (1982).

11. H. R. Griem, in *Plasma Spectroscopy* (McGraw-Hill, New York, 1964), Chap. 6.

12. R. Epstein, S. Skupsky, and J. Delettrez, J. Quant. Spectrosc. Radiat. Transfer **35**, 131 (1986).

13. B. Yaakobi, R. Epstein, F. J. Marshall, D. K. Bradley, P. A. Jaanimagi, and Q. Su, Opt. Commun. **111**, 556 (1994).

14. T. R. Dittrich *et al*., Phys. Rev. Lett. **73**, 2324 (1994).

Self-Consistent Stability Analysis of Ablation Fronts with Large Froude Numbers

In inertial-confinement fusion (ICF), the ablation front of the imploding capsules is hydrodynamically unstable.[1,2] The heavy material of the compressed pellet is accelerated by the low-density ablating plasma, thus making the pellet interface unstable to density perturbations (Rayleigh-Taylor instability).[3] The classical treatment[3] of this instability occurring at the interface of a heavy fluid with uniform density ρ_h, supported by a light fluid with uniform density ρ_l, yields the growth rate $\gamma_{cl} = \sqrt{A_T kg}$, where g is the acceleration and $A_T = (\rho_h - \rho_l)/(\rho_h + \rho_l)$ is the Atwood number. It is noteworthy that, in the classical case, the growth rate monotonically increases with the mode wave number k, and the Atwood number is constant. However, in ICF, the convection of ablated material through the interface leads to a reduction of the growth rate with respect to the classical value $(\gamma/\gamma_{cl} < 1)$ and, for sufficiently short wavelengths, the instability is suppressed.[4–20] Thus, only those modes with wave number smaller than a critical value[14–16] ($k < k_c$, where k_c is the cutoff wave number) are unstable. In addition, the density profile of ICF targets monotonically decreases in the ablation and blow-off regions, thus complicating the definition of a light-fluid density (ρ_l) to be used in the definition of the classical Atwood number. For a monotonic density profile and mode wavelength smaller than the density-gradient scale length,

$$kL >> 1, \quad \text{where} \quad L = \rho(d\rho/dy)^{-1},$$

the growth rate of the classical Rayleigh-Taylor instability (without ablative flow) is $\gamma_{cl} \simeq \sqrt{g/L_{\min}}$, where $L_{\min}$ is the minimum density-gradient scale length. This result has led several authors[1,20] to approximate the Atwood number with an asymptotic formula $(A_T = 1/1 + kL_{\min})$ that reproduces the classical results for long- and short-wavelength modes, and for $\rho_l << \rho_h$. In this article, the Atwood number is derived for equilibria with ablative flow, and it is shown that the classical formula does not apply to ablation fronts. The ablative Atwood number depends on the density-gradient scale length, the mode wavelength, and the law of thermal conduction.

A qualitative description of convective (or ablative) stabilization can be obtained by using the incompressible sharp boundary model[7–10] consisting of two fluids of constant density separated by an interface of zero thickness with mass flowing from the heavy to the light fluid. For subsonic ablation flows, the perturbed velocity field is assumed to be incompressible $(\nabla \cdot \tilde{\mathbf{v}} = 0)$ through the interface. It is easily shown that the assumption of divergence-free velocity perturbations is not consistent with an accelerating equilibrium flow, i.e., the equation describing the perturbation cannot be used to determine the equilibrium profiles. Since the equilibrium is one-dimensional, the incompressibility condition leads to a uniform velocity profile ($U = constant$), in clear contradiction with the mass conservation that requires a uniform mass flow ($\rho U = constant$) and a jump in the profiles. In addition, the model requires a closure equation, as the number of unknowns exceeds the number of equations. Several closure equations have been proposed by different authors[7–10] leading to discrepancies in the final results. In Ref. 10, the sharp boundary model is improved by a self-consistent calculation of the density jump occuring at the ablation front. Nevertheless, an additional closure equation [Eq. (5) of Ref. 9] is still needed and the model is not self-consistent.

Monotonic equilibrium profiles of ablation fronts can only be reproduced by retaining the effect of finite thermal conductivity in the energy equation. Thus, for consistency, the effect of thermal conduction should be retained in the stability analysis as well. Kull and Anisimov developed a model[4] (the isobaric model) that includes thermal conduction and neglects other less important physical effects such as finite Mach number. Their model is self-consistent because it can be solved to determine the equilibrium profiles as well as to carry out the stability analysis. However, in Ref. 4, Kull and Anisimov analytically solve the isobaric model without determining the self-consistent equilibrium. They assume instead that a sharp boundary exists between the heavy and the light fluids. Although their model is self-consistent, their solution is not. Later, Kull[5] numerically solves the self-consistent isobaric

model and finds a large discrepancy with the sharp boundary results. The numerical results of Kull[5] also agree with the results of Ref. 6. The latter can be fitted by the well-known formula

$$\gamma = \alpha_T \sqrt{kg} - \beta_T k V_a , \tag{1}$$

where V_a is the ablation velocity and α_T, β_T are given later in the section on **Stability Analysis**. This formula has been derived by numerically solving the exact eigenvalue problem, including electronic heat transport ($\kappa \sim T^{\nu}$, $\nu = 2.5$), for large Froude numbers (Fr = 5–9, see Table I of Ref. 5), where $Fr = V_a^2 / gL_0$ and L_0 is the characteristic width of the ablation front and will be specified in the next section. The numerical results of Kull[5] and Takabe[6] have also been confirmed by several two-dimensional simulations of accelerated targets and capsule implosions.[18,19]

The great difficulties in the analytic solution of the self-consistent problem had prevented the derivation of an analytic growth-rate formula that reproduces the numerical results. Only recently, some attempts have been made to close this gap by solving the self-consistent problem using asymptotic techniques.

The first attempt is found in Ref. 12, where the Wentzel-Kramers-Brillouin (WKB) approximation is used to determine the cutoff wave number in the case of electronic heat conduction ($\nu = 2.5$). Based on this analytic estimate, V. V. Bychkov, S. M. Goldberg, and M. A. Liberman derive an approximate growth-rate formula, similar to Eq. (1), with $\beta = 2.5$–3.2 and $\alpha^2 = (\rho_1 - \rho_2)/(\rho_1 + \rho_2)$, where ρ_1 is the peak density and ρ_2 is the critical density. In Ref. 16, the cutoff formula for long-wavelength modes and $Fr > 1$ is derived self-consistently for an arbitrary power law dependence of the thermal conduction $(\kappa \sim T^{\nu},\ \nu > 1)$ using boundary layer theory. The eigenvalue equation is solved in the overdense, ablation, and blowoff regions, and the solutions are asymptotically matched. For $\nu = 2.5$, this formula agrees with the analytic estimate of Ref. 12 and reproduces the numerical results of Ref. 5 for different values of ν.

A semi-analytical, self-consistent analysis is also carried out in Ref. 13 by matching the analytical solution of the ablation region with the numerical solution of the blowoff region. The growth rate of Ref. 13 and the fully analytic formula derived in this article are in agreement for $\nu = 2.5$ and $Fr > 10$, but significant discrepancies exist for large ν's. A more detailed comparison between analytical, semi-analytical, and numerical results is presented in the **Discussion** section.

In this article, the importance of a growth rate formula valid over a large range of ν's is emphasized. In fact, numerical simulations show that direct- and indirect-drive ICF capsule implosions have different instability growth rates. This could be related to the different mechanism of energy transport—indirect-drive ICF is dominated by radiation transport and direct drive by electronic thermal conduction. In the diffusive radiation model,[21] the heat flux transported by radiation heat conduction is proportional to the temperature gradient $(q = -\kappa \nabla T)$ and the effective radiation thermal conductivity $\kappa = 16\sigma T^3 l(T)/3$, where σ is the Stefan-Boltzmann constant, and $l(T)$ is the Rosseland mean free path. According to Ref. 21, $l(T)$ can be approximated by a power law with the power index dependent on the material properties. For example, in an optically thick, fully ionized homogeneous plasma, $l(T) \sim T^{3.5}$ and $\kappa \sim T^{6.5}$. The variance of the power index has provided the motivation to carry out the stability analysis for arbitrary values of ν ($\kappa \sim T^{\nu}$) and to determine a generalized formula for the growth rate.

In this article, we present the analytical solution of the eigenvalue problem derived from the linearized isobaric model of Kull and Anisimov[4] for long-wavelength perturbations ($kL << 1$), closing the gap between theory and numerical computations, and extending the validity of the growth-rate formula to a large range of ν's. The analysis is limited to $\nu > 1$ and large values of the Froude number, thus restricting the unstable spectrum to wavelengths longer than the width of the ablation front. In fact, as shown in Ref. 16, the cutoff wave number for large-Froude-number equilibria occurs at long wavelengths: $k_c L_0 \sim 1/Fr^{\frac{\nu}{\nu-1}} << 1$. Configurations with $Fr > 1$ are typical for ablation fronts characterized by pure electron heat conduction (such as those considered in Ref. 6), some indirectly driven targets with large ablation velocities, and some directly driven targets with a strong radiation emission [such as those containing poly-vinyl-chloride (PVC or C_2H_3Cl)].

The growth rate is obtained by performing a boundary layer analysis in the regions of different scale lengths for the perturbation and subsequent asymptotic matching. The analytic theory is compared with the numerical results of Kull[5] and Takabe[6] for different values of Fr and ν.

This article is organized as follows: First, the isobaric model describing the evolution of accelerated ablation fronts is presented; next, the equilibrium profiles are derived, a stability analysis is performed, and the growth-rate formulas are reported. Finally, in the discussion section, the growth-rate formulas are compared with the numerical results.

Isobaric Model

We consider an ablatively accelerated fluid in steady state. In the ablation-front frame of reference, the evolution of the mass density ρ, velocity $\mathbf{v}$, and temperature T is described by the following conservation equations:

$$\frac{\partial \rho}{\partial t} + \nabla \cdot \rho \mathbf{v} = 0 \tag{2}$$

$$\rho\left(\frac{\partial \mathbf{v}}{\partial t} + \mathbf{v} \cdot \nabla \mathbf{v}\right) = -\nabla p + \rho \mathbf{g} \tag{3}$$

$$\rho \mathbf{c}_v \left(\frac{\partial T}{\partial t} + \mathbf{v} \cdot \nabla T\right) = -p \nabla \cdot \mathbf{v} + \nabla \cdot \kappa \nabla T \ , \tag{4}$$

where $\mathbf{g} = g\mathbf{e}_\mathbf{y}(g<0)$, $p = \rho T/A$ is the hydrodynamic pressure, $c_v = A^{-1}/(\gamma_h - 1)$ is the specific heat at constant volume, and γ_h is the ratio of the specific heats. The constant $A = \rho/(n_i + n_e) \simeq m_i/(1+Z)$ represents the average particle mass, where m_i is the ion mass, Z is the atomic number, and n_i, n_e are the ion and electron particle densities, respectively. The thermal conductivity κ has a power law dependence on the temperature, $\kappa = \kappa_a (T/T_a)^\nu$, where T_a is the ablation temperature.

For realistic ICF implosions, the energy equation can be simplified by assuming that the sound speed C_s at the ablation surface is much larger than the ablation velocity V_a, i.e., a negligible Mach number M $(M = V_a/C_s << 1)$, and the density-gradient scale length $\left[L = \rho(d\rho/dy)^{-1}\right]$ is much smaller than the stratification length C_s^2/g. Following the work of Kull and Anisimov,[4] the simplified energy equation can be rewritten in divergence-free form,

$$\nabla \cdot \left(\mathbf{v} + L_0 V_a \frac{\nabla \xi}{\xi^{\nu+2}}\right) = 0, \tag{5}$$

where $\xi = \rho/\rho_a$ is the density normalized to its peak value ρ_a, and L_0 is the typical width of the ablation front,

$$L_0 \equiv \frac{\gamma_h - 1}{\gamma_h} \frac{A\kappa_a}{\rho_a V_a} \ . \tag{6}$$

For classical electron thermal conduction, $\nu = 5/2$, and κ_a is given by Spitzer,[22]

$$\kappa_a = \frac{32 T_a^{5/2}}{\pi^{3/2}\sqrt{2}\Phi(Z)\Lambda Z e^4 \sqrt{m_e}} \ , \tag{7}$$

where Λ is the Coulomb logarithm and

$$\Phi(Z) \simeq (Z + 4.16)/(Z + 0.24).$$

As will be shown later, the constant L_0 is proportional to the density-gradient scale length at the ablation front.

Equations (2), (3), and (5) represent a complete set of four equations for the four variables ρ, v_x, v_y, and p that can be used to study the equilibrium and stability of accelerated ablation fronts.

Equilibrium Profiles

The equilibrium profiles can be derived from Eqs. (2), (3), and (5) by setting $\partial/\partial t = 0$. Although a detailed description of such profiles is given by Kull in Ref. 5, we summarize herein the main results. The density profile obeys the following first-order differential equation obtained by combining Eqs. (2) and (5):

$$\frac{d\xi}{dy} = \frac{1}{L_0} \xi^{\nu+1}(\xi_0 - \xi), \tag{8}$$

where ξ_0 is an integration constant. The appropriate boundary conditions for ablation fronts require the density profile to be flat at the peak value ($\xi' = 0$ for $\xi = 1$, leading to $\xi_0 = 1$) and evanescent in the downstream or expansion region ($\xi \to 0$ for $y \to -\infty$). The steepness of the profile depends on the value of L_0 that is determined by the thermal conduction and the ablation rate. Using Eq. (8), the density-gradient scale length can be written as $L = L_0/\left[\xi^\nu(1-\xi)\right]$ and its minimum value[5] is proportional to L_0, $L_{\min} = \left[(\nu+1)^{\nu+1}/\nu^\nu\right] L_0$. As described in Ref. 16, the length L_0 can also be related to the distance L_e between the peak of the density and the 1/*e* point.

Although Eq. (8) cannot be solved in closed form, an approximate solution can be found in proximity of the peak

density (overdense region), where $y > 0$, $\xi \approx 1$, and in the blowoff region, where $y < 0$, $\xi << 1$:

$$\xi_{\text{overdense}} \approx 1 - e^{-y/L_0}, \quad \xi_{\text{blowoff}} \approx \left(-\frac{L_0}{\nu y}\right)^{1/\nu}. \quad (9)$$

Equation (9) shows that the density profile is sharp near the peak density, where $L \simeq L_0$, and becomes smooth in the expansion region, where $L \simeq -\nu y$ and $-y >> L_0$. The equilibrium velocity profile can easily be derived from the mass conservation equation $\left[\nabla \cdot (\rho \mathbf{U}) = 0\right]$. Since the ablated material is flowing toward the light fluid, then $\mathbf{U} = U\mathbf{e}_y$, $U < 0$, and $\rho U = const$. In the overdense region, the velocity U approaches a constant value $U(y \to \infty) = -V_a$, and its magnitude monotonically increases in the blowoff region $\left[U(y \to -\infty) \to -\infty\right]$.

It is important to observe that the density-, velocity-, and temperature-gradient scale lengths are determined by the thermal-conductivity coefficient, the ablation rate, and the power index ν. The profiles become smoother as κ_a or ν increases.

Stability Analysis

The linear stability analysis proceeds in the standard manner. Following Ref. 16, all perturbed quantities are written as $Q_1 = \tilde{Q}(y) \exp(ikx + \gamma t)$, and the linear equations can be combined into a single fifth-order differential equation,

$$\left[\partial_{\hat{y}}\left(\Gamma_a \xi + \partial_{\hat{y}}\right)\partial_{\hat{y}} - \left(\Gamma_a \xi + \partial_{\hat{y}}\right)\right]$$

$$\times \in \hat{L}\left[\left(\Gamma_a \xi + \partial_{\hat{y}}\right)\tilde{\Phi}\xi^{\nu} + \in \hat{\nabla}^2\tilde{\Phi}\right]$$

$$+ \partial_{\hat{y}}\left(\Gamma_a \xi + \partial_{\hat{y}}\right)\left[\partial_{\hat{y}}\tilde{\Phi}\xi^{\nu} + \in \hat{\nabla}^2\tilde{\Phi}\right]$$

$$+ \in \hat{\nabla}^2\tilde{\Phi} + \frac{1}{\in Fr}\tilde{\Phi}\xi^{\nu+2} = 0, \quad (10)$$

where $\tilde{\Phi} = \tilde{\rho}/\left(\rho\xi^{\nu+1}\right)$, $\hat{y} = ky$, $\Gamma_a = -\gamma/kV_a$, $Fr = V_a^2/|g|L_0$ is the Froude number, $\hat{\nabla} = k^{-1}\nabla$, $\in = kL_0$, and $\hat{L} = L/L_0$. Equation (10) is an eigenvalue equation for the growth rate $\gamma = -\Gamma_a kV_a$. The eigenfunction must satisfy the boundary conditions corresponding to a vanishing perturbation at infinity, i.e., $\tilde{\mathbf{v}}(\pm\infty) = 0$, $\tilde{p}(\pm\infty) = 0$, and $\tilde{\rho}(\pm\infty) = 0$. Because of the complicated spatial dependence of the coefficients, Eq. (10) cannot be solved in closed form. However, an approximated solution can be found for large values of Fr and long-wavelength modes ($Fr >> 1, \in << 1$). The presence of the small parameter $\in$ makes Eq. (10) solvable by asymptotic methods such as boundary layer theory. First, the equation is solved in regions of different scale lengths for the perturbations. Then, the solutions are asymptotically matched at the boundaries of each region. The asymptotic matching and the boundary conditions lead to a unique value of the growth rate γ. Using the shape of the density profile and the scale length of the perturbations, three regions can be identified (see Fig. 65.21): (1) the overdense region, where $\hat{y} >> \in$, (2) the ablation front, where $\hat{y} \sim \in$, and (3) the blowoff region, where $-\hat{y} >> \in$.

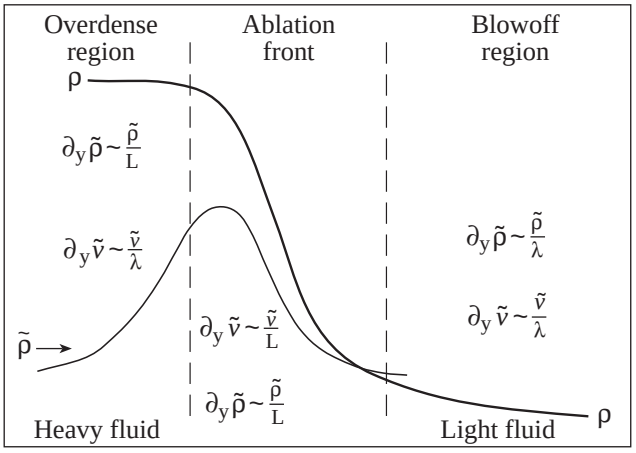

Figure 65.21
Density profile with regions of different scale lengths for the perturbations. Here λ is the mode wavelength.

Region 1: The Overdense Region

In ICF capsule implosions, the heavy-fluid region is the overdense portion of the shell where $\hat{y} \equiv ky \sim 1$, $\rho \simeq \rho_a$, $\xi \equiv \rho/\rho_a = 1 - \exp(-\hat{y}/\in) + O\left[\exp(-2\hat{y}/\in)\right]$, and $L >> L_0$. In this region and to lowest order in $\exp(-\hat{y}/\in)$, Eq. (10) reduces to a constant-coefficient fifth-order differential equation,

$$\left(\partial_{\hat{y}}^2 - 1\right)\left(\Gamma_a + \partial_{\hat{y}}\right)\left(\in \partial_{\hat{y}}^2 - \partial_{\hat{y}} + \Gamma_a - \in\right)\tilde{\Phi}^h \exp(\hat{y}/\in) = 0, \quad (11)$$

where $\Gamma_a = -\gamma/kV_a$ and the superscript h denotes the heavy-fluid region. The solution of Eq. (11) can be written in the following form:

$$\tilde{\Phi}^h = \left(a^h e^{-\hat{y}} + b^h e^{\alpha^- \hat{y}} + c^h e^{\hat{y}} + d^h e^{-\Gamma_a \hat{y}} + q^h e^{\alpha^+ \hat{y}}\right) e^{-\hat{y}/\epsilon}, \quad (12)$$

where a^h, b^h, c^h, d^h, q^h are integration constants and $\alpha^{\pm} = \left[1 \pm \sqrt{1 + 4\epsilon(\epsilon - \Gamma_a)}\right] / 2\epsilon$. In order to satisfy the boundary conditions of vanishing perturbations at $+\infty$, $c^h = d^h = q^h = 0$, and Eq. (12) reduces to the simple form

$$\tilde{\Phi}^h = \left(a^h e^{-\hat{y}} + b^h e^{\alpha^- \hat{y}}\right) e^{-\hat{y}/\epsilon}. \quad (13)$$

It is important to observe that the incompressible theory $(\nabla \cdot \tilde{\mathbf{v}} = 0)$ yields only the sonic solution

$$\tilde{\rho}_{\text{sonic}} \sim \exp\left[-\hat{y} - \hat{y}/\epsilon\right].$$

Equation (13) shows that a new solution is introduced by the finite thermal conductivity and, because of its diffusive character, we denote the second term in Eq. (13) as the diffusion or entropy solution. The asymptotic matching conditions can be greatly simplified by the following choice of the integration constants:

$$a^h = 1 - b^h, \qquad b^h = B^h - \hat{\beta}\frac{\epsilon^{1/\nu}}{\Gamma_a}, \quad (14)$$

where B^h, $\hat{\beta}$ must be determined from asymptotic matching, and the normalization condition $a^h + b^h = 1$ has been used. The heavy-fluid solution [Eq. (13)] can be rewritten using the ablation-front variable $z = \hat{y}/\epsilon$ and expanding α^- in powers of ϵ and $\epsilon\Gamma_a$,

$$\alpha^- \simeq \Gamma_a\left[1 - \frac{\epsilon^2}{\epsilon\Gamma_a} + \epsilon\Gamma_a - 2\epsilon^2 + 2(\epsilon\Gamma_a)^2 + \ldots\right]. \quad (15)$$

A short calculation yields

$$\tilde{\Phi}^h(\hat{y} \sim \epsilon) = e^{-z}\left[\Psi^h(\epsilon z) + \tilde{\chi}^h(\epsilon\Gamma_a, \epsilon, z)\right], \quad (16)$$

where $\Psi^h(\epsilon z)$ and $\tilde{\chi}^h(\epsilon\Gamma_a, \epsilon, z)$ can be written as an ϵ-series

$$\Psi^h(\epsilon z) = 1 - \epsilon z\left[1 - b^h(1 - \epsilon) + \hat{\beta}\epsilon^{1/\nu}\right] + \left(1 - b^h\right)\left[\epsilon^2\frac{z^2}{2} - \epsilon^3\frac{z^3}{6} + O(\epsilon^4)\right], \quad (17a)$$

$$\tilde{\chi}^h(\epsilon\Gamma_a, \epsilon, z) = \sum_{j=0}^{\infty} \tilde{\chi}_j(\epsilon\Gamma_a, z)\epsilon^j. \quad (17b)$$

It is important to observe that the parameter $\epsilon\Gamma_a$ is small for long-wavelength modes and large Froude numbers. Indeed, $\epsilon|\Gamma_a| = \epsilon\gamma/(kV_a) < \epsilon\gamma_{cl}/(kV_a) = \sqrt{\epsilon/Fr} \ll 1$. Thus, each term of the series in Eq. (17b) can be further expanded in powers of $\epsilon\Gamma_a$:

$$\tilde{\chi}_0^h = B^h(\epsilon\Gamma_a)z + b^h\left[(\epsilon\Gamma_a)^2\left(z + \frac{z^2}{2}\right) + (\epsilon\Gamma_a)^3\left(\frac{z^3}{6} + z^2 + 2z\right)\right] + b^h\left\{(\epsilon\Gamma_a)^4\left(\frac{z^4}{24} + \frac{z^3}{2} + \frac{5}{2}z^2 + 5z\right) + O\left[(\epsilon\Gamma_a)^5\right]\right\}, \quad (18a)$$

$$\tilde{\chi}_1^h = 0, \ \tilde{\chi}_2^h = -2b^h\left\{(\epsilon\Gamma_a)\left(z + \frac{z^2}{2}\right) + O\left[(\epsilon\Gamma_a)^2\right]\right\}. \quad (18b)$$

The next step is to solve Eq. (10) in the ablation-front region and asymptotically match that solution with Eq. (16).

Region 2: The Ablation-Front Region

The ablation front is the region where the density, velocity, and temperature profiles undergo sharp variations. In this region, $\hat{y} \sim \epsilon$, $L \sim L_0$, and $\xi \sim 1$. Since $\xi \equiv \rho/\rho_a \sim 1$, Eq. (8) cannot be analytically solved and an explicit expression for the spatial dependence of the density profile cannot be found. Thus, it is more convenient to use ξ as the independent variable in Eq. (10). By denoting $\tilde{\Phi}^a$ as the solution in the ablation region and after some straightforward manipulations, Eq. (10) can be rewritten in the following operator form:

$$\left[L_0 + \epsilon L_1 + \epsilon^2 L_2 + \epsilon^4 L_4\right]\tilde{\Phi}^a = 0, \quad (19)$$

where

$$L_0 = \partial_z(\in\Gamma + \partial_z)\partial_z\left[\in\Gamma\hat{L}\xi^\nu + \left(\hat{L}\partial_z + 1\right)\left(\xi^\nu + \partial_z\right)\right], \quad (20a)$$

$$L_1 = \frac{\xi^{\nu+2}}{\Gamma_c^2}\left(\in\Gamma_a\right)^2, \quad (20b)$$

$$L_2 = -\partial_z(\in\Gamma + \partial_z)\partial_z\hat{L} - (\in\Gamma + \partial_z)\hat{L}\left[(\in\Gamma + \partial_z)\xi^\nu + \partial_z^2\right] - \partial_z \in\Gamma, \quad (20c)$$

$$L_4 = \in\Gamma\hat{L} + \partial_z\hat{L} - 1, \quad (20d)$$

$\partial_z = \xi^{\nu+1}(1-\xi)\partial_\xi$, $\hat{L} = \xi^{-\nu}/(1-\xi)$, $\Gamma = \Gamma_a\xi$, $\Gamma_c \equiv \gamma\sqrt{k|g|}$, and $z = \hat{y}/\in$ is the ablation-front coordinate ($z \sim 1$ in the ablation-front region). Furthermore, each operator L_i can be expanded in powers of $\in\Gamma_a$, and the eigenfunction can be expressed as a double power series,

$$L_i = \sum_{j=0}^{\infty} L_{ij}\left(\in\Gamma_a\right)^j,$$
$$\tilde{\Phi}^a = \sum_{j=0}^{\infty} \tilde{\Phi}_j^a \in^j, \quad (21)$$
$$\tilde{\Phi}_j^a = \sum_{k=0}^{\infty} \tilde{\Phi}_{jk}^a\left(\in\Gamma_a\right)^k.$$

The next step is to solve Eq. (19) order by order. To lowest order in $\in$ and $\in\Gamma_a$, Eq. (19) yields

$$\tilde{\Phi}_{00}^a = A^a\Psi_0 + B^a\Psi_1 + C^a\Psi_2 + D^a\Psi_3 + E^a\Psi_4, \quad (22)$$

where A^a, B^a, C^a, D^a, and E^a are the integration constants. The five solutions can be written in the following integral forms:

$$\Psi_0 = \frac{1-\xi}{\xi}, \qquad \Psi_1 = \frac{1-\xi}{\xi}z(\xi), \quad (23a)$$

$$\Psi_2 = \frac{1-\xi}{\xi}\left\{\frac{z^2(\xi)}{2} + \frac{1}{\nu}\int_1^\xi \frac{T_\nu(\eta)}{\eta^{\nu+1}(1-\eta)^2}\,d\eta\right\}, \quad (23b)$$

$$\Psi_3 = \frac{1-\xi}{\xi}\left\{\frac{z^3(\xi)}{6} - \int_1^\xi \frac{d\eta}{\eta^{\nu+1}(1-\eta)^2}\int_1^\eta z(x)\frac{1-x^{\nu+1}}{x^{\nu+1}}dx\right\}, \quad (23c)$$

$$\Psi_4 = \frac{1-\xi}{\xi}\int_{\xi(0)}^\xi \frac{d\eta}{\eta^{\nu+1}(1-\eta)^2}, \quad (23d)$$

$$z(\xi) = \int_{\xi(0)}^\xi \frac{d\eta}{\eta^{\nu+1}(1-\eta)}, \quad (23e)$$

where $T_\alpha(x) = 1/x^\alpha + \alpha(x-1) - 1$, and $\xi(0)$ is the density at $z = 0$. To determine the integration constants, the solution in the ablation front must be asymptotically matched with the solution in the heavy-fluid region. This can be accomplished by taking the limit of $\xi \to 1 (z \to \infty)$ in Eq. (22). According to standard boundary layer theory, the asymptotic matching will occur if a common region of validity of the two solutions exists. Substituting $1-\xi = e^{-z} + O\left(e^{-2z}\right)$ and matching the lowest-order term of Eq. (22) with Eq. (16) yields $B^a = C^a = D^a = E^a = 0$, and $A^a = 1$. The first- and second-order matchings in $\in\Gamma_a$ yield $\tilde{\Phi}_{01}^a = B^h\Psi_1$, $\tilde{\Phi}_{02}^a = b^h\left(\Psi_1 + \Psi_2\right)$. The functions $\tilde{\Phi}_{03}^a$ and $\tilde{\Phi}_{04}^a$ can also be derived from Eq. (19) and, because of the lengthy expressions, they are reported in Appendix A.

The next step is to solve Eq. (19) to zeroth order in $\in\Gamma_a$ and first/second order in $\in$, i.e.,

$$L_{00}\tilde{\Phi}_{10}^a = 0 \quad \text{and} \quad L_{00}\tilde{\Phi}_{20}^a = -L_{20}\tilde{\Phi}_{00}^a.$$

Matching the $\in$ and $\in^2$ terms of the solutions with Eq. (16) yields

$$\tilde{\Phi}_{10}^a = -B_1^a\Psi_1, \quad \tilde{\Phi}_{20}^a = \frac{1-\xi}{\xi}\frac{z^2}{2} - b^h\Psi_2, \quad (24)$$

where $B_1^a = 1 - b^h(1-\in) + \hat{\beta}\in^{1/\nu}$. The functions $\tilde{\Phi}_{12}^a$ and $\tilde{\Phi}_{21}^a$ are important to describe the eigenfunction $\tilde{\Phi}^a$ to the desired accuracy; they are also reported in Appendix A.

Region 3: The Blowoff Region

The blowoff or expansion region is located downstream with respect to the ablation front. In this region, $-\hat{y} \sim 1$, $L >> L_0$, and $\xi \simeq \left(-L_0/\nu y\right)^{1/\nu} << 1$. The analysis can be simplified by introducing the new variable

$$\varsigma = \epsilon \Big/ \left(\nu \xi^{\nu}\right) = -\hat{y}\left[1 + O(\xi)\right],$$

and rewriting Eq. (10) in the following form:

$$\frac{1}{\nu} M_0 \tilde{\Phi}^l + \sigma M_1 \tilde{\Phi}^l + \sigma^2 M_2 \tilde{\Phi}^l = 0, \tag{25}$$

where $\sigma = \left[\left|\Gamma_a\right|^{\nu} (\epsilon/\nu)\right]^{-1/\nu}$, and the superscript *l* denotes variables in the low-density fluid,

$$M_0 = \left[\left(\partial_{\hat{y}} \frac{1}{\varsigma^{1/\nu}} \partial_{\hat{y}} - \frac{1}{\varsigma^{1/\nu}}\right) \frac{1}{1-\xi} + \frac{1}{\nu \in Fr \Gamma_a^2} \frac{1}{\zeta^{\frac{\nu+1}{\nu}}}\right] \frac{1}{\zeta^{1/\nu}}, \tag{26a}$$

$$\begin{aligned} M_1 = & -\partial_{\hat{y}} \hat{\nabla}^2 \frac{1}{\nu \zeta^{1/\nu}(1-\xi)} \\ & - \left[\partial_{\hat{y}} \frac{1}{\zeta^{1/\nu}} + \left(\partial_{\hat{y}} \frac{1}{\zeta^{1/\nu}} \partial_{\hat{y}} - \frac{1}{\zeta^{1/\nu}}\right) \frac{\zeta}{1-\xi}\right] \\ & \times \left(\partial_{\hat{y}} \frac{1}{\nu\zeta} + \hat{\nabla}^2\right), \end{aligned} \tag{26b}$$

$$M_2 = \frac{1}{\nu}\left(\partial_{\hat{y}}^4 + \partial_{\hat{y}}^3 \frac{1}{\nu\zeta} - 1\right) + \partial_{\hat{y}} \hat{\nabla}^2 \frac{\zeta}{1-\xi}\left(\partial_{\hat{y}} \frac{1}{\nu\zeta} + \hat{\nabla}^2\right), \tag{26c}$$

$\partial_{\hat{y}} = -(1-\xi)\partial_{\zeta}$, and $\xi = (\epsilon/\nu\zeta)^{1/\nu}$. Focusing on the values of $\nu > 1$, Eq. (25) yields different solutions according to the magnitude of $\sigma\nu$: (1) $\sigma\nu << 1$ and (2) $\sigma\nu >> 1$.

Solution 1: $\sigma\nu << 1$

Since the growth rate of the long-wavelength modes ($\epsilon << 1$) scales as the classical growth rate $\left(\gamma \sim \sqrt{kg}\right)$, the condition $\sigma\nu << 1$ can be rewritten in the following form:

$$\epsilon^{\frac{\nu-2}{\nu}} \nu^{\frac{2\nu+2}{\nu}} Fr << 1. \tag{27}$$

For large Froude numbers, Eq. (27) can be satisfied only for density profiles with $\nu > 2$ and wave numbers

$$\epsilon << \left(\frac{1}{\nu^{\frac{2\nu+2}{\nu}} Fr}\right)^{\frac{\nu}{\nu-2}}. \tag{28}$$

Since σ and $\epsilon^{1/\nu}$ are small, the differential operator and the eigenfunction can be expanded in powers of σ and $\epsilon^{1/\nu}$,

$$\begin{aligned} M_j &= \sum_{k=0}^{\infty} M_{jk} \epsilon^{k/\nu}, \\ \tilde{\Phi}^l &= \sum_{n=0}^{\infty} \tilde{\Phi}_n^l \sigma^n, \quad \tilde{\Phi}_n^l = \sum_{i=0}^{\infty} \tilde{\Phi}_{ni}^l \epsilon^{i/\nu}. \end{aligned} \tag{29}$$

Each term of the series satisfies the boundary condition $\tilde{\Phi}_{ni}^l(\zeta \to \infty) = 0$. Substituting Eq. (29) into Eq. (25) and collecting terms corresponding to the lowest power of σ and $\epsilon^{1/\nu}$ leads to $M_{00}\tilde{\Phi}_{00}^l = 0$, which results in

$$\left[\zeta \partial_{\zeta}^2 - \frac{1}{\nu}\partial_{\zeta} - \zeta + \frac{1}{\nu \in Fr \Gamma_a^2}\right] \tilde{\Phi}_{00}^l \zeta^{-1/\nu} = 0. \tag{30}$$

The solution of Eq. (30) satisfying the boundary conditions at infinity can be written in terms of the Kummers' confluent hypergeometric function $U(a, b, x)$,

$$\begin{aligned} \tilde{\Phi}_{00}^l &= C_l \zeta^{1/\nu} e^{-\zeta} U(a, b, 2\zeta), \\ a &= -\frac{1}{2\nu \in Fr \Gamma_a^2} - \frac{1}{2\nu}, \quad b = -\frac{1}{\nu}. \end{aligned} \tag{31}$$

The other terms of the series in Eq. (29) can be found from Eq. (25) in a similar manner. Particularly useful for matching is the term $\tilde{\Phi}_{10}^l$ that satisfies $M_{00}\tilde{\Phi}_{10}^l / \nu = -M_{10}\tilde{\Phi}_{00}^l$. However, because of its complexity, we simplify such an equation by assuming that, to lowest order in ϵ, $\epsilon^{1/\nu}$, and $\epsilon\Gamma_a$, the eigenvalue has the classical form $\gamma^2 = k|g|$. This assumption is verified later by the matching conditions. First, observe that for $\gamma^2 = k|g|$, Eq. (31) reduces to

$$\tilde{\Phi}_{00}^l = C_l \zeta^{1/\nu} e^{\zeta} \Gamma(1 + 1/\nu, 2\zeta),$$

where $\mathbf{\Gamma}(a, x)$ is the incomplete gamma function. By rewriting $M_{10} = -\hat{\nabla}^2 \zeta \hat{\nabla}^2 \zeta^{-1/\nu}$ and substituting $\tilde{\Phi}_{00}^l$ into Eq. (25), the equation for $\tilde{\Phi}_{10}^l$ can be solved in closed form, yielding

$$\tilde{\Phi}_{10}^l = \frac{2^{1/\mu} C_l}{\nu} e^{\zeta} \zeta^{1/\nu} \left[\Gamma(2/\nu, 2\zeta) - \nu\Gamma(1 + 2/\nu, 2\zeta)\right], \tag{32}$$

where $\mu = \nu/(\nu - 1)$. To achieve matching with the solution in

the ablation front, it is important to derive the asymptotic behavior of the solution in the blowoff region for small ζ. Combining Eqs. (31) and (32) leads to the following form of the eigenfunction:

$$\tilde{\Phi}^l_{00} + \sigma\tilde{\Phi}^l_{10} = C_l\zeta^{1/\nu}\left\{A_l\left(1+a_l\zeta+\ldots\right) - B_l\left(2\zeta\right)^{1+\frac{1}{\nu}}\left(1+b_l\zeta+\ldots\right) - 2^{1/\nu}\sigma\,\zeta^{2/\nu}\left(1+\zeta+\ldots\right)\right\}, \quad (33)$$

where

$$A_l = \frac{\Gamma\left[1+1/\nu\right]}{\Gamma\left[1+a+1/\nu\right]} - \frac{2^{1/\mu}\sigma}{\nu}\Gamma\left[\frac{2}{\nu}\right], \quad (34a)$$

$$a_l = \frac{1}{A_l}\left\{\frac{\Gamma\left[1+1/\nu\right]}{\Gamma\left[1+a+1/\nu\right]}\left(2\frac{a}{b}-1\right) - \frac{2^{1/\mu}\sigma}{\nu}\right\}, \quad (34b)$$

$$B_l = \frac{\nu}{\nu+1}\frac{\Gamma\left(-1/\nu\right)}{\Gamma\left[a\right]}, \qquad b_l = 2\frac{1+a}{b} - 3. \quad (34c)$$

Substituting $\zeta = \in\!/\left(\nu\xi^\nu\right)$, Eq. (33) can be rewritten as the sum of three power series in $\in$. It is important to observe that the power series in Eq. (33) cannot be matched with the $\in$ and $\in\Gamma_a$ power series of the ablation-front solution. This suggests that a transition region exists between the ablation front and the blowoff regions. The solution in such a region must match the ablation front as well as the blowoff region solution.

By introducing the layer variable $\eta = \zeta/\sigma^\mu$ and the operator $\partial_u = -\left(1-\xi\right)\partial_\eta$, Eq. (25) can be rewritten in the following form:

$$W_0\tilde{\Phi}^t + \Delta W_1\tilde{\Phi}^t + \Delta^2 W_2\tilde{\Phi}^t + \Delta^4 W_4\tilde{\Phi}^t = 0, \quad (35)$$

where $\Delta = \sigma^\mu$, the superscript t denotes the transition region, and

$$W_0 = \partial_u\left(\partial_u - \frac{1}{\eta^{1/\nu}}\right) \times \partial_u\left\{\frac{\eta}{1-\xi}\left[\left(\partial_u - \frac{1}{\eta^{1/\nu}}\right)\frac{1}{\nu\eta} + \partial_u^2\right] + \frac{1}{\nu}\partial_u + \frac{1}{\nu^2\eta}\right\}, \quad (36a)$$

$$W_1 = \frac{1}{\nu^2 \in Fr\Gamma_a^2}\,\frac{1}{\eta^{\frac{\nu+2}{\nu}}}, \quad (36b)$$

$$W_2 = \frac{1}{\nu}\partial_u\frac{1}{\eta^{1/\nu}} - \left(\partial_u - \frac{1}{\eta^{1/\nu}}\right)\frac{\eta}{1-\xi}\left[\partial_u^2 + \left(\partial_u - \frac{1}{\eta^{1/\nu}}\right)\frac{1}{\nu\eta}\right] - \partial_u\left(\partial_u - \frac{1}{\eta^{1/\nu}}\right)\partial_u\frac{\eta}{1-\xi}, \quad (36c)$$

$$W_4 = \left(\partial_u - \frac{1}{\eta^{1/\nu}}\right)\frac{\eta}{1-\xi} - \frac{1}{\nu}, \quad (36d)$$

and $\xi = \left(\in\!/\Delta\nu\eta\right)^{1/\nu}$. Observe that $\in\!/\Delta \sim \left(\in\!/Fr\right)^{\frac{\nu}{2(\nu-1)}} << 1$, and the variable $\xi \sim \left(\in\!/\Delta\right)^{1/\nu} << 1$. Thus, each operator W_i can be expanded in powers of $\left(\in\!/\Delta\right)^{1/\nu}$, and the eigenfunction $\tilde{\Phi}^t$ can be expanded in powers of Δ and $\left(\in\!/\Delta\right)^{1/\nu}$,

$$W_i = \sum_{n=0}^{\infty} W_{in}\left(\frac{\in}{\Delta}\right)^{n/\nu}, \qquad \tilde{\Phi}^t = \sum_{n=0}^{\infty}\tilde{\Phi}^t_n\Delta^n, \quad \tilde{\Phi}^t_n = \sum_{j=0}^{\infty}\tilde{\Phi}^t_{nj}\left(\frac{\in}{\Delta}\right)^{j/\nu}. \quad (37)$$

To lowest order in Δ and $\left(\in\!/\Delta\right)^{1/\nu}$, Eq. (35) reduces to $W_{00}\tilde{\Phi}^t_{00} = 0$, where

$$W_{00} = -\frac{1}{\nu^2}\partial_\eta\left(\partial_\eta + \frac{1}{\eta^{1/\nu}}\right) \times \partial_\eta\left(\nu^2\eta\partial_\eta^2 - 2\nu\partial_\eta + \frac{\nu+1}{\eta} - \frac{\nu}{\eta^{1/\nu}}\right). \quad (38)$$

This equation can be further simplified by introducing a new function $\tilde{\chi}^t = \tilde{\Phi}^t/\eta^{1/\nu}$ and by integrating three times with respect to η. A straightforward manipulation leads to the following second-order differential equation:

$$\nu\eta^{2-\frac{1}{\mu}}\partial_\eta^2\tilde{\chi}^t - \tilde{\chi}^t = A^t\int_0^\eta d\theta\; e^{-\mu\theta^{1/\mu}}\int_0^\theta d\phi\; e^{\mu\phi^{1/\mu}} + B^t\int_0^\eta d\theta\; e^{-\mu\theta^{1/\mu}} - C^t, \quad (39)$$

where A^t, B^t, C^t are the constants of integration. The solution of Eq. (39) can be written as a linear combination of the

homogeneous and particular solutions,

$$\tilde{\chi}^t = A^t\chi_A^P + B^t\chi_B^P + C^t\chi_C^P + D^t\chi_D^H + E^t\chi_E^H, \quad (40)$$

where $\chi_A^P, \chi_B^P, \chi_C^P$ are the particular solutions corresponding to each term in the right-hand side of Eq. (39) and χ_D^H, χ_E^H are the homogeneous solutions (D^t and E^t are integration constants). Next, we observe that $\chi_C^P = 1$ and we rewrite Eq. (39) for the other four solutions by introducing the new variable $\tau = \eta^{1/\mu}$. A short calculation yields

$$\nu\tau\partial_\tau^2\tilde{\chi}^t - \mu\partial_\tau\tilde{\chi}^t - \mu^2\tilde{\chi}^t = \mu^2\Pi(\tau), \quad (41a)$$

where

$$\Pi(\tau) = A^t\mu^2\int_0^\tau d\theta\left(\theta^{\mu/\nu}e^{-\mu\theta}\right)\int_0^\theta d\phi\left(\phi^{\mu/\nu}e^{\mu\phi}\right) + B^t\mu\int_0^\tau d\theta\left(\theta^{\mu/\nu}e^{-\mu\theta}\right). \quad (41b)$$

The homogeneous solutions can be easily calculated from Eq. (41a), yielding

$$\chi_D^H = \tau^{\mu/2}\,\mathbf{K}_\mu\left(2\mu\sqrt{\tau/\nu}\right), \qquad \chi_E^H = \tau^{\mu/2}\,\mathbf{I}_\mu\left(2\mu\sqrt{\tau/\nu}\right), \quad (42)$$

where $\mathbf{K}_\mu(x)$ and $\mathbf{I}_\mu(x)$ are the modified Bessel functions. To determine the two particular solutions χ_A^P and χ_B^P, Eq. (41a) is transformed in Laplace space,

$$\frac{d\hat{\chi}^t}{ds} + \left[\frac{2\nu+\mu}{\nu s} + \frac{\mu^2}{\nu s^2}\right]\hat{\chi}^t = A^tF_A(s) + B^tF_B(s). \quad (43)$$

The Laplace transforms of χ_A^P and χ_B^P are the particular solutions of Eq. (43):

$$\hat{\chi}_A^P = -\frac{\mu^4}{\nu}\Gamma(2\mu)\frac{e^{\mu^2/\nu s}}{s^{2+\frac{\mu}{\nu}}}\int_{1/s}^\infty\frac{e^{-\frac{\mu^2 x}{\nu}}}{(1+x\mu)^\mu}dx\int_0^x dy\left(y+\mu y^2\right)^{\mu/\nu}, \quad (44)$$

$$\hat{\chi}_B^P = -\mu\left(\frac{\mu}{\nu}\right)^\mu\frac{\Gamma(\mu)}{s^{2+\frac{\mu}{\nu}}}e^{\frac{\mu}{\nu}\left(1+\frac{\mu}{s}\right)}\Gamma\left[1-\mu,\frac{\mu}{\nu}\left(1+\frac{\mu}{s}\right)\right], \quad (45)$$

where

$$F_A(s) = -\frac{\mu^4}{\nu s^3}\frac{\Gamma(2\mu)}{(s+\mu)^\mu}\int_s^\infty\frac{(\omega+\mu)^{\mu/\nu}}{\omega^{2\mu}}d\omega, \qquad F_B(s) = -\frac{\mu^3}{\nu s^3}\frac{\Gamma(\mu)}{(s+\mu)^\mu}. \quad (46)$$

Here, $\mathbf{\Gamma}(x)$ is the gamma function and $\mu = \frac{\nu}{\nu-1}$. The behavior of the particular solutions for $\tau\to\infty$ and $\tau\to 0$ can be determined by expanding Eqs. (44) and (45) in proximity of the poles. A short calculation yields

$$\chi_A^P(\tau\approx 0) = \phi_1\tau^\mu\left[1+\frac{\mu}{2\nu-1}\tau+\cdots\right] + \phi_2\tau^{2\mu+1}\left[1-\frac{\nu}{2(3\nu-2)}\tau+\cdots\right], \quad (47a)$$

$$\chi_A^P(\tau\to\infty) = -\frac{\nu}{\nu+1}\tau^{2\mu-1}\left[1+\frac{\nu+1}{2\nu\tau}+\cdots\right], \quad (47b)$$

$$\chi_B^P(\tau\approx 0) = \theta_1\tau^\mu\left[1+\frac{\mu}{2\nu-1}\tau\cdots\right] + \theta_2\tau^{\mu+1}\left[1-\frac{\nu}{2(3\nu-2)}\tau\cdots\right], \quad (47c)$$

$$\chi_B^P(\tau\to\infty) = -\Gamma(\mu)\mu^{-\mu/\nu} - \frac{1}{\mu\nu}\tau^{\mu-2}e^{-\mu\tau}, \quad (47d)$$

where

$$\phi_1 = -\frac{\Gamma(2\mu)}{\nu-1}\Gamma\left(\frac{\nu+1}{1-\nu},\frac{\mu}{\nu}\right)\left(\frac{\in}{\nu}\right)^{\mu/\nu}, \qquad \phi_2 = \frac{\nu}{2(3\nu-1)(2\nu-1)}, \quad (48a)$$

$$\theta_1 = -\left(\frac{\mu}{\nu}\right)^\mu e^{\mu/\nu}\,\Gamma\left(-\frac{\mu}{\nu},\frac{\mu}{\nu}\right), \qquad \theta_2 = \frac{\nu}{(\nu-1)(2\nu-1)}. \quad (48b)$$

Equations (47) and (48) determine the lowest-order solution in the transition region. By inspection, one can immediately

conclude that the exponentially growing solution χ_E^H does not match the solution in the light-fluid region, and the χ_D^H generates an $\in\Gamma_a$ series for $\eta = \in/\nu\Delta\xi^\nu$ that cannot be matched by the ablation layer solution. Thus, we set $D^t = E^t = 0$ in Eq. (40) and rewrite the transition region solution as

$$\tilde{\Phi}_{00}^t = C^t\tilde{\Phi}_{00}^C + A^t\tilde{\Phi}_{00}^A + B^t\tilde{\Phi}_{00}^B,$$

where

$$\tilde{\Phi}_{00}^C = \eta^{1/\nu},\quad \tilde{\Phi}_{00}^A = \eta^{1/\nu}\chi_A^P,\ \text{and}\ \tilde{\Phi}_{00}^B = \eta^{1/\nu}\chi_B^P.$$

Some higher-order terms in the Δ and $\xi \sim (\in/\Delta)^{1/\nu}$ series are also important; they are reported in Appendix B.

The growth rate of the instability can be found by matching the solutions in the ablation front, the transition, and the blowoff region. First, we combine the terms of the transition region into a single function

$$\tilde{\Phi}^t = C^t\left(\tilde{\Phi}_0^C + \Delta\tilde{\Phi}_1^C + \Delta^2\tilde{\Phi}_{20}^C + \cdots\right) + A^t\left[\tilde{\Phi}_{00}^A + \Delta\tilde{\Phi}_{10}^A + \left(\frac{\in}{\nu\Delta}\right)^{1/\nu}\tilde{\Phi}_{01}^A + \cdots\right] + B^t\eta^{1/\nu}\chi_B^P. \quad (49)$$

Then, we rewrite the transition region solution near the ablation region by substituting $\eta = \in/\nu\,\Delta\xi^\nu$ into Eq. (49) and taking the limit of $\xi \to 0$,

$$\begin{aligned}\tilde{\Phi}^t(\eta\to 0,\xi\to 0) &= C^t\left(\frac{\in}{\Delta\nu}\right)^{1/\nu}\\ &\times\frac{1}{\xi}\left(1-\frac{\in}{\xi^\nu}\frac{kg}{\nu\gamma^2}+\frac{\in^2}{2\nu^2\xi^{2\nu}}+\cdots\right)\\ &+\left\{A^t\phi_1\left[1+O(\Delta,\xi)\right]+B^t\theta_1\right\}\left(\frac{\in}{\nu\Delta}\right)^{\frac{\nu+1}{\nu}}\frac{F_1(\xi)}{\xi^{\nu+1}}\\ &+A^t\phi_2\left(\frac{\in}{\Delta\nu}\right)^3\frac{F_2(\xi)}{\xi^{3\nu}}(1+Q_3\xi+\cdots)\\ &+B^t\left(\frac{\in}{\Delta\nu}\right)^2\frac{\theta_2}{\xi^{2\nu}}F_2(\xi). \end{aligned} \quad (50)$$

Equation (50) must match the ablation-front solution in the limit of $\xi \to 0$. The asymptotic behavior of the ablation-front solution near $\xi = 0$ can be obtained from the section covering the **Ablation-Front Region**, leading to

$$\begin{aligned}\tilde{\Phi}^a &\to \frac{R_0}{\xi} + \in\frac{R_1}{\xi^{\nu+1}} + \in^2\frac{1}{2\nu^2\xi^{2\nu+1}}\\ &-\in\Gamma_a\frac{B^h+\in\Gamma_a b^h Q_1}{\nu\xi^{\nu+1}}F_1(\xi) - \in^{2+\frac{1}{\nu}}\Gamma_a\frac{\hat{\beta}Q_2}{\xi^{2\nu}}\\ &\times\left(1+\frac{\in\Gamma_a}{\nu}\right)F_2(\xi)\\ &-\in^3\Gamma_a^2\left\{B_1^a+\frac{kg}{\gamma^2}-\hat{\beta}\in^{1/\nu}F_2(\xi)\left[1+Q_3\xi+\cdots\right]\right\}\frac{Q_4}{\xi^{3\nu}}, \end{aligned} \quad (51)$$

where

$$\begin{aligned}R_0 &= 1-\in z_0\left(1-b^h\right)+\in\Gamma_a B^h z_0,\\ R_1 &= \frac{1}{\nu}\left[B_1^a-\in z_0\left(1-b^h\right)-\in b^h\frac{\nu+1}{\nu}\right],\end{aligned} \quad (52a)$$

$$Q_1 = \frac{\nu z_0 - 1}{\nu},\quad Q_2 = \left[\nu(2\nu-1)(\nu-1)\right]^{-1}, \quad (52b)$$

$$\begin{aligned}Q_3 &= \frac{9\nu^3-11\nu^2+4\nu}{(\nu-1)^2(3\nu-2)},\\ Q_4 &= \left[2\nu^2(2\nu-1)(3\nu-1)\right]^{-1},\end{aligned} \quad (52c)$$

$$F_1(\xi) = 1-\frac{\in\Gamma_a}{(2\nu-1)(\nu-1)\xi^{\nu-1}} + \frac{(\in\Gamma_a)^2}{2(\nu-1)^2(2\nu-1)(3\nu-2)\xi^{2(\nu-1)}}+\cdots, \quad (52d)$$

$$F_2(\xi) = 1+\frac{\in\Gamma_a}{2(3\nu-2)\xi^{\nu-1}}+\cdots. \quad (52e)$$

Here, $z_0 = \sum_{n=0}^{\infty}\xi(0)^{n-\nu}/(\nu-n)$. Matching Eq. (50) with Eq. (51) yields the following set of equations:

$$R_0 = C^t\left(\frac{\in}{\nu\Delta}\right)^{1/\nu},\qquad -\frac{kg}{\gamma^2} = \frac{\nu R_1}{R_0}, \quad (53a)$$

$$B^h = -\left(\frac{\in}{\nu\Delta}\right)^{1/\nu}\frac{A^t\phi_1\left[1+O(\Delta,\xi)\right]+B^t\theta_1}{\Delta\Gamma_a\left(1+\in\Gamma_a Q_1/B^h\right)}, \quad (53b)$$

$$B^t = \nu^{1/\nu}\Delta^{\frac{\nu+1}{\nu}}\hat{\beta}\left(1+\frac{\in\Gamma_a}{\nu}\right), \tag{53c}$$

$$-\frac{kg}{\gamma^2} = 1 - b^h(1-\in) + \frac{A^t}{\Delta^3\Gamma_a^2}. \tag{53d}$$

The next step is to match the solutions for the transition and blowoff regions. Taking the limit of Eq. (48) for $\eta \to \infty$ and $\Delta \to 0$ yields

$$\begin{aligned}&\tilde{\Phi}^t(\eta\to\infty,\Delta\to 0)\\ &=\left[C^t - \Gamma(\mu)\mu^{\frac{1}{1-\nu}}B^t - \phi_1 A^t\left(\frac{\in}{\nu\Delta}\right)^{1/\nu}\right]\eta^{1/\nu}\left[1+O(\Delta\eta)\right]\\ &\quad -A^t\frac{\nu}{\nu+1}\left(1+\frac{kg}{\gamma^2}\phi_1\right)\eta^{1+\frac{2}{\nu}}\left[1+O(\Delta\eta)\right].\end{aligned} \tag{54}$$

Upon the substitution $\zeta = \Delta\eta$, the terms of this equation must match the powers of η in Eq. (33). A short calculation yields

$$\begin{aligned}&A^t\left(\frac{\in}{\nu\Delta}\right)^{1/\nu} = \Sigma^l\,\Delta^{\frac{\nu+1}{\nu}}R_0,\\ &\Sigma^l = 2^{\frac{\nu+1}{\nu}}\frac{\nu+1}{\nu}\frac{B^l}{A^l}\frac{1+O\left(\in^{1/\nu}\Delta\right)}{1+\frac{kg}{\gamma^2}\phi_1\Delta}.\end{aligned} \tag{55}$$

Equations (53) and (55) determine the order of magnitude of the constants. It is easy to show that $B^h \sim \Delta^{1/\nu}/\Gamma_a << 1$, $B^t \sim \Delta^{(\nu+1)/\nu} \sim A^t\xi << A^t$, and $\hat{\beta} \sim 1$. Equations (53) and (55) can be used to determine the instability growth rate and the parameter $\hat{\beta}$. Retaining all terms up to order $\in\Gamma_a B^h$ and $\in$, the instability growth rate satisfies the following equation:

$$\gamma(k << k_c) = \sqrt{A_T\,k|g|} - \beta k V_a, \tag{56}$$

where

$$A_T = \frac{1-\mu_0\in^{1/\nu}}{1+\mu_0\in^{1/\nu}},\quad \mu_0 = \frac{(2/\nu)^{1/\nu}}{\Gamma\left(\frac{\nu+1}{\nu}\right)},\quad \beta = \frac{\Gamma\left(\frac{\nu+2}{\nu}\right)}{\Gamma^2\left(\frac{\nu+1}{\nu}\right)}. \tag{57}$$

Equation (56) represents the growth rate of the instability for $\nu > 2$ and

$$k\,L_0 << \left[\nu^{(2\nu+2)/\nu}Fr\right]^{\nu/(2-\nu)}.$$

Solution 2: $\sigma\nu >> 1$

For $\sigma\nu >> 1$, the solution of Eq. (25) can be determined by following the procedure described in Ref. 16. The differential operators and the eigenfunction are expanded in powers of $1/\nu$:

$$M_i = \sum_{n=0}^{\infty} M_{in}\left(\frac{1}{\nu}\right)^n, \qquad \tilde{\Phi}^l = \sum_{n=0}^{\infty}\tilde{\Phi}_n^l(\hat{y})\left(\frac{1}{\nu}\right)^n, \tag{58}$$

where i = 0,1,2. Substituting Eq. (58) into Eq. (25) and collecting terms up to the first two orders in $1/\nu$ yields the following equations:

$$\left(\Gamma_a\delta + \partial_{\hat{y}}\right)\left(\partial_{\hat{y}}^2 - 1\right)\varsigma\left(\partial_{\hat{y}}^2 - 1\right)\tilde{\Phi}_0^l = 0, \tag{59}$$

$$\begin{aligned}&\left(\Gamma_a\delta+\partial_{\hat{y}}\right)\left(\partial_{\hat{y}}^2-1\right)\varsigma\left(\partial_{\hat{y}}^2-1\right)\tilde{\Phi}_1^l + \left(\Gamma_a\delta+\partial_{\hat{y}}\right)\left(\partial_{\hat{y}}^2-1\right)\varsigma\partial_{\hat{y}}\frac{\tilde{\Phi}_0^l}{\varsigma}\\ &+\left\{\Gamma_a\delta\left(\Gamma_a\delta+\partial_{\hat{y}}\right) - \frac{\delta}{1-\delta}\left(\Gamma_a\delta+\partial_{\hat{y}}\right)\left(\partial_{\hat{y}}^2-1\right)\varsigma\ln\varsigma\right.\\ &\left.-\Gamma_a\delta\left(\partial_{\hat{y}}\ln\varsigma\partial_{\hat{y}} - \ln\varsigma\right)\varsigma + (1-\delta)\left[\partial_{\hat{y}}\left(\Gamma_a\delta+\alpha_{\hat{y}}\right)+1\right]\right\}\\ &\times\left(\partial_{\hat{y}}^2-1\right)\tilde{\Phi}_0^l = 0,\end{aligned} \tag{60}$$

where

$$\delta = (\in/\nu)^{1/\nu},\quad \varsigma = \in\Big/\left(\nu\xi^\nu\right),\ \text{and}\ \ \partial_{\hat{y}} = -(1-\xi)\partial_\varsigma.$$

The function $\tilde{\Phi}_0^l$ can be written as a combination of the three decaying homogeneous solutions of Eq. (59):

$$\tilde{\Phi}_0^l = A^l\tilde{\Phi}_A^l + B^l\tilde{\Phi}_B^l + C^l\tilde{\Phi}_C^l,$$

where

$$\tilde{\Phi}_A^l = e^{\hat{y}},\quad \tilde{\Phi}_B^l = e^{-\hat{y}}\int_{-\infty}^{\hat{y}} dx e^{2x}\int^x\frac{d\eta}{\varsigma(\eta)}, \tag{61a}$$

$$\tilde{\Phi}_C^l = e^{\hat{y}} \int_0^{\hat{y}} dx e^{-2x} \int_{-\infty}^{x} d\eta \frac{e^{2\eta} - e^{\eta(1-\Gamma_a\delta)}}{\varsigma(\eta)}. \quad (61b)$$

The next step is to determine the coefficients A^l, B^l, C^l by matching the solution $\tilde{\Phi}_0^l$ with the ablation-front solution $\tilde{\Phi}^a$. Using the $1/\nu$ expansion of the ablation-front solution,

$$\begin{aligned}\tilde{\Phi}^a = {} & \frac{1-\delta}{\delta} + \frac{1}{\nu}\frac{\ln\varsigma}{\delta} + \frac{\varsigma}{\delta}\left[1 - b^h\left(1+\Gamma_a\right)\right] \\ & \times\left[1 + \frac{1}{\nu}\left(\ln\varsigma + \frac{\delta}{1-\delta}\right)\right] \\ & + \frac{\varsigma^2}{2(1-\delta)^2}\left\{\frac{1-\delta}{\delta} + \frac{1}{\nu}\left[2 - b^h\left(1-\Gamma_a^2\right) + \left(\frac{1}{\delta} - 2\right)\ln\varsigma\right]\right\} \\ & + \frac{\varsigma^3}{6\delta(1-\delta)^2}\left\{1 - b^h\left(1+\Gamma_a\right) + \frac{1}{2\nu}\left[\left(1 - b^h\left[1+\Gamma_a\right]\right)\right.\right. \\ & \times\frac{1+5\delta+2\ln\varsigma(1-3\delta)}{(1-\delta)} \\ & \left.\left. + \frac{\delta}{\in Fr} - \Gamma_a\delta\left[\Gamma_a - b^h\left(1+\Gamma_a\right)\right]\right\} + O\left(\frac{1}{\nu^2}\right),\end{aligned} \quad (62)$$

and matching the lowest power of $1/\nu$ in $\tilde{\Phi}^a$ and $\tilde{\Phi}_0^l$ yields $A^l = (1-\delta)/\delta$, $B^l = C^l = 0$.

The first-order correction $\tilde{\Phi}_1^l$ can be obtained by solving Eq. (60),

$$\tilde{\Phi}_1^l = \frac{\ln\varsigma}{\delta} e^{\hat{y}} + (1-\delta) C_1^l \tilde{\Phi}_C^l. \quad (63)$$

The constants C_1^l, b^h, and the dispersion relation are determined by matching $\tilde{\Phi}_0^l$ and $\tilde{\Phi}_1^l$ with Eq. (62):

$$\begin{aligned} b^h &= \frac{2}{1+\Gamma_a}\left[1 - \frac{\delta}{\nu(1-\delta)}\ln\left(\frac{2}{1-\delta\Gamma_a}\right)\frac{1-\Gamma_a}{1+\delta\Gamma_a}\right], \\ C_1^l &= 2\frac{1-\Gamma_a}{1+\delta\Gamma_a}, \end{aligned} \quad (64)$$

$$\Gamma_a^2 - \frac{4}{1+\delta}\Gamma_a - \left(\frac{1-\delta}{\in Fr(1+\delta)} - \frac{1}{\delta}\right) = 0. \quad (65)$$

Solving Eq. (65) yields the growth-rate formula:

$$\gamma = \sqrt{A_T^0 k|g| - \left(A_T^0\right)^2 k^2 V_a V_{bo}^0} - \left(1 + A_T^0\right) kV_a, \quad (66)$$

where

$$A_T^0 = \frac{1 - (\in/\nu)^{1/\nu}}{1 + (\in/\nu)^{1/\nu}}, \qquad V_{bo}^0 = \frac{V_a}{(\in/\nu)^{1/\nu}}. \quad (67)$$

Note the different coefficients of $\in^{1/\nu}$ in the Atwood numbers defined by Eqs. (67) and (57). It is important to remember that Eq. (66) has been derived using the $1/\nu$ expansion and, to the lowest order in $1/\nu$, $\mu_0 = (1/\nu)^{1/\nu}$ and $A_T^0 = A_T$. Furthermore, replacing A_T^0 with A_T and V_{bo}^0 with $V_a/\left(\mu_0 \in^{1/\nu}\right)$ in Eq. (66) would also reproduce the cutoff wave number obtained in Ref. 16 by including the higher-order corrections in $1/\nu$. Thus, we conclude that replacing $(\in/\nu)^{1/\nu}$ with $\mu_0 \in^{1/\nu}$ in Eq. (66) improves the accuracy of the growth-rate formula up to the first order in $1/\nu$:

$$\gamma = \sqrt{A_T k|g| - A_T^2 k^2 V_a V_{bo}} - (1 + A_T) kV_a, \quad (68)$$

where

$$V_{bo} = \frac{V_a}{\mu_0 \in^{1/\nu}}, \quad A_T = \frac{1 - \mu_0 \in^{1/\nu}}{1 + \mu_0 \in^{1/\nu}}. \quad (69)$$

Although Eq. (68) is valid over a large range of ν's > 1, a significant degradation of its accuracy is expected to occur for $\nu \to 1$, where the $1/\nu$ expansion breaks down. This problem is addressed in the next section, where the range of validity of the growth-rate formulas is discussed.

Summary of the Growth-Rate Formulas for *Fr* >> 1

For values of $\nu > 2$, two different growth-rate formulas have been derived according to the magnitude of the wave number:

$$\gamma = \sqrt{A_T k|g|} - \beta kV_a, \text{ for } kL_0 << \left(\nu^{2+\frac{2}{\nu}} Fr\right)^{\frac{\nu}{2-\nu}}, \quad (70a)$$

and

$$\gamma = \sqrt{A_T k|g| - A_T^2 k^2 V_a V_{bo}} - (1 + A_T) kV_a, \text{ for } kL_0 >> \left(\nu^{2+\frac{2}{\nu}} Fr\right)^{\frac{\nu}{2-\nu}}, \quad (70b)$$

where A_T, β, and V_{bo} are defined by Eqs. (57) and (69), respectively.

For values of $1 < \nu < 2$, the analysis of the previous section still applies. However, because corrections due to higher orders of $1/\nu$ are not included in the derivation, the growth-rate formula [Eq. (68)] shows poor agreement with the numerical results for $\nu < 1.5$. Figure 65.22(a) shows the unstable spectrum obtained by Eq. (68) and the numerical results of Ref. 5 for $\nu = 1.5$, 1.2, and 1.15. Note the degradation in accuracy of the analytic growth rate for $\nu < 1.5$. The analytic formula can be improved by observing that, for $\nu \to 1$, the cutoff wave number is so small that the $\epsilon^{1/\nu}$ corrections can be neglected in the analysis and the eignevalue equation can be numerically solved in the blowoff region. It is found that by modifying μ_0 to $\mu_0 + 0.12/\nu^2$, the matching conditions are satisfied over a large range of Froude numbers and $\nu \to 1^+$, thus leading to a general growth-rate formula valid for $1 < \nu < 2$:

$$\gamma = \sqrt{A_T k|g| - A_T^2 k^2 V_a V'_{bo}} - (1 + A_T) kV_a, \qquad (71a)$$

where

$$V'_{bo} = \frac{V_a}{\mu'_0 \epsilon^{1/\nu}}, \qquad \mu'_0 = \mu_0 + \frac{0.12}{\nu^2}, \qquad (71b)$$

and A_T is defined by Eq. (57). Figure 65.22(b) shows that for values of ν close to unity, excellent agreement is obtained between the numerical results of Ref. 5 and the modified formula [Eq. (71)].

Discussion

The validity of the asymptotic formula has been tested by comparing the growth rate obtained from Eqs. (70) and (71) with the numerical results of Ref. 5, where the isobaric model is numerically solved. Figure 65.23 shows plots of the normalized growth rate $\gamma L_0/V_a$ calculated using Eq. (70) (solid lines) and one numerically derived in Ref. 5 for $\nu = 2.5$ for different values of the Froude number (dots). Remarkable agreement between numerical and analytical results is obtained. In Fig. 65.24, the analytic growth rate is compared with the numerical results of Ref. 5 for different values of ν and fixed Froude number. The solid lines represent the result of the analytic theory and the dots are the numerical results. The analytic formula [Eq. (70)] is also compared with the self-consistent growth rate derived in Ref. 13. A significant disagreement between the results of Ref. 13 and Eq. (70) is found for large values of ν. Figure 65.25 shows the plot of the unstable spectrum for $\nu = 8$ obtained from the numerical computations of Kull[4] (dashed line), Eq. (70) (solid line), and the growth-rate formula of Ref. 13 with zero Mach number (dotted line).

Next, Eq. (70) is compared with other growth-rate formulas obtained by fitting numerical results. The most commonly used formula has been derived by Takabe *et al*. in Ref. 6 for spherical geometry, electronic heat conduction ($\nu = 2.5$), and large values of the Froude number. Following Ref. 6, the numerically derived growth rate can be fitted by the following formula:

$$\gamma = \alpha_T \sqrt{kg} - \beta_T kV_a, \qquad (72)$$

where

$$\alpha_T = 0.9\, G^{-0.02},$$

$$\beta_T = 2.3\left(\frac{\rho_a}{\rho_s}\right)^{0.075} G^{-0.2}, \qquad (73)$$

$$G = gr_s/c_s^2,$$

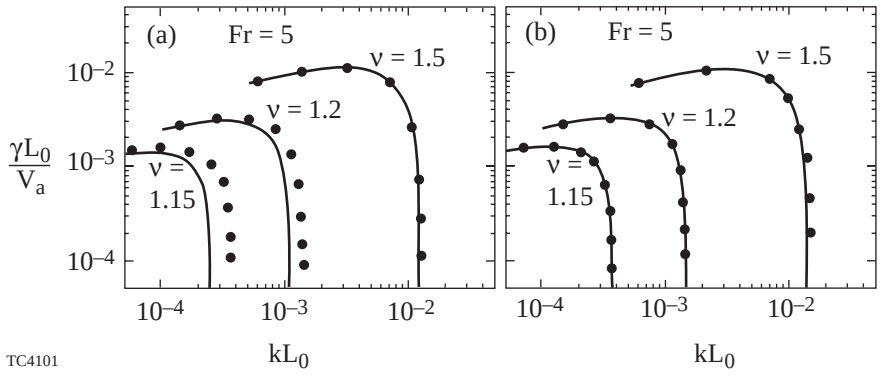

Figure 65.22
Unstable spectrum ($\gamma L_0/V_a$ versus kL_0) calculated using (a) Eq. (68) and (b) Eq. (71) (solid lines) compared with the numerical results of Ref. 5 (dots) for $\nu = 1.5$, 1.2, and 1.15 and $Fr = 5$.

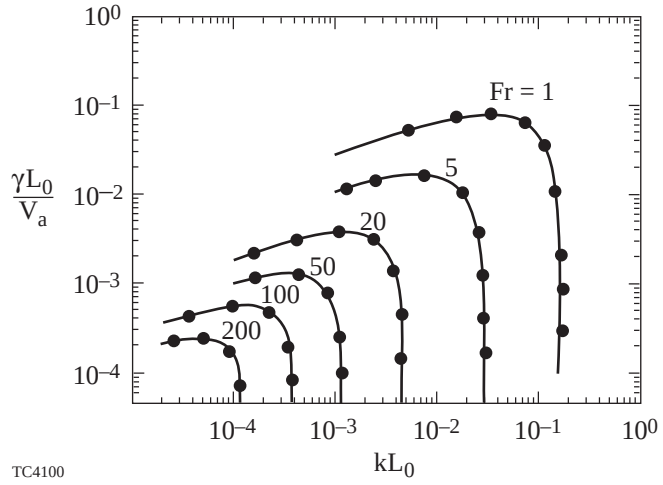

Figure 65.23
Unstable spectrum ($\gamma L_0/V_a$ versus kL_0) calculated using Eq. (70) (solid lines) compared with the numerical results of Ref. 5 (dots) for $\nu = 2.5$.

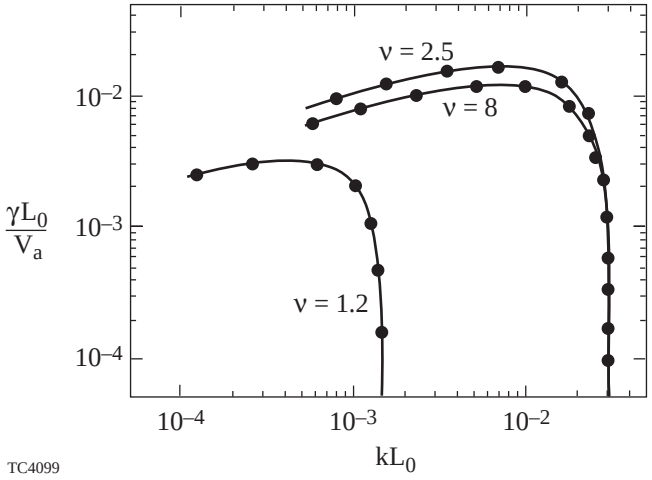

Figure 65.24
Unstable spectrum ($\gamma L_0/V_a$ versus kL_0) calculated using Eqs. (70) and (71) (solid lines) compared with the numerical results of Ref. 5 (dots) for $\nu = 1.2$, 2.5, 8 and $Fr = 5$.

and ρ_s, c_s, and r_s are the sonic density, sound speed, and position of the sonic point, respectively. Since α_T is almost independent of the equilibrium parameters ($\alpha_T \simeq 0.9$), we focus our attention on β_T. It is important to remember that, while Eqs. (72) and (73) have been derived for spherical geometry including finite Mach number, Eq. (70) is valid for slab geometry, neglecting the Mach number. Since the only isobaric dimensionless parameter is the Froude number, the coefficient β_T must be rewritten in terms of Fr. Using the isobaric profiles [Eq. (9)], we define y_s as the distance at which $\xi(y_s) = \rho_s/\rho_a \simeq (L_0/\nu y_s)^{1/\nu} << 1$, and correlate the parameter G to the Froude number,

$$G = \frac{0.4}{Fr}\,\frac{r_s}{y_s}\left(\frac{r_s}{r_a}\right)^4\left(\frac{\rho_a}{\rho_s}\right)^{0.5}, \qquad (74)$$

where r_a is the radial location of the peak density. Table I of Ref. 5 shows values of the relevant dimensionless parameters for $G = 2$. According to these values, Takabe's coefficients can be rewritten in the following form:

$$\beta_T = 1.8\,\theta\, Fr^{0.2},$$
$$\theta = \left(\frac{10\,y_s}{3\,r_s}\right)^{0.2}\left(\frac{10\,r_a}{9\,r_s}\right)^{0.8}\left(\frac{50\,\rho_s}{\rho_a}\right)^{0.025}. \qquad (75)$$

Observe that θ is very weakly dependent on the equilibrium parameters, and its values are always close to unity $(\theta \simeq 1)$. Table 65.I shows the values of θ corresponding to the equili-

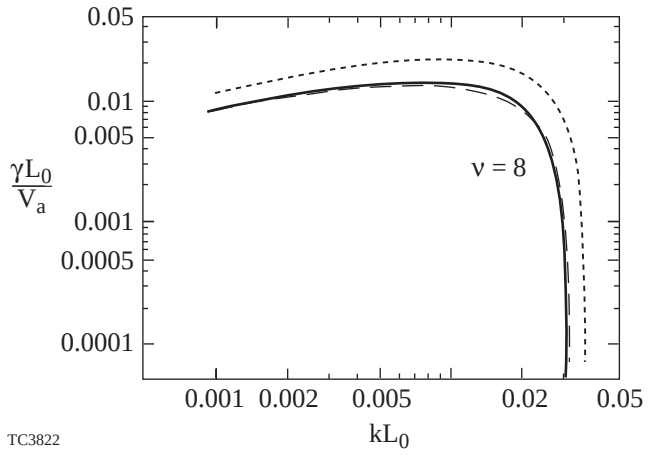

Figure 65.25
Plot of the normalized growth rate versus $\in$ for $\nu = 8$ and $Fr = 5$. The solid line represents Eq. (70), the dashed line is the numerical result of Ref. 5, and the dotted line is Eq. (16) of Ref. 13.

Table 65.I: Equilibrium parameters of Refs. 5 and 6.

$G = 2$				
r_a/r_s	Fr	ρ_a/ρ_s	y_s/r_s	θ
0.899	5.88	25.0	0.26	0.99
0.903	7.14	50.0	0.30	1.00
0.904	8.70	98.0	0.34	1.01

bria in Table I of Ref. 5. Since θ is approximately constant, the coefficient β depends mainly on the Froude number. The next step is to find the best fit ($\gamma_{\rm fit}$) for Eq. (70) based on a formula similar to Takabe's $\left(\gamma_{\rm fit} = a\sqrt{kg} - bkV_a\right)$. The fitting procedure is straightforward. The error $\left(\gamma - \gamma_{\rm fit}\right)^2$ is minimized over the portion of the unstable spectrum of interest to ICF ($1\ \mu{\rm m} < \lambda < 200\ \mu{\rm m}$). Since the typical cutoff wavelength λ_c is of the order of $1\ \mu$m, the minimization condition can be written in the convenient form

$$\frac{\partial \varepsilon}{\partial a} = 0, \qquad \frac{\partial \varepsilon}{\partial b} = 0, \quad \varepsilon = \int_{\lambda_c}^{200\lambda_c} \left(\gamma - \gamma_{\rm fit}\right)^2 d\lambda . \quad (76)$$

The two minimizing conditions yield the values of a and b that are subsequently fit with a power law formula ($a \sim Fr^{\mu_a}$ and $b \sim Fr^{\mu_b}$). For the values of Fr reported in Table I of Ref. 5 ($5 < Fr < 9$), the described procedure leads to the following fit of Eq. (70):

$$\gamma_{\rm fit} = 0.9\, Fr^{0.03}\sqrt{kg} - 2.0\, Fr^{0.15}\, kV_a . \quad (77)$$

The good agreement between Eqs. (77) and (72) confirms the accuracy of the analytic derivation. Furthermore, the general analytic formulas [Eqs. (70) and (71)] are valid for any $\nu > 1$ and can be applied to configurations that are not described by pure electron heat conduction.

Conclusions

The stability analysis of accelerated ablation fronts is carried out self-consistently for an arbitrary power law dependence of the thermal conductivity ($\kappa \sim T^{\nu}$ with $\nu > 1$) and large Froude numbers ($Fr > 1$). The eigenvalue equation is solved in different regions of the density profile (overdense, ablation, and blow-off regions), and the solution is asymptotically matched. The growth-rate formula is derived from the matching conditions, and its validity has been tested against the numerical results of Ref. 5. The excellent agreement between the growth-rate formula and the numerical results shows the high level of accuracy of the analytic derivation.

ACKNOWLEDGMENT

This work was supported by the U.S. Department of Energy Office of Inertial Confinement Fusion under Cooperative Agreement No. DE-FC03-92SF19460, the University of Rochester, and the New York State Energy Research and Development Authority. The support of DOE does not constitute an endorsement by DOE of the views expressed in this article.

Appendix A: Higher-Order Correction to $\tilde{\Phi}$ in the Ablation-Front Region

In this appendix, important higher-order corrections to the eigenfunction in the ablation-front region are reported. Those corrections are terms of Eq. (21), and they are derived by solving Eq. (19) order by order. After a very lengthy calculation, these terms can be written in the following convenient form:

$$\tilde{\Phi}^a_{03} = \frac{1-\xi}{\xi}\left\{ b^h\left[\frac{z^3}{6} + z^2 + 2z - \int_1^{\xi} \frac{G_{03}(\eta)}{\eta^{\nu+1}(1-\eta)^2}\, d\eta\right] - \frac{\hat{\beta}\,\epsilon^{1/\nu}}{\Gamma_a} K_{03}(\xi)\right\}, \quad (A1)$$

$$\tilde{\Phi}^a_{04} = \frac{1-\xi}{\xi}\left\{ b^h\left[\frac{z^4}{24} + \frac{z^3}{2} + \frac{5z^2}{2} + 5z\right] - \int_1^{\xi} \frac{d\eta}{\eta^{\nu+1}(1-\eta)^2} \int_1^{\eta} dx \left(b^h G_{04} - \frac{\hat{\beta}\,\epsilon^{1/\nu}}{\nu\Gamma_a} K_{04}\right)\right\}, \quad (A2)$$

$$\tilde{\Phi}^a_{11} = 0, \qquad \tilde{\Phi}^a_{21} = \tilde{\Phi}^{par}_{21} - 2b^h\left(\Psi_1 + \Psi_2\right), \quad (A3)$$

$$\tilde{\Phi}^{par}_{21} = \frac{1-\xi}{\xi}\int_1^{\xi} \frac{d\eta}{\eta^{\nu+1}(1-\eta)^2} \int_1^{\eta} dx \left\{ \frac{b^h}{\nu}\int_1^x \frac{T_{\nu-1}(y)}{y^{\nu+1}(1-y)^2}\, dy + B^h G_{21}(x)\right\}, \quad (A4)$$

$$\tilde{\Phi}^a_{12} = \left[B^a_1 + \frac{kg}{\gamma^2}\right]\frac{1-\xi}{\nu\xi}\int_1^{\xi} \frac{d\eta}{\eta^{\nu+1}(1-\eta)^2} \int_1^{\eta} dx \int_1^x \frac{1-y^{\nu}}{y^{2\nu+1}(1-y)}\, dy, \quad (A5)$$

where $T_a(x)$ is derived in the section on the **Ablation-Front Region** and

$$G_{03}(\eta)=\int_1^\eta dx\left[\left(\frac{1}{x^{\nu+1}}-1\right)(z+2)+\right.$$

$$\left.\frac{1}{\nu}\int_1^x \frac{T_\nu(y)}{y^{\nu+1}(1-y)^2}dy\right], \quad \text{(A6)}$$

$$K_{03}(\xi)=\frac{1}{\nu}\int_1^\xi \frac{d\eta}{\eta^{\nu+1}(1-\eta)^2}$$

$$\int_1^\eta dx\int_1^x \frac{1-y^\nu}{y^{2\nu+1}(1-y)}dy, \quad \text{(A7)}$$

$$G_{04}(x)=\left(\frac{1}{x^{\nu+1}}-1\right)\left(\frac{z^2}{2}+3z+5\right)$$

$$-\int_1^x \frac{dy}{y^{\nu+1}(1-y)^2}G_{03}(y), \quad \text{(A8)}$$

$$K_{04}(x)=\int_1^x \frac{dy}{y^{\nu+1}(1-y)}$$

$$\left[\int_1^y \frac{ds}{s^{2\nu}}\frac{1-s^\nu}{1-s}+\frac{1}{1-y}\int_1^y ds\int_1^s \frac{1-r^\nu}{r^{2\nu+1}(1-r)}dr\right], \quad \text{(A9)}$$

$$G_{21}(x)=-\frac{1}{\nu+1}\int_1^x \frac{y^{\nu+1}-1}{y^{2\nu+2}(1-y)}dy+z\left(\frac{1}{x^{\nu+1}}-1\right). \quad \text{(A10)}$$

Note that these corrections are essential to the derivation of Eqs. (51) and (62).

Appendix B: Higher-Order Correction to $\tilde{\Phi}$ in the Transition Region

In this appendix, the higher-order corrections to the eigenfunction in the transition region are reported. Those corrections are terms of Eq. (37), and they are derived by solving Eq. (35) order by order. The ξ and Δ corrections to $\tilde{\Phi}_{00}^C$ and $\tilde{\Phi}_{00}^A$ can be written in the following form:

$$\tilde{\Phi}_0^C=\eta^{1/\nu}(1-\xi), \quad \text{(B1)}$$

$$\tilde{\Phi}_1^C=-\frac{kg}{\gamma^2}\eta^{1/\nu}(1-\xi)\int_0^\eta \frac{d\eta}{1-\xi}, \quad \text{(B2)}$$

$$\tilde{\Phi}_2^C=\frac{1}{2}\eta^{2+\frac{1}{\nu}}\left[1+\frac{\nu+1}{\nu-1}\xi+O\left(\xi^2\right)\right]+O\left(1-\frac{kg}{\gamma^2}\right), \quad \text{(B3)}$$

$$\tilde{\Phi}_{10}^A=\frac{kg}{\gamma^2}\eta^{1/\nu}\chi_E^H(\eta)\int_\infty^\eta \frac{dx}{\left[\chi_E^H(x)\right]^2}$$

$$\int_0^x \frac{H_{10}(y)\chi_E^H(y)}{\nu y^{1+\frac{1}{\nu}}}dy+\frac{kg}{\gamma^2}\phi_1\tilde{\Phi}_{00}^A(\eta), \quad \text{(B4)}$$

$$\tilde{\Phi}_{01}^A=\eta^{1/\nu}\chi_E^H(\eta)\int_\infty^\eta \frac{dx}{\left[\chi_E^H(x)\right]^2}\int_0^x \frac{H_{01}(y)\chi_E^H(y)}{\nu y^{1+\frac{1}{\nu}}}dy$$

$$+\phi_1\eta^{1/\nu}\left[\frac{2}{\Gamma(\mu)}\left(\frac{\mu}{\sqrt{\nu}}\right)^\mu \chi_D^H(\eta)-1\right], \quad \text{(B5)}$$

where χ_E^H, χ_D^H, and $\tilde{\Phi}_{00}^A$ are defined in **Solution 2: $\sigma\nu >> 1$,** and

$$H_{10}(y)=-\int_0^y drH_{00}(r)+\int_0^y d\theta e^{-\mu\theta^{1/\mu}}$$

$$\int_0^\theta d\phi\left[\phi-\partial_\phi\chi_A^P(\phi)\right]e^{\mu\phi^{1/\mu}}, \quad \text{(B6)}$$

$$H_{00}(r)=\int_0^r d\theta e^{-\mu\theta^{1/\mu}}\int_0^\theta d\phi e^{\mu\phi^{1/\mu}}, \quad \text{(B7)}$$

$$H_{01}(\eta)=\left(\frac{2}{\eta^{1/\nu}}-\frac{\nu+1}{\nu\eta}\right)\chi_A^P(\eta)$$

$$+\frac{H_{00}(\eta)}{\eta^{1/\nu}}-\frac{2}{\nu-2}\eta+\frac{1}{\nu-2}K_{01}(\eta), \quad \text{(B8)}$$

$$K_{01} = \int_0^{\eta} d\theta e^{-\mu\theta^{1/\mu}}$$

$$+\left(\nu\eta^{\frac{\nu-1}{\nu}}+1\right)e^{-\mu\eta^{1/\mu}}\int_0^{\eta} d\phi e^{\mu\phi^{1/\mu}} . \qquad \text{(B9)}$$

Observe that Eqs. (B1) and (B2) include all the ξ-corrections to $\tilde{\Phi}_{00}^{C}$ and $\tilde{\Phi}_{10}^{C}$. These terms are essential for the derivation of Eqs. (49) and (50).

REFERENCES

1. J. D. Kilkenny, S. G. Glendinning, S. W. Haan, B. A. Hammel, J. D. Lindl, D. Munro, B. A. Remington, S. V. Weber, J. P. Knauer, and C. P. Verdon, Phys. Plasmas **1**, 1379 (1994).
2. J. Grun *et al*., Phys. Rev. Lett. **58**, 2672 (1987); M. Desselberger *et al*., *ibid*. **65**, 2997 (1990); S. G. Glendinning, S. V. Weber, P. Bell, L. B. DaSilva, S. N. Dixit, M. A. Henesian, D. R. Kania, J. D. Kilkenny, H. T. Powell, R. J. Wallace, P. J. Wegner, J. P. Knauer, and C. P. Verdon, *ibid*. **69**, 1201 (1992); B. A. Remington *et al*., Phys. Fluids B **5**, 2589 (1993).
3. G. Taylor, Proc. R. Soc. London Ser. A **201**, 192 (1950); Lord Rayleigh, *Scientific Papers* (Cambridge University Press, Cambridge, England, 1900), Vol. II, pp. 200–207.
4. H. J. Kull and S. I. Anisimov, Phys. Fluids **29**, 2067 (1986).
5. H. J. Kull, Phys. Fluids B **1**, 170 (1989).
6. H. Takabe *et al*., Phys. Fluids **28**, 3676 (1985).
7. S. E. Bodner, Phys. Rev. Lett. **33**, 761 (1974).
8. D. L. Book, Plasma Phys. Control. Fusion **34**, 737 (1992).
9. R. Betti, R. L. McCrory, and C. P. Verdon, Phys. Rev. Lett. **71**, 3131 (1993).
10. J. G. Wouchuk and A. R. Piriz, Phys. Plasmas **2**, 493 (1995).
11. K. O. Mikaelian, Phys. Rev. A **46**, 6621 (1992).
12. V. V. Bychkov, S. M. Golberg, and M. A. Liberman, Phys. Plasmas **1**, 2976 (1994).
13. J. Sanz, Phys. Rev. Lett. **73**, 2700 (1994).
14. A. B. Bud'ko and M. A. Liberman, Phys. Fluids B **4**, 3499 (1992).
15. R. Betti, V. Goncharov, R. L. McCrory, E. Turano, and C. P. Verdon, Phys. Rev. E **50**, 3968 (1994).
16. R. Betti, V. N. Goncharov, R. L. McCrory, and C. P. Verdon, Phys. Plasmas **2**, 3844 (1995).
17. C. P. Verdon, R. L. McCrory, R. L. Morse, G. R. Baker, D. I. Meiron, and S. A. Orszag, Phys. Fluids **25**, 1653 (1982).
18. M. Tabak, D. H. Munro, and J. D. Lindl, Phys. Fluids B **2**, 1007 (1990).
19. J. H. Gardner, S. E. Bodner, and J. P. Dahlburg, Phys. Fluids B **3**, 1070 (1991).
20. S. V. Weber *et al*., Phys. Plasmas **1**, 3652 (1994).
21. Ya. B. Zel'dovich and Yu. P. Raizer, in *Physics of Shock Waves and High-Temperature Hydrodynamic Phenomena*, edited by W. D. Hayes and R. F. Probstein (Academic Press, New York, 1966), Vol. I, p. 152.
22. L. Spitzer, Jr. and R. Härm, Phys. Rev. **89**, 977 (1953).

Design and Implementation of the OMEGA Power Conditioning Executive

A significant amount of hardware was added to OMEGA to upgrade it to a 30-kJ, 60-beam laser. To control this hardware, an entirely new control system was implemented. This article describes one of the core subsystems of that control system—the Power Conditioning Executive.[1] Timing and control of the electrical energy fed to OMEGA's amplifiers are provided by the power conditioning system comprising state-of-the-art, high-power electrical switching components that are centrally controlled by a workstation linked to distributed sets of 218 embedded processors, one per amplifier. In this article we review this important subsystem of the OMEGA control system, beginning with a "black box" view of its role in the overall control system and proceeding with an in-depth review of the subsystem itself and its major components.

Laser Control System Overview

The OMEGA laser control system is an entirely new design, based in part on the previous OMEGA system in terms of overall requirements and system concepts. The new system makes use of both centralized and distributed control concepts. Central control is provided by a series of Sun SPARC workstations, each running an individual "executive" process that controls one aspect of the laser or diagnostic subsystems. As shown in Fig. 65.26, the primary executives are Power Conditioning, Alignment, Shot Supervisor, Facility Interlock, Laser Drivers, and Experimental (target irradiation and fusion diagnostics). Executive processes are interconnected via Ethernet using TCP/IP.[2] In the following sections, we will describe the power conditioning subsystem (Fig. 65.27), while a future article will review the entire control system design. Additional design details are available in the OMEGA Control System Design Document (CSDD)[3] and the OMEGA System Operations Manual.[4]

Power Conditioning Subsystem

As illustrated in Fig. 65.28, the power conditioning subsystem is organized vertically into the following components: executive [Graphical User Interface (GUI), state engine, status display, timing interface, etc.], local operating network (LON)/LON to Ethernet network adaptor (LON/LENA) interface, power conditioning modules (PCM's). The PCM's are the main control interface to the power conditioning units (PCU's), which contain the pulse-forming networks that supply electrical energy to the laser amplifiers. This article discusses the control software for this portion of the system. For details of the timing system, the PCU's, or the PCM's, consult the CSDD and related design documents.[5–7]

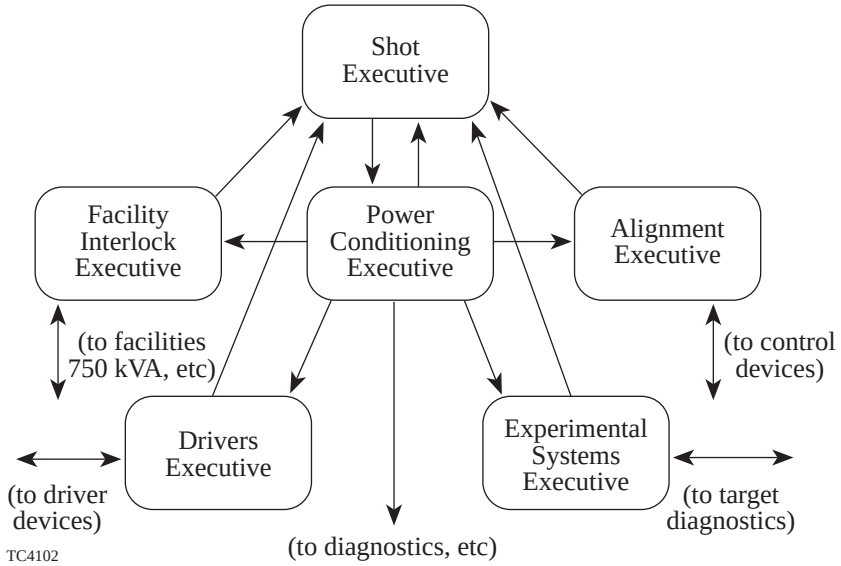

Figure 65.26
The laser control system is distributed over several *executives* that are interconnected via Ethernet using TCP/IP. Each executive performs or oversees one aspect of the laser operation and interacts with its associated devices.

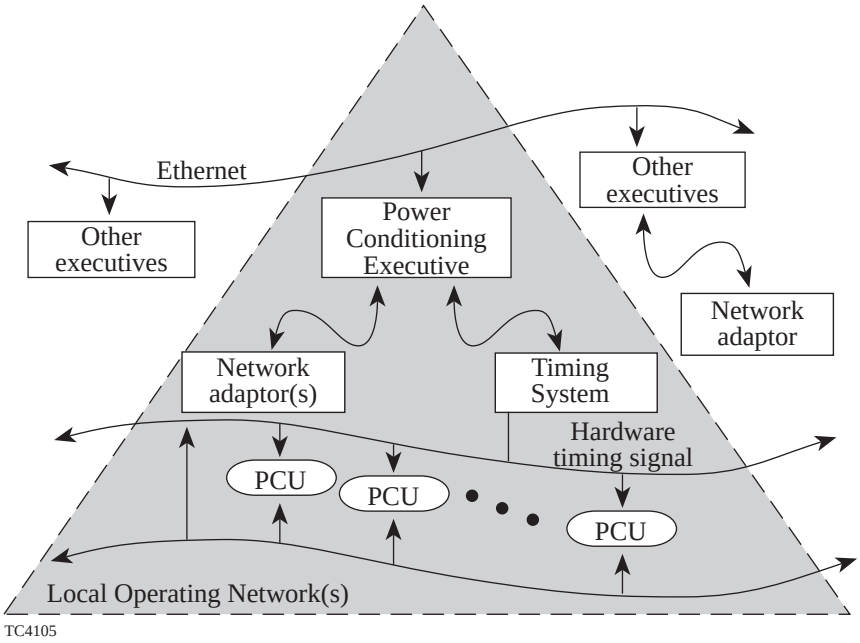

Figure 65.27
Power conditioning is one subsystem of the OMEGA laser control system. It operates as a unit to control individual power conditioning units (PCU's) but also interacts with the other OMEGA executives via Ethernet communication.

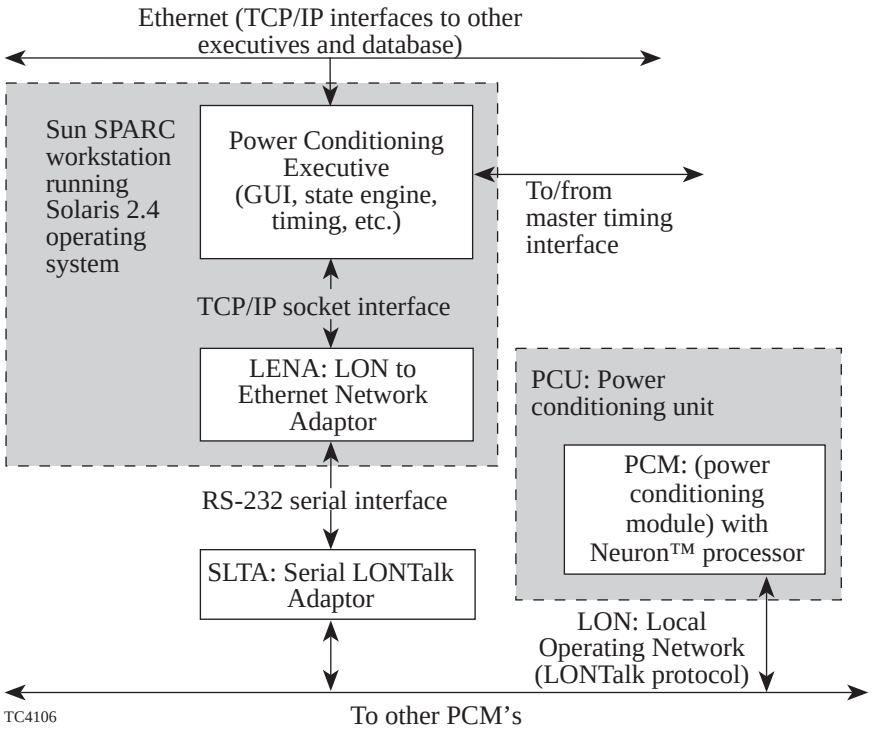

Figure 65.28
The power conditioning subsystem is distributed vertically into executive, mid-level, and low-level processors. This organization facilitates both modular code development and reusability. The local operating network (LON) is a proprietary network (hardware and protocol) that connects the Neuron™-based power conditioning modules (PCM's) to the executive via the mid-level processors (LENA's and SLTA's). Each LENA/SLTA combination provides access to up to 40 PCM's.

1. Power Conditioning Executive (PCE)

In addition to providing the central control for power conditioning, the Power Conditioning Executive (PCE) subsystem also establishes and implements the "shot sequence" for the entire laser system. As shown in Fig. 65.29, this subsystem comprises several interconnected subprocesses whose functions are to operate the laser in a safe and predictable manner.[8] These subprocesses all run on a single multiprocessor Sun SPARC workstation under the Solaris 2.4 operating system. The majority of the code was developed using the C++ object-oriented programming language,[9] though some subprocesses and libraries were developed using ANSI standard C[10] for convenience in device interfacing or reusability. In addition, the PCE has an X-based status display that was developed using low-level X libraries for optimal display speed.

The Graphical User Interface is a separate process, written in C, utilizing the UIM/X Graphical User Interface builder to construct the X/Motif interface. It will be discussed in a later section.

a. State engine. The heart of the PCE is a general-purpose state engine that is programmed with the transition network illustrated in Fig. 65.30. The transitions are caused by messages that can be received from the user interface, another executive, or the PCE itself, in the case of *automatic* (self-initiated) transitions.[11] For speed and simplicity, the state and transition lists are stored in fixed-size arrays rather than linked lists. This state engine has been generalized for reuse in the other executives.

b. Message queue. The messages that cause state transitions in the PCE are generally queued in a first-in first-out (FIFO) message queue that operates asynchronously with the state engine. An exception is made for abort messages, which cause all pending messages to be dequeued, thus placing the abort at the head of the queue for immediate processing. The message-queue subprocess has also been generalized into a library for reuse in other executives. It includes both a simple command line and a text-based interface for use with the independent GUI process.

c. Status display. Amplifier status information can be displayed on one or two workstations using an X window to show the charge status for 218 PCU's, the interface states, countdowns, system parameters, errors, and other information regarding the current state of the power conditioning. This display is maintained by a subprocess of the PCE and is independent of the GUI used for operator control of the PCE. The status display is illustrated in Fig. 65.31.

d. Timing system interface. Critical to the control of the power conditioning system is its interface to the OMEGA master timing system—the synchronization reference for the laser system. This system provides essential timing signals that are phase locked to the laser oscillator (an Antares™ cw mode-locked laser) whose 78-MHz master timing clock is the

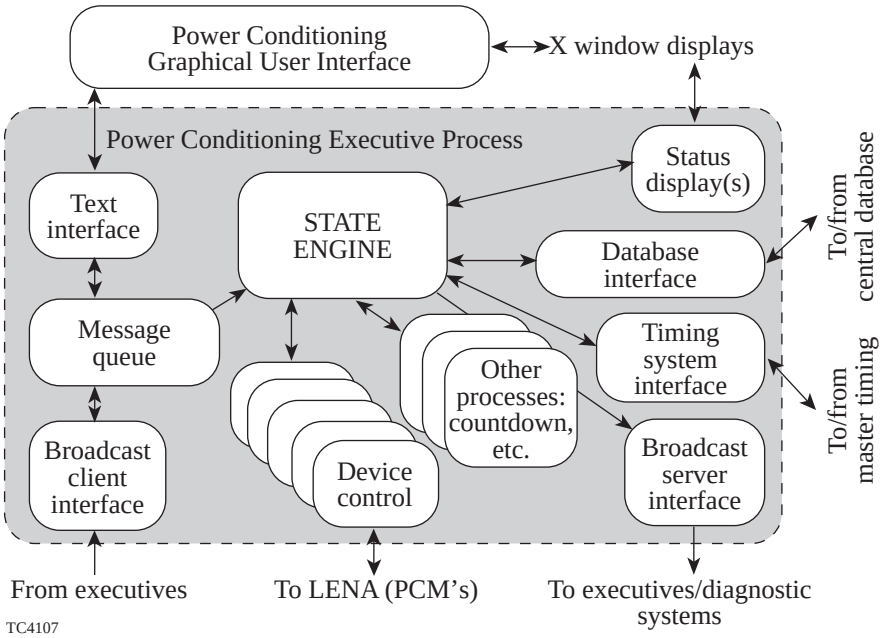

Figure 65.29
The Power Conditioning Executive Subprocesses exist within the executive computer and are composed of both *lightweight* and normal processes. For example, the Graphical User Interface (GUI) is a separate (normal) process, while the state engine and the message queue are examples of *lightweight* processes within the PCE process.

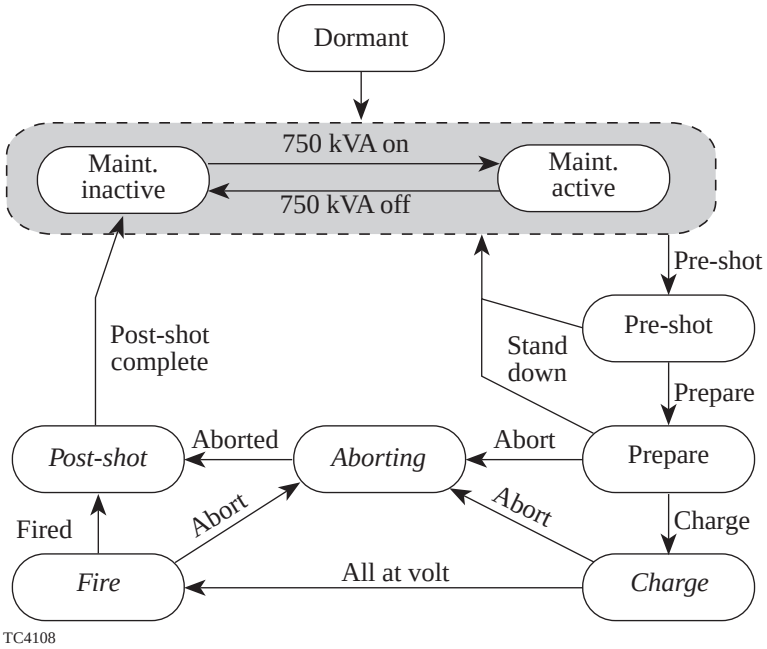

Figure 65.30
The Power Conditioning Executive is fundamentally a *state engine* with several states and transitions related to the shot sequence of the laser system.

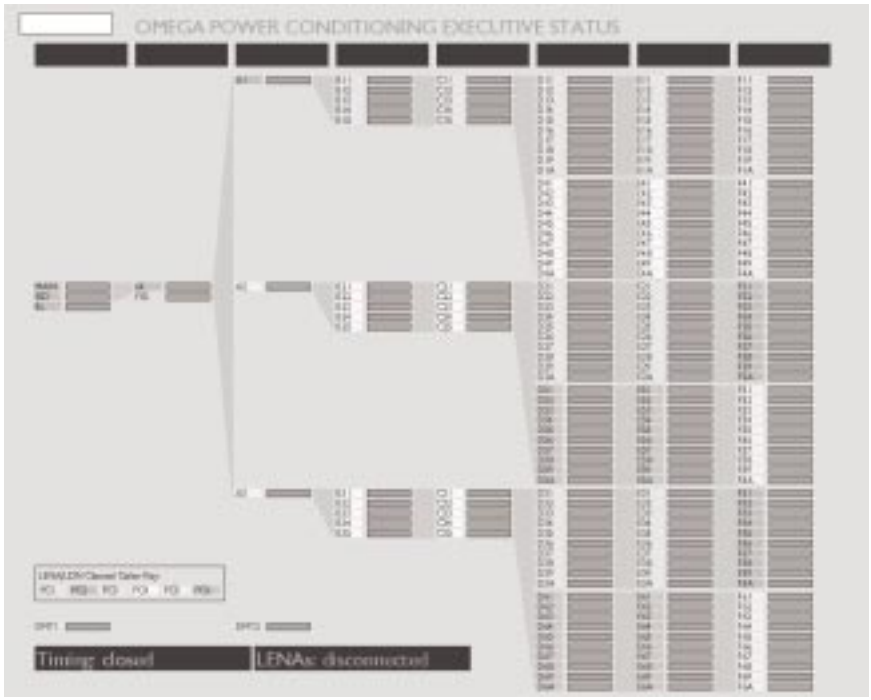

Figure 65.31
The Power Conditioning Executive status display shows the operator the current status of each power conditioning unit (PCU), including its current voltage and error status during charge, as well as the countdown to the shot.

reference for the entire system. This allows all events that occur during the operation of the laser to be properly synchronized to the occurrence of the ~1-ns laser pulse. Without this precise synchronization, the laser system and its diagnostics could not operate.

The interface to the timing system allows the Power Conditioning Executive to synchronize itself to the timing system and to initiate and control the shot sequence. The timing system provides the PCE with a 0.1-Hz signal via the timing interface hardware illustrated in Fig. 65.32. To execute a laser

shot, the PCE initiates and monitors the charging of the system capacitors. Once all capacitors are charged, the PCE waits for a 0.1-Hz signal and then enables the *T minus 10* event; this signals the preparation of many diagnostic subsystems for the shot. On the next 0.1-Hz signal (which is *T minus 10*), the PCE enables the *T equals 0* event—the actual shot, which will occur exactly 10 s later. Both the *T minus 10* and *T equals 0* events are referenced by electrical signals that are fiber optically coupled to numerous hardware devices, including the PCU's that initiate the firing of the amplifiers. These devices use the enable signals from the PCE to discriminate which of the 0.1-Hz pulses is the actual shot.

e. Database interface. The PCE is interfaced to an Ingres database that stores the post-shot data and maintains the various shot counters. A *Database Log Number* (*DBL#*) is incremented for all shots or aborts, and counters are used to keep track of the various shot types. The database keeps a precise record of the number of shots on each of the ~7000 flash lamps in the system, allowing for periodic maintenance in a timely manner. The post-shot data logged to the database can be used to review the amplifier performance on any shot, or to perform statistical analysis of amplifier performance over time. In addition, post-shot reports are generated from the database using this information, as well as other diagnostic data that are stored in the database after the shot.

An early version of the PCE used a separate process called the *Data Manager* to communicate with the database. This was necessary because of an incompatibility between the multithreaded PCE and the database API. Recent updates to the database system have allowed this functionality to be merged directly into the PCE, resulting in a significant improvement in performance as well as simplicity and reliability. The database API has been written in ANSI C for compatibility with a variety of other applications.

f. Broadcast. To support inter-executive communication (over Ethernet via TCP/IP), several libraries and subprocesses have been developed. One important implementation is the "broadcast" subprocess that allows any number of other executives or diagnostics to "listen" to messages from another executive, in this case the PCE. The PCE broadcasts state transitions, the shot countdown, and other shot-related information such as the type of shot and the database log number. In addition to these messages, the PCE transmits an empty message every few seconds as a "heartbeat" to allow other processes to verify that the PCE is still operating. This is performed to insure constant control of the high-voltage power-conditioning system.

g. LENA interface. Much of the lower-level functionality of the power conditioning subsystem is performed by the power conditioning units (PCU's), each of which contains a power conditioning module (PCM) that in turn contains a Neuron™[13] control device. These Neurons™ communicate via a proprietary network protocol called LONTalk™.[14] To communicate with the Neuron™ devices, the PCE and other executives make use of a process called the LON Ethernet network adaptor (LENA). This process was developed as part of the OMEGA Upgrade Project and can operate either on an IBM PC or SPARC workstation. As suggested by its name, the LENA acts as an interface between the proprietary network protocol of the Neurons™ and the Ethernet protocol (TCP/IP), which is used by the executives. (Six LENA's are used by the PCE to contact six distinct LONTalk networks among which the 218 PCM's are distributed.)

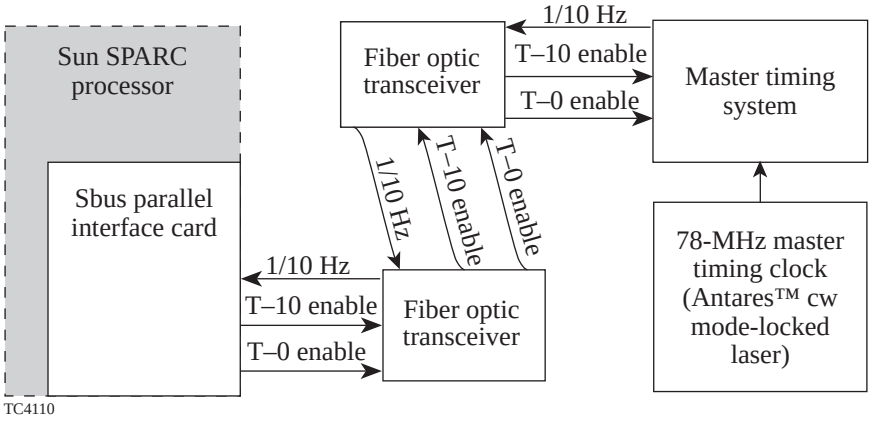

Figure 65.32
The interface to the timing system allows the Power Conditioning Executive to synchronize itself with the timing system and to initiate and control the shot sequence.

The LENA is composed of several parts, as illustrated in Fig. 65.33. The executive API (application programmer's interface) was developed in C++ and is directly accessed from the executive (PCE). It communicates, via TCP/IP sockets, with the LENA process, which may run on the same or another computer. The LENA process has a master loop that watches for either executive requests or asynchronous Neuron™ responses and relays these requests and responses to the appropriate destination. The LENA communicates with the LON via the manufacturer-supplied API, which was ported to Solaris at LLE for use on OMEGA. The LENA process was also developed using C++.

2. Power Conditioning Graphical User Interface (GUI)

One part of the message-queue system of the PCE is a command-line interface that is used mainly for development. In operation, the PCE is accessed via a Graphical User Interface. This GUI acts as a "front end" to the PCE, so that for operators, this is the only interface to the PCE. The GUI (illustrated in Fig. 65.34) has buttons for selecting state transitions as well as displays of the current database log number, the time, the elapsed time since the previous shot, the state of the enable lines, and the countdown. In addition, a scrolling window displays the text output from the PCE, and an option button allows the operator to select various procedures that are not part of the basic shot sequence.

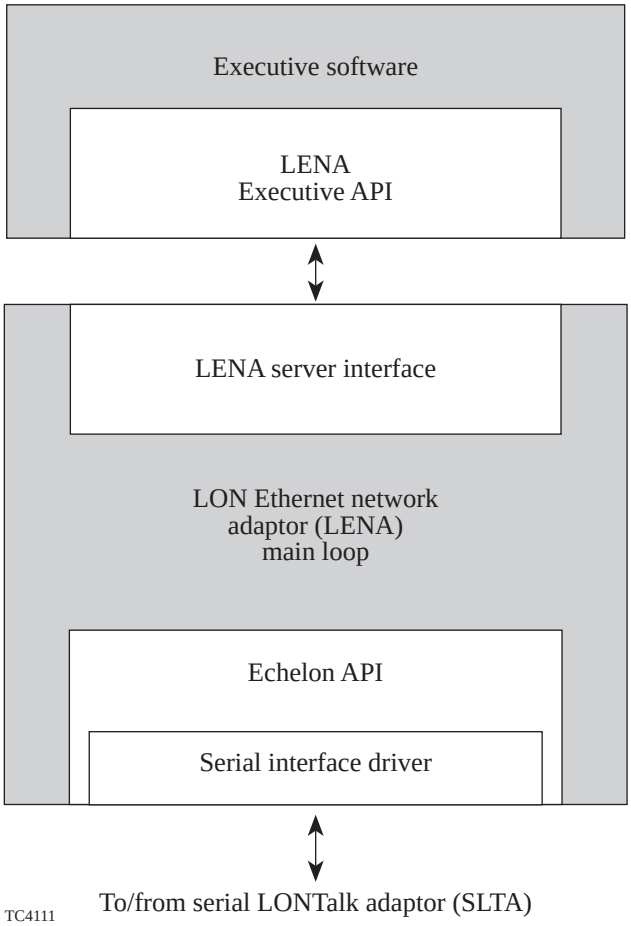

Figure 65.33
The LON Ethernet network adaptor (LENA) is a critical mid-level component in the control system, which connects the executives with the Neuron™ networks.

This Graphical User Interface was developed using the UIM/X Graphical User Interface Builder, which constructs the X/Motif user interface. Call-back procedures for the various buttons and windows were written in ANSI C.

The *look and feel* of this interface conforms with the standards established for the OMEGA executive processes. These standards were meant to create an aesthetic, functional, and uniform interface that will allow system operators to move comfortably to the various control executives, thus supporting a cross-training philosophy basic to OMEGA operations.

The Power Conditioning Executive workstation is equipped with two monitors so that both this GUI and the previously described status display are presented simultaneously to the operator.

3. Power Conditioning Unit (PCU)

As mentioned, each amplifier is equipped with a power conditioning unit (PCU) that is responsible for charging and discharging the capacitors for the execution of a shot. On a shot, the PCU first charges its associated capacitors to the requested voltage and then holds that voltage until the command is given to discharge into the flash lamps. The charge profile, holding parameters, various delay times, etc., are preprogrammed into the PCU and are constantly monitored during the shot sequence by the power conditioning module (PCM) and its Neuron™ processor. Deviations from expected performance are identified and acted on to insure safe, reliable operation of the system.

a. Power conditioning module (PCM). Each PCM contains one Neuron™ processor that is pre-programmed with the PCM firmware and is controlled by the PCE. The firmware performs all of the tasks outlined above and was written in a variation of the C programming language called Neuron C™. In addition to the normal C constructs, Neuron C includes several features for handling event-driven processes. These events are related to state changes in several hardware I/O lines

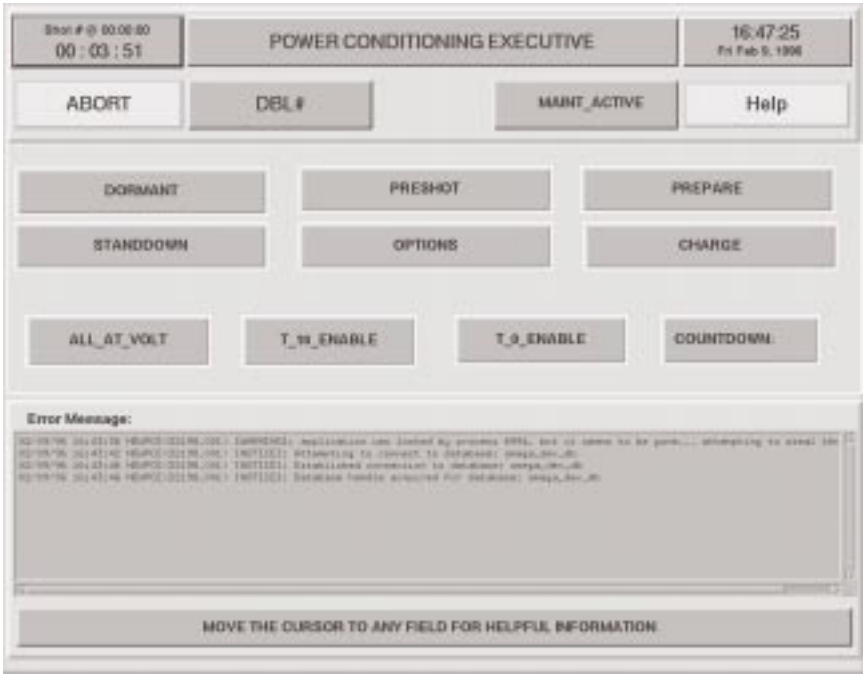

TC4112

Figure 65.34
The Power Conditioning Graphical User Interface provides access to the executive for the power conditioning operator. This screen illustrates many of the standard features of the OMEGA control system's GUI's, including a clock, time since last shot, and abort and help buttons.

and interfaces, or are related to the state of the so-called "network variables" that are used to communicate information between the Neurons™ and the executive.

4. Shot Sequence

All of the hardware and software systems described thus far have a single purpose—to fire the laser. A laser shot is a carefully orchestrated sequence through system states that charges and discharges the PCU's, then propagates a laser pulse. It requires precise and flawless operation of 218 amplifiers. The entire sequence takes about 5 min and is repeated every 30 to 60 min. A variety of shot types are possible, but all shots (assuming there is no abort) follow the sequence illustrated in Fig. 65.35.

The normal intershot state is called "maintenance."[15] It can be either "maintenance active," meaning that the 750-kVA power supply is turned on, or "maintenance inactive," meaning that the supply is off. The 750-kVA power is controlled by the facility interlock executive (FIE), which provides most of the top-level safety interlock control functions. The PCE uses the broadcast system to communicate with the FIE to determine the state of the 750-kVA power. The PCE can request 750-kVA power be turned on but cannot progress to the shot sequence until the FIE has turned on the 750 kVA.

a. Pre-shot. The shot sequence begins with the pre-shot state during which the "shot template" is loaded. This template contains a list of the amplifiers to be used and all of their relevant shot parameters, including charge voltages, various thresholds, and the required trigger delays.[16] This information is displayed in the scrolling window on the GUI and is also available for individual amplifiers on the status display. Selected amplifiers on the status display show black; nonselected amplifiers are blue.

At this stage, if the operator or shot director notices some problem with the shot, it is possible to terminate the shot sequence without an abort. No data is logged to the database, and the database log number is not incremented in such an event. Once the template is accepted by the operator and shot director, the sequence proceeds to the "prepare" state by pressing the "prepare" button on the GUI.

b. Prepare. In the prepare state, system configuration information (from the template) is downloaded to the Neuron™ modules (PCM's) via the LENA's. At completion of the download, the status of each amplifier on the status display will turn from black to green and then to white, indicating to the operator that the selected amplifiers are ready to charge. In this state, it is still possible to terminate the shot sequence without an abort.

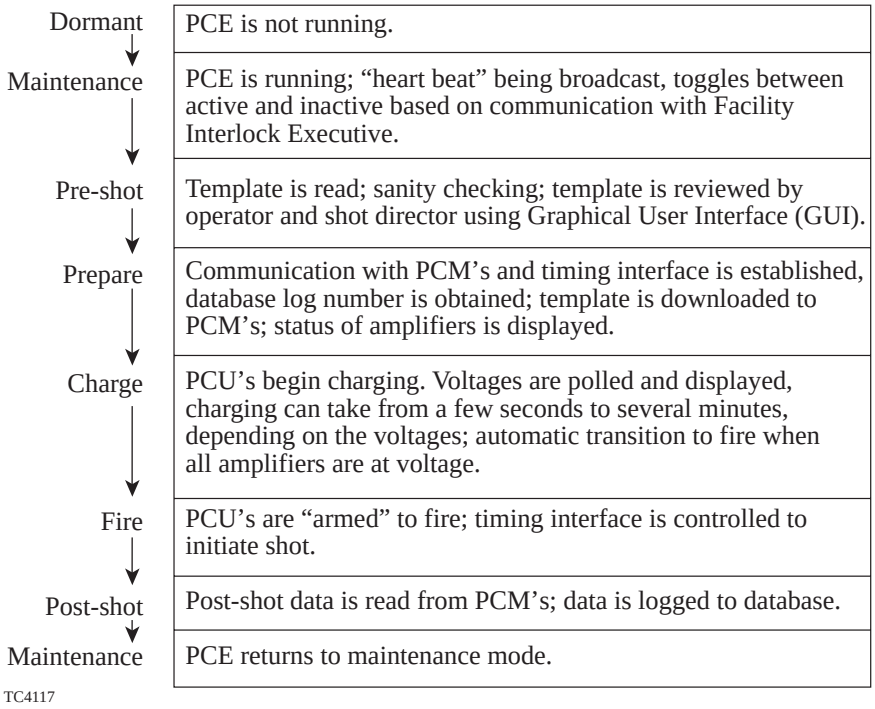

Figure 65.35
A typical OMEGA shot sequence carries the system from its dormant or maintenance state through pre-shot, prepare, charge, fire, and post-shot, and returns it to the maintenance state. In each state, various conditions must be met, and tasks performed, before proceeding to the next state. Note that this is a *typical* shot sequence. Many other transitions are possible, particularly in an **abort** condition, as illustrated in Fig. 65.30.

c. Charge. When all selected amplifiers show "ready," it is then possible to progress to the "charge" state. The operator selects "charge" from the GUI, and the amplifiers begin to charge after waiting the requested individual charge-delay times. This is the last transition in the shot sequence that is operator initiated (aside from an abort). While the capacitors charge, the PCE polls the voltages and displays a yellow bar on the status display. Minimum and maximum voltages for each amplifier stage are also displayed. When an amplifier reports "at voltage," the display bar turns green, and when all amplifiers are fully charged, the PCE automatically proceeds to the "fire" state.

d. Fire. In the "fire" state, the shot-timing sequence described previously is initiated, and a countdown is displayed on both displays. This countdown is also broadcast to any processes that may require this synchronization.

e. Post-shot. After the shot, the PCE automatically proceeds to the "post-shot" state, during which the PCM's are polled for a variety of recorded information to be logged to the database. In addition, the shot type, shot time, and other shot-related data are logged. Once data logging is complete, the PCE returns automatically to the "maintenance" state and is ready for the next shot sequence to be initiated.

5. Error Handling

In addition to the normal sequencing of the PCE, a large portion of the system is dedicated to proper handling of error conditions. Great care has been taken to ensure that the PCE will remain operational and function properly in the event of a wide variety of possible error conditions.

a. Abort. The PCE is designed to accept and respond immediately to any abort messages resulting from an unrecoverable error condition detected during the shot sequence. These may come from the user interface, another executive, or one of the subprocesses within the PCE itself. The PCE responds to an abort by first disabling the timing interface, thus preventing the shot from occurring. Next, the PCE sends an abort message to each active PCM, ceasing the charging process and dumping the charge through the emergency dump resistors. Once the system is aborted, the PCE automatically proceeds to the "post-shot" state and records much the same information that is recorded on a normal shot.

b. Casualty mode. One field in the template that is loaded at pre-shot is a "casualty mode" flag for each amplifier. If this flag is on, it indicates that a detected error on this amplifier is not to be treated as an abort condition. In this mode, the amplifier is flagged as inactive and the status display will show red, but the shot sequence will proceed for the remaining

amplifiers. This mode was added during the activation of the laser system to allow amplifiers with noncritical defects to be operated.

Future Directions

Although the PCE is used effectively for routine operation of OMEGA, many aspects of the system could be improved. Several of these areas are outlined in this section.

1. LON Throughput

Currently, the LON throughput is severely limited by various aspects of the hardware and software. This affects the ability to read certain diagnostic information from the power conditioning modules and the receipt of notifications that occur during critical shot-related events. Work is ongoing to improve this throughput at several levels.

2. Templates

On each shot, the PCE is now configured by using a so-called *flat file* that contains the voltage and timing parameters for each amplifier. Ultimately, this information will be contained in an overall *System Template*, a comprehensive description of the entire laser system configuration for each intended shot. It will be created and stored hierarchically in the Ingres database system and will include an automatic validation scheme. Much work in the coming months will be dedicated to the creation and deployment of this template system for all of the OMEGA control systems.

In addition to the power conditioning parameters, a complete description of the shot will eventually be logged at shot time. In the present implementation, much of this information is either not available to the computer or not directly available to the PCE for logging. As the templates are developed, this information will become available and will be logged at shot time. The goal is to create an electronic database that contains all pertinent information about a shot.

3. Graphical User Interfaces

Both the operator interface and the status display for the system have features that have yet to be implemented. These programs were developed using different tools and techniques and are driven from different processes within the executive. The appearance and operation of the system can be improved by merging the two into a single process and standardizing their *look and feel* using the same technique to implement them.

Conclusion

The power conditioning subsystem is central to the operation of the OMEGA laser system. The Power Conditioning Executive (PCE) and Power Conditioning Graphical User Interface (PCEGUI) are key software components that control this subsystem. Together they provide the operator interface, state engine, interprocess communication, and device control, which are essential to the operation of the laser system. The primary task of this subsystem is to perform a *shot sequence*, which entails not only the charging and firing of the laser amplifiers but also careful monitoring of the entire laser system to ensure safe and controlled operation. It is also responsible for logging shot data for later analysis.

Implemented in C/C++ and making use of X/Motif and threads, these programs take best advantage of the state-of-the-art software tools to provide an efficient and effective interface to the power conditioning hardware. Graphical User Interfaces (GUI's) make the system easy to operate and present the status of the system in an attractive and accessible format.

To perform its task, the PCE interacts continuously with a central database system, a master timing interface, other executives, and the Neuron™-based power conditioning modules (PCM's). Judicial use of *threads* (or *lightweight processes*) and interprocess communication allows these many tasks to be performed in concert with one another.

The successful deployment of this subsystem, as part of the entire OMEGA Upgrade Project, has been the work of many individuals over several years. Many more years of work remain to implement all of the desired aspects of this new OMEGA laser control system.

ACKNOWLEDGMENT

This work was supported by the U.S. Department of Energy Office of Inertial Confinement Fusion under Cooperative Agreement No. DE-FC03-92SF19460, the University of Rochester, and the New York State Energy Research and Development Authority. The support of DOE does not constitute an endorsement by DOE of the views expressed in this article.

REFERENCES

1. During its activation, the OMEGA laser achieved 40-kJ UV energy on target, matching the previous record obtained on the Nova laser at Lawrence Livermore National Laboratory.

2. TCP/IP (Transmission Control Protocol/Internet Protocol) is the prevailing standard for network communication over the Internet.

3. Definition Document: Upgrade Control System: S-AA-G-01. Laboratory for Laser Energetics, University of Rochester, September 1993.

4. OMEGA System Operations Manual—Volume I: System Description, S-AA-M-12. Laboratory for Laser Energetics, University of Rochester, February 1995.

5. Definition Document: OMEGA Upgrade Hardware Timing System: B-BU-R-02. Laboratory for Laser Energetics, University of Rochester (unreleased).

6. Specification—Power Conditioning Controls for the Rod and Disk Amplifiers of the OMEGA Upgrade: C-PC-G-01, Rev. B, Laboratory for Laser Energetics, University of Rochester, May 1992.

7. Computer Program Design Document—PCU Control Module: C-PC-F-01, Rev. A, Laboratory for Laser Energetics, University of Rochester.

8. Many of these subprocesses are threads, also known as lightweight processes. These threads are tightly coupled but asynchronously executing processes within a single program and are implemented using Sun's multithreaded Solaris operating system API.

9. B. Stroustrup, *The C++ Programming Language*, 2nd ed. (Addison Wesley, Reading, MA, 1991).

10. B. W. Kernighan and D. M. Richie, *The C Programming Language*, 2nd ed. (Prentice Hall, Englewood Cliffs, NJ, 1988).

11. Transient states are shown in italics in Fig. 65.30.

12. Previously, the database log number was known as the shot number. It is incremented on each shot or aborted shot, including "software" shots, and is used to uniquely identify information stored in the database. Other counters are also incremented depending on the type of shot.

13. The Neuron™ name is a trademark for single-chip network-based microcontrollers produced by Echelon Corporation.

14. LON stands for local operating network.

15. Note that the "dormant" state means that the PCE is not operating.

16. Each PCU fires on a pre-programmed delay relative to the T–0 trigger. In addition, each amplifier has a charge delay to allow all amplifiers to reach voltage at approximately the same time.

Upconversion and Reduced $^4F_{3/2}$ Upper-State Lifetime in Intensely Pumped Nd:YLF

Intense diode pumping of active elements doped with Nd^{3+} is a common approach to produce efficient, reliable, and compact laser systems. The high quantum efficiency of diode pumping can develop large population inversion densities in the $^4F_{3/2}$ upper level that can be lased at either 1 μm or 1.3 μm.[1,2] The upper-state lifetime τ is an important parameter for engineering such lasers since it affects the achievable stored-energy density for a given pumping scheme and ultimately determines the output energy of the laser. The long $^4F_{3/2}$ upper-state lifetime of Nd:YLF (~520 μs for 1-at.% doping[3,4]) makes it an attractive laser material.

Figure 65.36 depicts several energy-transfer mechanisms active in Nd:YLF that can reduce the effective $^4F_{3/2}$ upper-state lifetime, including concentration quenching and energy-transfer upconversion (ETU). Concentration quenching, or self-quenching, of the upper-state lifetime[5–7] is a well-known cross-relaxation process that limits the benefits of increased dopant levels in Nd:YLF. Close-range multipole or quantum mechanical exchange interactions between ions in the $^4F_{3/2}$ upper state and $^4I_{9/2}$ ground state result in two excitations at intermediate energy levels. The rate of additional loss from the $^4F_{3/2}$ upper state introduced by self-quenching generally increases linearly with dopant concentration. It is shown in this work that significant reductions in the effective upper-state lifetime also result from ETU processes at high population inversion in Nd:YLF. ETU, also known as nonlinear self-quenching, is analogous to self-quenching except interactions between two ions in the $^4F_{3/2}$ upper state promote one ion to a higher-lying energy level at the expense of demoting the other ion to a lower level. In this case, the additional loss rate from the upper state is proportional to the square of the excited-state ion density.

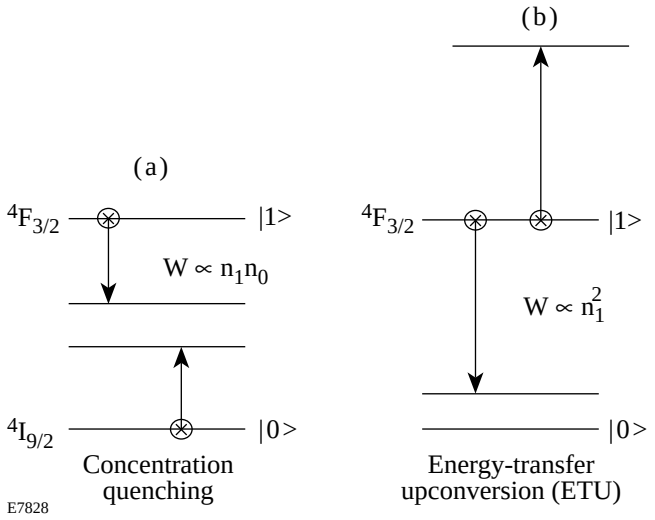

Figure 65.36
Energy-transfer processes introduce additional losses that reduce the effective $^4F_{3/2}$ upper-state lifetime. (a) Concentration quenching rates depend on ground state population densities, n_0, which are equal to doping concentrations under typical operating conditions. (b) Energy-transfer upconversion (ETU) rates depend on the square of the excited-state population density, n_1^2.

In this work, high population inversions are achieved by directly pumping from the ground state into the $^4F_{3/2}$ upper state with an intracavity-pumping arrangement in a tunable, pulsed Cr:LiSAF laser shown in Fig. 65.37. The approximately 1.4-mm-thick, uncoated Nd:YLF sample is placed inside the cavity at Brewster's angle with the pump laser polarization matching the stronger π-polarization absorption[4] in the range of approximately 855 to 885 nm. TEM_{00} mode operation is accomplished with an intracavity aperture in the nearly hemispherical cavity. Typical *Q*-switched pulse lengths were approximately 200 ns (FWHM).

Both a 1053-nm small-signal-gain probe beam and fluorescence, collected at both 1047 and 1053 nm, are used to monitor the population dynamics of the pumped sample. The small-signal-gain probe beam is focused to an approximately 50-μm spot in the center of the pumped region and measured with an amplified silicon diode (Thorlabs PDA150). A 1053±1 nm (FWHM) interference filter and a 2-mm-thick piece of RG-1000 filter glass, along with a small aperture, are used to pass only the 1053-nm probe beam. The small-signal gain is used to measure the absolute $^4F_{3/2}$ upper-state population achieved, given the effective stimulated emission cross section[8] $\sigma_{1053} = 1.9 \times 10^{-19}$ cm^2. The 1-μm fluorescence from the sample is

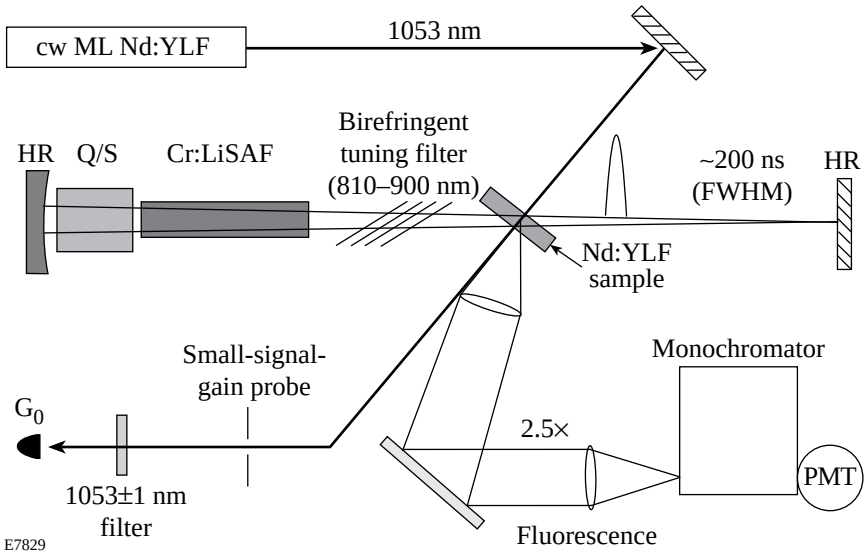

Figure 65.37
An intracavity pumping scheme achieves high population inversions in Nd:YLF. Q/S–Pockels cell *Q*-switch; HR–high-reflector mirrors; PMT–photomultiplier tube; G_0–amplified silicon diode.

collected and imaged onto a 400-μm pinhole to sample approximately the same volume as the small-signal-gain probe. The fluorescence is measured using an S-1 photomultiplier tube (Hamamatsu R5108), cooled to ~0°C, and fitted with a 1051±7.5 nm (FWHM) interference filter and a 2-mm-thick piece of RG-1000 filter glass. Upconversion fluorescence is collected and imaged onto the 250-μm entrance slit of a 1/4-m Jarrel-Ash monochromator and measured using an uncooled, multi-alkali photomultiplier tube (Hamamatsu R928). The 2.5× magnification of the imaging/collection optics effectively samples a 100-μm width around the center of the pumped region.

Figure 65.38 shows the time evolution of the $^4F_{3/2}$ upper-state population normalized to the doping concentration, $n = N/N_{\mathrm{Nd}}$, after intense pumping with an ~200-ns (FWHM) *Q*-switched pulse. At early times when large population inversions exist, there is a strong departure from the simple exponential decay that ultimately occurs at long times and lower inversions. Higher time-resolution measurements show a rapid initial decay consuming approximately 10% of the initial population for times shorter than approximately 10 μs. The horizontal dashed line in Fig. 65.38, representing the approximate maximum upper-state populations achieved in typical flashlamp-pumped Nd:YLF lasers, illustrates that the nonexponential decay associated with the two-body ETU process is observed only at inversion densities typical of intensely diode-pumped lasers.

An ETU loss channel from the $^4F_{3/2}$ upper state is confirmed in the inset to Fig. 65.38, which illustrates upconversion fluorescence measured at approximately 530 nm under similar conditions. Visible fluorescence is also observed near 591 and 665 nm with similar decay dynamics. The long duration and nonexponential nature of this upconversion fluorescence are consistent with several predicted two-body ETU processes[9] that promote ions from the $^4F_{3/2}$ upper-state population to the higher-lying $^4G_{7/2}$ and $^2G_{9/2}$ manifolds. Since the lifetimes of these latter states are very short ($\tau < 10$ ns), no

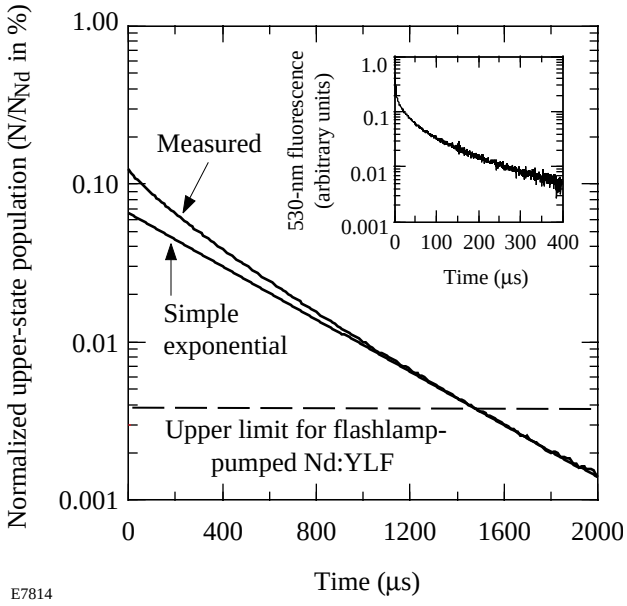

Figure 65.38
Measured population decay of the $^4F_{3/2}$ upper state normalized to the dopant ion concentration. Inset: Visible upconversion fluorescence decay measured under similar experimental conditions.

significant population accumulates in these levels and the resulting fluorescence reflects the ETU rate. The rapid decrease in upconversion fluorescence at early times ($t < 10\ \mu s$) is interpreted as static ETU, while the longer, nonexponential decay is associated with both migration-assisted ETU and the underlying fluorescence decay of the $^4F_{3/2}$ upper state.

Static and migration-assisted ETU can be differentiated by analyzing the nonexponential decay of the $^4F_{3/2}$ upper-state population in coordinates specific to each regime. Following the approach in Ref. 10, the observed decay $n(t)$ is transformed to $\left[n_0 \exp\left(-t/\tau\right)/n(t)\right]-1$ to remove the underlying fluorescent lifetime τ and plotted in Fig. 65.39 versus the coordinates for static and migration-assisted regimes, $\mathrm{erf}\left(\sqrt{t/\tau}\right)$ and $1-\exp\left(-t/\tau\right)$, respectively. The linear relationship for the migration-assisted coordinates is consistent with migration-assisted nonlinear self-quenching of the $^4F_{3/2}$ upper state predicted from the energy-transfer microparameters calculated in Ref. 9. The departure from linearity near the origin in Fig. 65.39 is attributed to the initial phase of static ETU.

The $^4F_{3/2}$ upper-state decay dynamics in Fig. 65.38 can be transformed into a more familiar "rate equation" form

$$\frac{dn}{dt} = -n/\tau - \alpha n^2 - \ldots \qquad (1)$$

by plotting the time derivative dn/dt at each time of the decay versus its corresponding population n. The linear term in Eq. (1) represents the fluorescence lifetime of the $^4F_{3/2}$ upper state, including both radiative and nonradiative decay, and concentration quenching, if present. Quadratic and higher-order terms can be included to represent energy-transfer upconversion processes that consume two or more units of excitation per interaction. A two-body ETU process is included in Eq. (1), as indicated by the quadratic dependence on upper-state population. Normally, the quadratic term would include a factor of 2 to account for the two excitations lost for each ETU interaction; however, for Nd:YLF, ions promoted to higher energy levels rapidly decay back to the $^4F_{3/2}$ upper state by nonradiative processes. Figure 65.40 graphically displays the decay dynamics of Eq. (1) along with a quadratic curve fit that best represents the transformed decay data. The $\tau = 523\ \mu s$ fluorescence lifetime derived from this curve fit matches very well the published values[3,4] for 1-at.% Nd:YLF, while the quadratic coefficient $\alpha = 1.0 \times 10^{-16}$ cm^3/s yields the macroscopic, two-body energy-transfer upconversion coefficient.

The effect of ETU processes on energy storage in Nd:YLF when operating at high population inversions can be estimated by evaluating the "relative" quantum efficiency[5] of the $^4F_{3/2}$ upper state, defined as

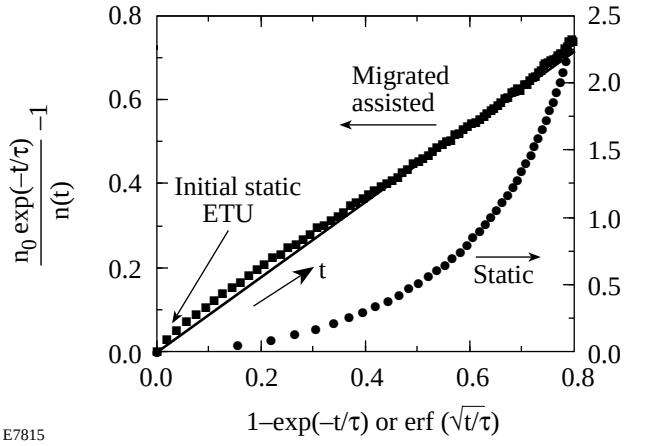

Figure 65.39
The linear dependence of the $^4F_{3/2}$ upper-state decay plotted versus $1 - \exp(-t/\tau)$ indicates migration-assisted ETU. Measurements are equally spaced ($\Delta t = 10\ \mu s$) with time increasing from left to right. An initial phase of static ETU causes the measured plot to depart slightly from Eq. (3), which is also plotted using measured values for α, τ, and n_0.

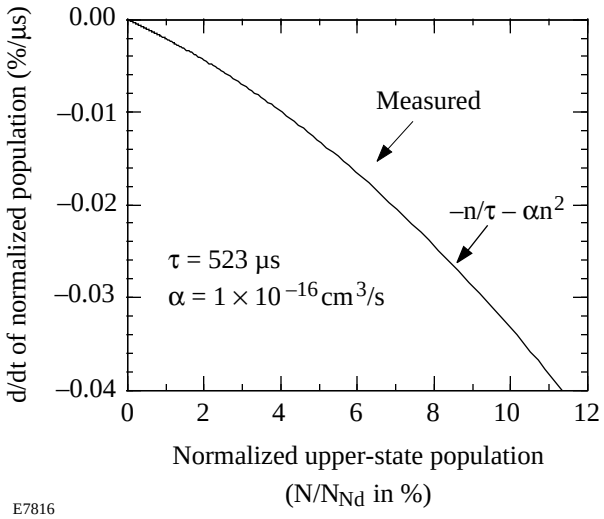

Figure 65.40
Rate equation form for $^4F_{3/2}$ upper-state population decay dynamics shows the quadratic nature of the energy-transfer upconversion (ETU) process active at high population inversions.

$$\eta_{\text{rel}} = \frac{1}{\tau}\int_0^{\infty} \frac{n(t)}{n_0}\,dt, \tag{2}$$

where τ is the fluorescence lifetime. The relative quantum efficiency compares the fluorescence yield of a sample with an initial population n_0 to that expected in the absence of energy transfer. The analytic solution to Eq. (1),[10]

$$n(t) = \frac{n_0 \exp\left(-t/\tau\right)}{1+\alpha\,\tau\,n_0\left[1-\exp\left(-t/\tau\right)\right]} \tag{3}$$

can be substituted into Eq. (2) and integrated to obtain an analytic expression for the relative quantum efficiency

$$\eta_{\text{rel}}\left(n_0\right) = \frac{\ln\left(\alpha\,\tau\,n_0+1\right)}{\alpha\,\tau\,n_0}, \tag{4}$$

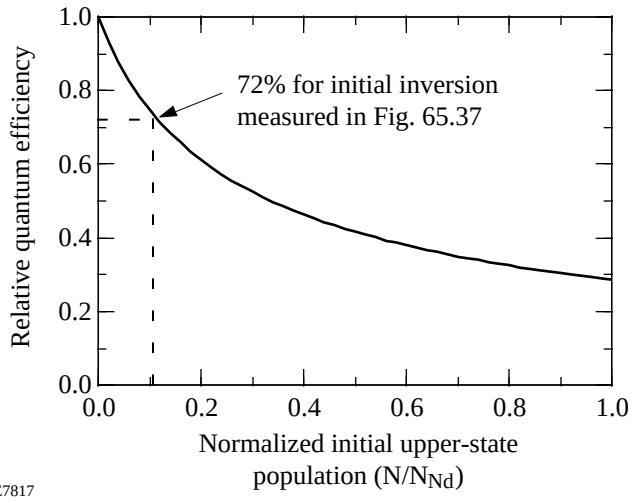

Figure 65.41
Relative quantum efficiency of Nd:YLF under intense pumping calculated using Eq. (4).

which is plotted in Fig. 65.41 using the experimental values for α and τ. A large penalty due to the ETU losses is seen for normalized $^4F_{3/2}$ upper-state populations greater than a few percent. For the experimental conditions in Fig. 65.39, these losses would reduce the relative quantum efficiency to 72%. It should be emphasized that this analysis underestimates the effect of ETU losses since Eq. (1) does not represent well the rapid initial decay due to static ETU or the likely onset of strong three-body ETU processes at high $^4F_{3/2}$ upper-state populations. On the other hand, the above analysis overestimates the effect of the ETU losses on energy storage in real laser systems since it compares the relative importance of ETU processes to fluorescence over an infinite period. An analytical form for storage efficiency[1] appropriate for pumping pulsed lasers is complicated by the nonlinear nature of the $^4F_{3/2}$ upper-state decay dynamics, requiring numerical calculations to evaluate the fraction of pump energy stored in the upper state at the end of a finite pumping period.

ETU losses also negatively impact cw laser performance in active elements operated at high population inversion threshold densities, n_{th}. These losses must be accounted for in an effective saturation intensity,

$$I_{\text{sat}} = h\nu/\sigma\tau_{\text{eff}} = h\nu/\sigma \times \left(1/\tau + \alpha n_{\text{th}}\right),$$

which increases linearly with threshold inversion. Since threshold power is proportional $\left(P_{\text{th}} \propto I_{\text{sat}}\right)$ and slope efficiency is inversely proportional $\left(\eta_{\text{slope}} \propto 1/I_{\text{sat}}\right)$ to the saturation intensity, these important laser operating parameters are adversely affected by increasing threshold densities. Using the experimental values for α and τ in 1-at.% Nd:YLF, a fractional threshold inversion of only 1% increases the effective saturation intensity by more than 7% over its value with no ETU losses.

Increased ETU rates should be observed as the doping concentration increases for several reasons. First, the macroscopic, two-body ETU coefficient, α, increases with doping concentration in the migration-assisted regime since more dopant ions are present on which to migrate. Second, the higher excited-state population densities achievable in higher doped materials and the strong dependence of energy-transfer rates on inter-ion separation lead to an increased contribution of static ETU.

In conclusion, a nonlinear loss channel from the $^4F_{3/2}$ upper state caused by two-body energy-transfer upconversion has been observed in intensely pumped Nd:YLF samples. This loss channel significantly degrades the energy storage capacity and increases the threshold power of Nd:YLF lasers operating at high population inversions.

ACKNOWLEDGMENT

The authors wish to acknowledge Lightning Optical Corporation for providing the Nd:YLF samples and M. A. Noginov for useful discussions. This work was supported by the U.S. Department of Energy Office of Inertial Confinement Fusion under Cooperative Agreement No. DE-FC03-92SF19460 and the University of Rochester.

REFERENCES

1. N. P. Barnes *et al*., IEEE J. Quantum Electon. **26**, 558 (1990).
2. J. R. Lincoln and A. I. Ferguson, Opt. Lett. **19**, 1213 (1994).
3. A. L. Harmer, A. Linz, and D. R. Gabbe, J. Phys. Chem. Solids **30**, 1483 (1969).
4. J. R. Ryan and R. Beach, J. Opt. Soc. Am. B **9**, 1883 (1992).
5. V. Lupei *et al*., Opt. Commun. **60**, 59 (1986).
6. N. P. Barnes, E. D. Filer, and C. A. Morrison, to be published in the *Technical Digest of the Advanced Solid State Laser Conference*, San Francisco, CA (1996).
7. A. A. Kaminskii, *Laser Crystals: Their Physics and Properties*, 2nd ed. (Springer-Verlag, Berlin, 1990), p. 328.
8. E. P. Maldonado and N. D. Vieira, Jr., Opt. Commun. **117**, 102 (1995).
9. A. M. Tkachuk, Opt. Spectrosc. (USSR) **68**, 775 (1990).
10. M. A. Noginov, H. P. Jenssen, and A. Cassanho, in *OSA Proceedings on Advanced Solid-State Lasers*, edited by A. A. Pinto and T. Y. Fan (Optical Society of America, Washington, DC, 1993), Vol. 15, pp. 376–380.

A New Ti:Sapphire Laser System: A Source of Femtosecond Pulses Tunable from Ultraviolet to Infrared

The availability of reliable, solid-state laser sources that produce femtosecond pulses with energies of about 1 mJ and repetition rates of 1 kHz provides new prospects for ultrafast laser spectroscopy. The Ti:sapphire oscillator/amplifier system is such a source. Nonlinear optical conversion of its output frequency using optical parametric generation/amplification or sum and difference frequency mixing effectively extends the spectral range available for femtosecond optical experiments. At LLE/COI, several UR faculty members are working to produce a multiuser laser system that will generate femtosecond pulses tunable through the visible and a large portion of the infrared. Such a system will be used for experiments in materials research, nonlinear optics, atomic and plasma physics, electronic devices, and circuits testing. In this article we describe the layout of the system under development, the main components and their characteristics, and the applications of the system. We also present the first experimental results produced at this facility.

System Configuration

A Ti:sapphire oscillator/chirped-pulse-amplification system—comprising an oscillator, stretcher, regenerative amplifier, and compressor—is the source of sub-100-fs pulses in the 800-nm spectral range with 1- to 5-kHz repetition rate. Figure 65.42 shows the layout of this system. The amplifier output is used to pump three devices: a white-light continuum generator (WLC), an optical parametric amplifier (OPA), and a terahertz (THz) radiation source. The continuum generator produces femtosecond pulses in the visible and near-infrared. Its output may serve as both a probe beam in ultrafast pump-probe experiments and a seed for the optical parametric amplifier. The output of the OPA lies in the near-infrared range ($\lambda = 1.2$ to 2.4 μm). The signal and idler waves out of the OPA are mixed in the difference frequency generator (DFG), producing tunable femtosecond pulses in the mid-infrared range (up to 12 μm and possibly longer wavelengths). The output of Ti:sapphire oscillator also pumps the optical parametric oscillator (OPO) that produces signal and idler waves covering the range between 1.35 and 2.0 μm. The OPO output can also be mixed in a difference frequency generator giving femtosecond pulses in the mid-infrared range at a repetition rate of 82 MHz.

Ti:Sapphire Oscillator/Amplifier

The core of this system is a Ti:sapphire oscillator/amplifier combination manufactured by Spectra Physics Lasers in collaboration with Positive Light. The oscillator is a regeneratively

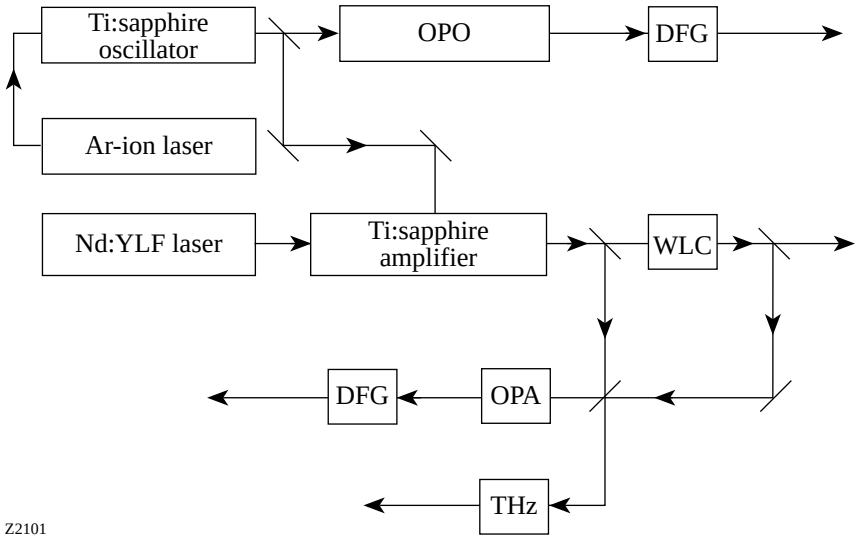

Figure 65.42
General layout of the femtosecond Ti:sapphire-based laser system. OPO—optical parametric oscillator; OPA—optical parametric amplifier; WLC—white-light continuum generator; DFG—difference frequency generator; THz—terahertz radiation generator.

mode-locked Tsunami (model 3960),[1] pumped by 8 to 12 W from an Ar-ion laser, and produces pulses at 82-MHz repetition rate. Typical pulse duration at the laser output is 70 to 80 fs, but, using an external prism compressor, pulses as short as 45 fs can be obtained [Fig. 65.43(a)]. The spectral width (FWHM) of the oscillator output is typically 15 to 17 nm [Fig. 65.43(b)]. Currently, the Tsunami tuning range is 720 to 850 nm and the output power is about 1 W. To pump the optical parametric oscillator, which requires higher pump power levels, the Ti:sapphire oscillator cavity is reconfigured to deliver up to 2 W of average power and slightly longer pulses (90 to 100 fs).

Part of the Ti:sapphire oscillator output is split off to seed the amplifier—a Spitfire, from Spectra Physics Lasers and Positive Light. The amplifier utilizes the chirped-pulse-amplification technique,[2] where the seed pulses are first stretched to about 150 ps in a diffraction-grating stretcher to reduce nonlinear effects and avoid damage to the optical elements in the amplifier and, at the same time, to allow efficient energy extraction from the amplifier. These temporally expanded pulses are switched into a regenerative amplifier cavity. The Ti:sapphire amplifier is pumped by a Nd:YLF *Q*-switched laser (Merlin, from Spectra Physics Lasers and Positive Light), which is capable of producing up to 12 W of average power at 527 nm (200- to 300-ns pulses at 1 kHz). After 15 to 20 roundtrips through the amplifier cavity, amplified pulses are switched out and contain 1 to 1.5 mJ per pulse (the repetition rate is that of the pump laser—1 kHz). Following this amplification, the pulses are compressed to 75 to 140 fs in the diffraction-grating compressor [Fig. 65.43(a)], depending on the seed pulses' characteristics. The energy per pulse is up to 1 mJ at 1-kHz repetition rate (i.e., 1-W average power) when operating near 800 nm with a pulse-to-pulse energy stability of ~2%. The amplifier is also capable of higher repetition rates—up to 5 kHz, producing up to 1.5 W of average power.

White-Light Generator

To perform time-resolved spectroscopic measurements (pump-probe experiments) in a broad spectral range, we utilize the technique of femtosecond continuum (or supercontinuum) generation. Femtosecond pulses out of the Ti:sapphire amplifier are focused onto a plate of glass or crystalline material. For pump intensities above a certain threshold, broadband radiation spanning the entire visible and a portion of near-infrared range is produced at the output of the plate. A number of mechanisms are involved in continuum generation, the major being spectral broadening of the pulses due to self-phase modulation.[3] The generation of femtosecond continuum requires materials with a high nonlinear refractive index and resistance to damage at very high intensities. We tested a number of glass and crystalline materials and, based on a compromise between efficient continuum generation in the near-infrared and resistance to optical damage, we selected BaF_2 crystals. The threshold for continuum generation in a BaF_2 plate of 5-mm thickness was about 1 to 2 μJ per pulse (the pump radiation was focused onto the crystal using 20-cm-focal-length lens). Using a Si or Ge photodiode for detection, we observed continuum radiation spanning 400 nm to 1500 nm. Femtosecond continuum was also generated using the second harmonic ($\lambda = 400$ nm) of a Ti:sapphire system; the output is in the visible-ultraviolet spectral range. For the pump-probe measurements, portions of the continuum in the spectral range of interest are selected using bandpass interference filters. The duration of probe pulses produced in this manner is nearly that of the pump pulses (~100 fs).

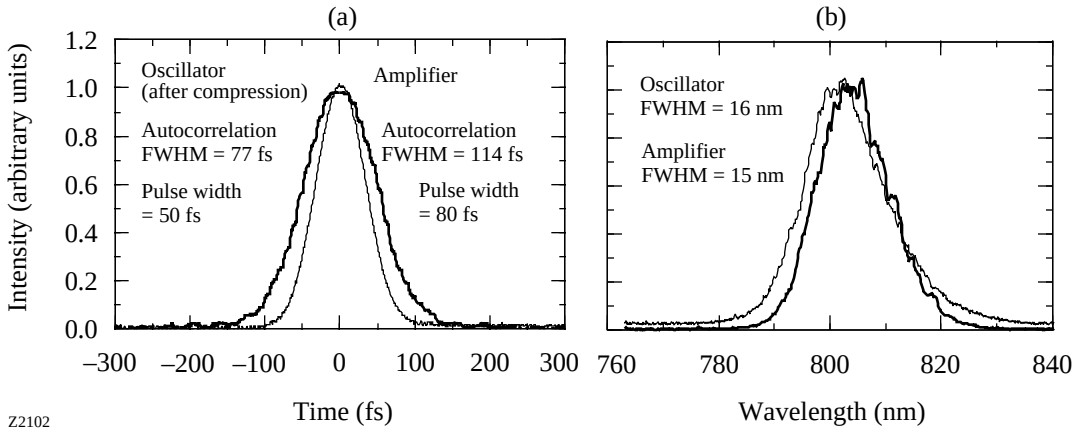

Figure 65.43
(a) Intensity autocorrelation functions and (b) spectra of the Ti:sapphire oscillator (thin line) and regenerative amplifier (thick line).

Although it is easy to implement, femtosecond continuum generation over a broad spectral range has certain limitations. First, the intensity of the continuum drops rapidly when moving away from the pump wavelength. The useful spectral range in the infrared is limited to 1.3 to 1.5 μm when pumped by pulses centered at 800 nm. Second, the intensity of the continuum may be too low for many applications. To produce intense, tunable femtosecond pulses in a broad spectral range, we use the optical parametric amplification technique and subsequent difference frequency mixing.

Optical Parametric Amplifier and Difference Frequency Generator

To generate femtosecond pulses in the 1.2- to 2.5-μm range we are developing a traveling-wave optical parametric amplifier that is seeded by pulses from the white-light continuum generator.[4] Seeding the OPA with femtosecond continuum pulses allows operation at lower pump levels (as compared to the optical parametric generator/amplifier configuration, which utilizes parametric fluorescence as the seed) and leads to more reliable and stable operation. Our OPA is based on a BBO crystal, which combines high second-order nonlinearity and high damage threshold. In the first experiment, we used a 7-mm-thick BBO crystal cut for type-II phase matching to reduce the bandwidth of the OPA output and to generate pulses that are closer to the transform limit than in the case of type-I phase matching. This also provides signal and idler waves of orthogonal polarizations that are convenient for subsequent difference frequency mixing. (Phase matching in a $AgGaS_2$ difference frequency generator requires orthogonally polarized input waves.) The layout of the two-pass, single-crystal OPA is shown in Fig. 65.44. The output of the white-light continuum generator and the pump radiation at 810 nm are collinearly combined in the nonlinear crystal using a dichroic mirror. The white-light seed is not spectrally filtered before the OPA since the nonlinear crystal, with its limited wavelength acceptance bandwidth, is a natural spectral filter. The central wavelength is selected by angular tuning of the OPA crystal. The first-pass OPA output is backreflected onto the crystal and is again combined collinearly with a fresh portion of the 800-nm pump using a dichroic mirror. The temporal overlap between the pump and seed (first pass), and the pump and the signal wave (second pass) is adjusted by two optical delay lines. When 100-μJ pulses were used to pump the first pass and 200 μJ for the second pass, the OPA output was more than 40 μJ per pulse (total output in signal and idler beams). Figure 65.45 is a demonstration of the tunability from degeneracy down to 1.2 μm (signal wave) and up to 2.4 μm (idler). The spectral width of the OPA output is about 25 nm FWHM (signal wave), which is enough to support pulses shorter than 100 fs. In the first experiments, the pump-pulse duration was 140 fs, and measurements of the cross correlation between the OPA output and the pump pulses indicated an OPA output pulse duration of about 200 fs. The excessive pulsewidth of the OPA output is most likely a result of a group-velocity mismatch between the interacting waves. For three-wave type-II interaction in BBO the group-velocity mismatch is calculated, using Sellmeier equations,[5] to be about 80 fs/mm. The crystal length in our OPA should, therefore, be reduced to optimize performance.

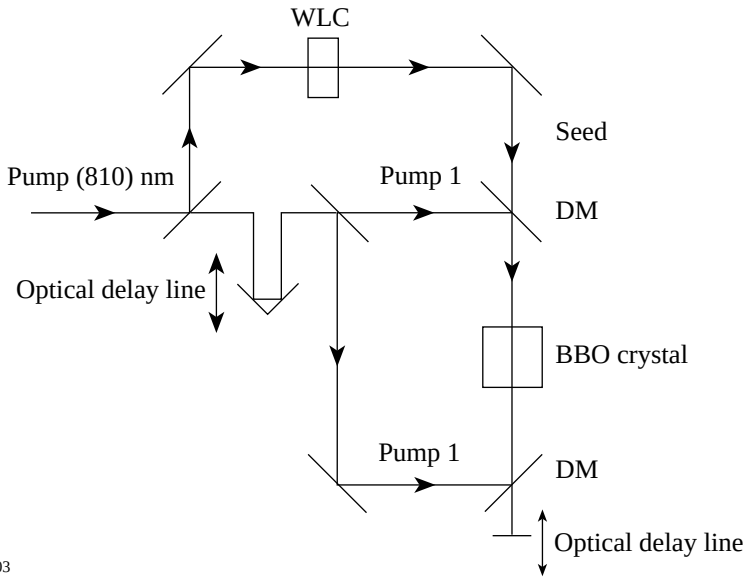

Figure 65.44
Optical parametric amplifier layout. WLC—white-light continuum generator; DM—dichroic mirror.

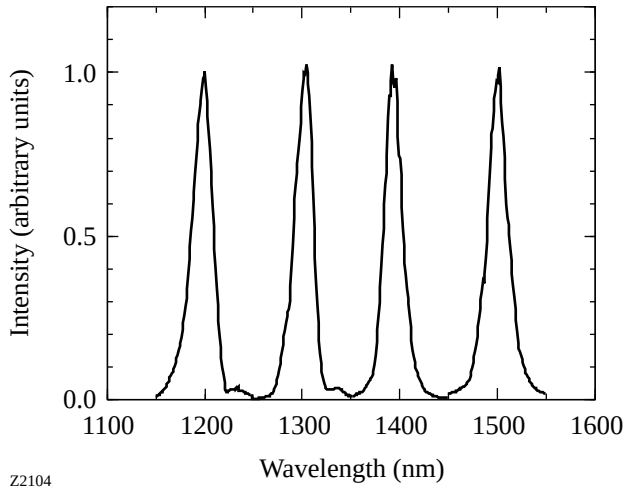

Figure 65.45
The spectrum of the OPA output.

To generate femtosecond pulses in the mid-infrared range, the signal and idler waves from the OPA are mixed in a difference frequency generator (Fig. 65.46 shows the expected tuning range of the DFG). A 1-mm-thick $AgGaS_2$ crystal, which is transparent up to 12 μm, was used for difference frequency mixing. With 30 μJ per pulse input (signal and idler) more than 300 nJ per pulse was obtained at 5-μm wavelength. The spectral width of the mid-infrared pulses was about 200 nm—sufficient to produce pulses as short as 130 fs.

It is worth mentioning that the OPA output pulses are of sufficient energy to generate femtosecond continuum in solid-state media. This continuum can be a broadband source of femtosecond pulses in the near- and mid-infrared that presents new possibilities for ultrafast spectroscopy in this range.

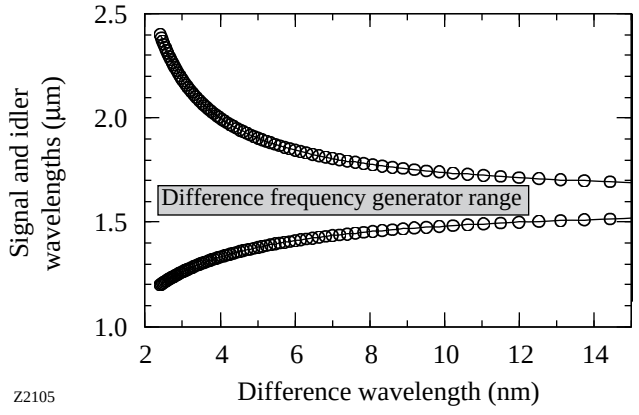

Figure 65.46
Tuning range of a difference frequency generator pumped by the OPA output.

The demonstrated performance of the OPA and DFG has already allowed several interesting time-resolved experiments to be performed in the near- and mid-infrared ranges. Work continues on the optimization of conversion efficiency and pulse durations.

Optical Parametric Oscillator

Femtosecond pulses in the near-infrared region at a high repetition rate (82 MHz) can be produced using a synchronously pumped optical parametric oscillator—OPAL, manufactured by Spectra-Physics Lasers. The OPAL is based on a temperature-tuned noncritically phase-matched LBO crystal and is capable of delivering pulses of about 100-fs duration in the spectral range of 1.35 to 1.6 μm (signal wave) and 1.6 to 2.0 μm (idler wave). (The wavelength is determined by the spectral characteristics of the OPAL cavity mirrors.) When pumped by about 2 W of average power from a Ti:sapphire oscillator, the OPAL produces an output of more than 250 mW (signal) and about 150 mW (idler) at the maximum of its tuning curve (signal wave at around 1.45 to 1.50 μm). A typical spectrum and an autocorrelation function of the OPAL output are shown in Fig. 65.47.

Mixing the signal and idler beams in the difference frequency generator can produce mid-infrared femtosecond pulses from 4 to 12 μm. Using a 1-mm-thick $AgGaS_2$ crystal for difference frequency mixing, up to 50 μW of average power was generated in the 4- to 10-μm range. In this range, group-velocity mismatch between interacting waves (signal, idler, and difference) in $AgGaAs_2$ does not exceed 200 fs/mm, so the difference frequency pulses out of the 1-mm-thick crystal should not be longer than 200 fs when the input signal and idler pulses are 100 fs long.

THz Radiation Generator

Work is currently underway to produce ultrashort pulses of terahertz radiation (the sub-millimeter range of the spectrum). A high-power source of terahertz radiation, called a large-aperture photoconducting antenna,[6,7] consists of a 6-cm^2 GaAs wafer that is biased using parallel electrodes spaced 2 cm apart. Semi-insulating GaAs is used to hold off a bias voltage of 10 kV. When a high-energy Ti:sapphire pulse uniformly illuminates the antenna, electrons are excited into the conduction band and the antenna becomes conductive. The sharp turn-on of surface current produces radiation that is polarized along the bias-field direction. In the far field, the radiated electric field is proportional to the rate of change of the surface current, the bias field, and the energy of the optical

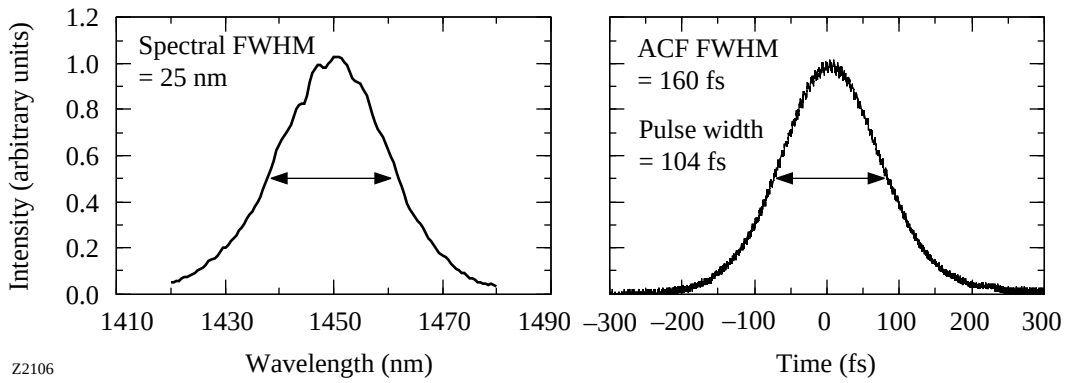

Figure 65.47
Spectrum and intensity autocorrelation function of the OPAL output pulses (signal wave).

pulse. The large-aperture design permits the use of high bias voltages and optical powers without damaging the antenna.

The THz radiation from this source is in the form of a beam of subpicosecond pulses. A 100-fs, 400-mJ Ti:sapphire pulse can produce a 450-fs, 0.8-mJ THz pulse.[6] The unique feature of these THz pulses is that the pulse duration is less than the period of the electric field oscillation. Thus, it does not have a carrier wave in the usual sense. For this reason the pulses are sometimes referred to as dc pulses or half-cycle pulses.[8]

The short-term goal is to measure the spatial and temporal characteristics of such THz pulses. Of particular interest are the effects of diffraction and focusing on the pulse shape, and improvement of the shot-to-shot noise when the antenna is saturated. A variety of techniques will be used to do this. Initially, the temporal profile of the pulses will be studied by passing the THz beam through a time-gated mirror and measuring the transmitted or reflected energy. The mirror consists of a second GaAs wafer that is illuminated by a delayed Ti:sapphire pulse.[6,9] After absorption of the Ti:sapphire pulse, the transmission of a GaAs wafer at THz frequencies can be reduced by a factor of ten.[6] Next, the power spectrum of the pulse will be measured using interferometric autocorrelation.[9] Finally, electro-optic sampling techniques[10] can be extended to freely propagating THz radiation to provide temporal and spatial information about the beam.

Once the nature of the THz pulses is better understood, work will begin on the long-term goal: the use of the THz pulses to manipulate the valence electron of a hydrogen-like atom. This type source has been used in atomic physics experiments to probe the electronic motion of highly excited (Rydberg) atoms.[8] When the duration of a directional THz pulse is shorter than the time scale of the electrons evolution, interaction between the THz pulse and an electron depends strongly on the shape of the electron wave function and its velocity. Furthermore, the large bandwidth of THz pulses enables electronic Rydberg states to be coherently coupled to neighboring states. These features may allow the use the THz pulses to excite and detect a three dimensionally localized Rydberg wave packet, which follows a circular orbit.[11]

Initial Applications of the System

Using the pulses from the Ti:sapphire amplifier and the femtosecond continuum generator, pump-probe transient-absorption measurements were performed to better understand relaxation processes in silicon-based materials, low-temperature-grown A_3B_5 semiconductors, and polymers. Here the results of these measurements are briefly described.

The first experiments were performed on porous silicon, which has attracted significant attention since the 1990 discovery of its efficient light emission.[12] Normally, crystalline silicon does not emit light since it is an indirect band-gap material, but porous silicon, formed by electrochemical etching of crystalline silicon, luminesces effectively. Photoluminescence in the blue through near infrared has been observed, and light-emitting devices have been demonstrated.[13] However, the energy structure of porous silicon and the origin of its efficient luminescence are still under debate. Time-resolved photoinduced absorption measurements (on a femtosecond scale) can be useful in clarifying the energy structure, determining the carrier relaxation mechanisms, and identifying the role of quantum confinement and defect states in porous silicon. Toward this end, pump-probe measurements on porous silicon, crystalline silicon (c-Si), and hydrogenated amorphous silicon (a-Si:H) samples have been conducted.

The porous Si sample was a 1-μm-thick mesoporous film lifted off and attached to a sapphire window. The c-Si sample was epitaxially grown on sapphire and was 530 nm thick. The a-Si:H sample was deposited on a glass window by RF glow discharge and was 320 nm thick. For these experiments, amplified Ti:sapphire pulses were frequency doubled to 3.06 eV (405 nm) to allow excitation of carriers across the band gap in the investigated samples. The probe was a portion of the white-light continuum, selected by a bandpass filter, and had a mean photon energy of 1.43 eV (870 nm).

Figure 65.48 shows the typical photoinduced absorption changes in the three samples. The traces for the porous Si and c-Si samples are similar to each other: both exhibit the increase in absorption when excited by 405-nm pulses; a short-lived (less than 1-ps decay constant) induced absorption peak decays into a "plateau." Longer time scans show that this plateau decays in hundreds of picoseconds. The initial peak is consistent with two-photon absorption—the simultaneous absorption of a pump and a probe photon across the direct band gap of silicon. The plateau in the induced absorption results from free-carrier absorption. That the dominant effect is induced absorption (as opposed to bleaching) is an indication of the indirect-band structure of porous silicon; in direct-gap semiconductors the dominant effect in the spectral range above the band gap is bleaching related to the filling of states. Based on our experimental results, we also estimated the free-carrier absorption cross section for the three silicon-based materials.

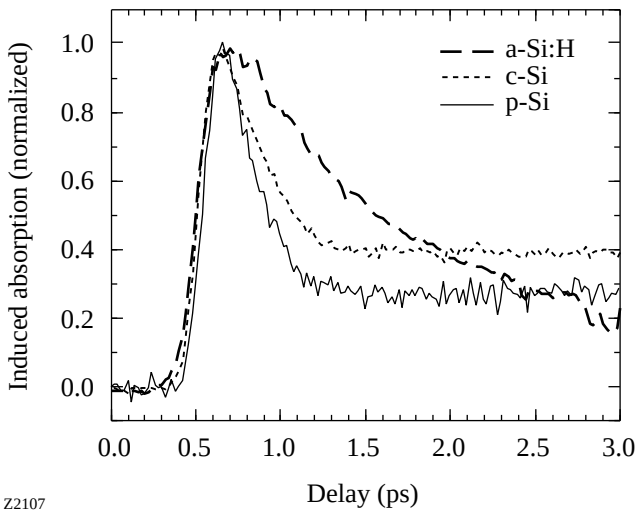

Figure 65.48
Time-resolved photoinduced absorption in porous, crystalline, and amorphous Si.

The cross-section for porous Si (1.2×10^{-18} cm^2) is close to that of crystalline Si (2.2×10^{-18} cm^2) and much smaller than that of amorphous Si (8×10^{-17} cm^2). This is evidence that porous Si is made of an ordered lattice of Si atoms. By varying the excitation intensity we observed changes in the induced absorption decay rate. In porous silicon, the rapid decay (less than 1.5-ps lifetime) of the photoinduced free-carrier absorption was observed. Its time constant, which is nearly pulsewidth limited at low intensity, increases to about 1.5 ps as the pump intensity is increased. In porous silicon, this fast component probably originates from photoinjected carrier trapping by dangling bonds at the surface of silicon crystallites. Reduction of its decay rate is due to the saturation of the surface trapping states. These measurements show that trap saturation takes place at an injected carrier density of about 10^{18} cm^{-3}. The "slowly" decaying component of the induced absorption signal is due to carrier recombination through nonradiative Auger processes. The Auger mechanism of recombination is evidenced by the characteristic speeding up of the final stage of the absorption recovery when the pump intensity is increased.[14]

These initial photoinduced absorption experiments with the Ti:sapphire laser system provided information about the energy structure of porous silicon and carrier relaxation mechanisms in that material.

Another set of measurements was performed with GaAs grown by molecular-beam epitaxy at low substrate temperatures. Low-temperature (LT)-grown A_3B_5 semiconductors have recently attracted considerable interest due to their extremely rapid optical response times (several picoseconds). Initially, this fast response was attributed to carrier recombination. Pump-probe transient absorption experiments were performed at or below the band edge of GaAs samples grown at 195°C and 250°C to check the origin of this fast response time. The pump beam wavelength was 810 nm (1.531 eV), and the probe was varied from 870 nm (1.425 eV) to 1000 nm (1.24 eV).

The 250°C sample, which behaves very much like a normally grown GaAs, exhibits bleaching in the investigated spectral range. This bleaching may be attributed to the filling of bandtail states associated with defects due to low-temperature growth. On the other hand, the 195°C sample shows initial bleaching, which recovers quickly when the probe wavelength is in the vicinity of the band edge. When the probe is tuned to longer wavelengths (>900 nm), the signal changes to induced absorption with a relative slow recovery. The slowly recovering induced absorption shows that the carriers are trapped in

states below the band gap within several picoseconds but stay there for a long time until they recombine. This indicates that the observed fast, above-the-band-gap photoresponse time is due to carrier trapping, not recombination.

The same pump-probe technique with femtosecond continuum as a source of probe pulses was also applied to study the excitation decay dynamics in PBZT—a conjugated rigid-rod aromatic polymer with promising nonlinear optical and luminescent properties. The optical absorption in PBZT rises sharply at 500 nm, so frequency-doubled pulses (405 nm) from a Ti:sapphire amplifier were used to resonantly excite the PBZT sample. Using the white-light continuum generator, the photoinduced absorption was probed over a wide spectral range (from 500 to 1000 nm) below the PBZT bandgap. A broad photoinduced absorption band was observed: the signal appeared promptly within the time resolution and decayed in several picoseconds. The experimental results are explained by a self-trapped exciton model: induced absorption is due to the transition of self-trapped excitons to higher-lying continuum states. These results provide important information for the potential nonlinear optical and light-emitting applications of PBZT.

Test pump-probe experiments were performed in the mid-infrared range using the output of the optical parametric amplifier and difference frequency generator. In one set of measurements, a semiconductor sample (InGaAs ternary compound) was excited with the OPA output at 1.4 μm, and the DFG output was used as a probe. Photoinduced absorption due to free carriers was observed at a probe wavelength of 5 μm. In another experiment, the mid-infrared output of the difference frequency generator was utilized to monitor the intersubband-hole relaxation in quantum wells (InGaAs/AlGaAs heterostructure). These measurements were performed in the degenerate pump-probe configuration at the 5-μm wavelength, resonant with the intersubband (heavy-hole to light-hole) transition. An increase of transmission (bleaching) following photoexcitation was observed (Fig. 65.49). The bleaching signal recovered with a time constant of about 0.6 ps, corresponding to the excited state (light-hole subband) lifetime.

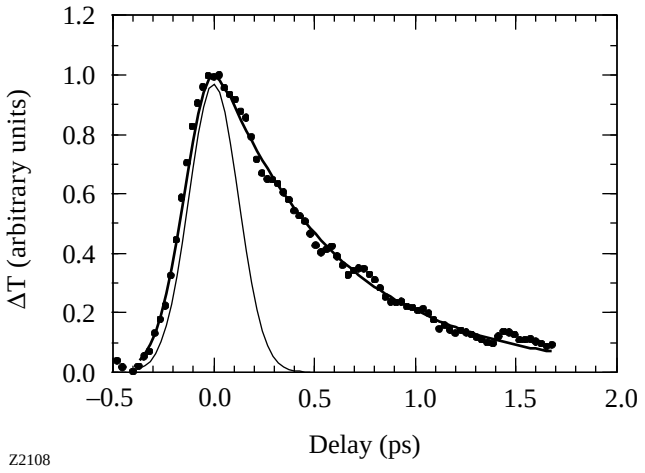

Figure 65.49
Pump-probe bleaching signal of a quantum well sample. The cross-correlation of the pump and probe pulses is shown for comparison (thin line).

Conclusions

An ultrafast Ti:sapphire laser/amplifier system has been developed and characterized. Its output has been used to produce tunable femtosecond pulses in the near- and mid-infrared range using white-light continuum generation, optical parametric amplification, and difference frequency mixing. Although further optimization of the nonlinear optical frequency converters is needed, the system is already capable of ultrafast optical experiments in the infrared range. Initial ultrafast spectroscopic experiments have been performed on a number of materials, important for both scientific and technological studies.

ACKNOWLEDGMENT

This work was supported by the National Science Foundation (Grant No. ECS-9413989).

REFERENCES

1. J. D. Kafka, M. L. Watts, and J.-W. J. Pieterse, IEEE J. Quantum Electron. **28**, 2151 (1992).
2. P. Maine, D. Strickland, P. Bado, M. Pessot, and G. Mourou, IEEE J. Quantum Electron. **24**, 398 (1988).
3. R. L. Fork *et al*., Opt. Lett. **8**, 1 (1983).
4. For a recent review of results on optical parametric amplification see J. Opt. Soc. Am. B **12**, 1995 (special issue on optical parametric devices).
5. V. G. Dmitriev, G. G. Gurzadyan, D. N. Nikogosyan, *Handbook of Nonlinear Optical Crystals* (Springer-Verlag, Berlin, 1991), p. 78.
6. D. You *et al*., Opt. Lett. **18**, 290 (1993).
7. J. T. Darrow *et al*., Opt. Lett. **15**, 323 (1990).
8. R. R. Jones, D. You, and P. H. Bucksbaum, Phys. Rev. Lett. **70**, 1236 (1993).
9. B. I. Greene *et al*., Appl. Phys. Lett. **59**, 893 (1991).
10. S. Alexandrou, R. Sobelewski, and T. Y. Hsiang, IEEE J. Quantum Electron. **28**, 2325 (1992).

11. Z. D. Gaeta, M. W. Noel, and C. R. Stroud, Jr., Phys. Rev. Lett. **73**, 636 (1994).

12. L. T. Canham, Appl. Phys. Lett. **57**, 1046 (1990).

13. Laboratory for Laser Energetics LLE Review **62**, NTIS document No. DOE/SF/19460-75, 1995 (unpublished), p. 77.

14. J. von Behren, Y. Kostoulas, K. B. Üçer, and P. M. Fauchet, to be published in the *Journal of Non-Crystalline Solids.*

Publications and Conference Presentations

Publications

R. Adam, W. Kula, R. Sobolewski, J. M. Murduck, and C. Pettiette-Hall, "Laser-Induced Modification of Transport Properties of Y-Ba-Cu-O Step-Edge Weak Links," Appl. Phys. Lett. **67**, 3801 (1995).

R. Betti, V. Goncharov, R. L. McCrory, and C. P. Verdon, "Self-Consistent Cutoff Wave Number of the Ablative Rayleigh-Taylor Instability," Phys. Plasmas **2**, 3844 (1995).

X. D. Cao and D. D. Meyerhofer, "Optimization of Pulse Shaping Using Nonlinear Polarization Rotation," Opt. Commun. **120**, 316 (1995).

S.-H. Chen, J. C. Mastrangelo, H. Shi, A. Bashir-Hashemi, J. S. Li, and N. Gelber, "Novel Glass-Forming Materials. 1. Adamantane with Pendant Cholesteryl, Disperse Red 1, and Nematogenic Groups," Macromol. **28**, 7775 (1995).

R. E. Giacone, C. J. McKinstrie, and R. Betti, "Angular Dependence of Stimulated Brillouin Scattering in Homogeneous Plasma," Phys. Plasmas **2**, 4596 (1995).

D. Eimerl, J. E. Rothenberg, M. H. Key, S. V. Weber, C. P. Verdon, S. Skupsky, J. M. Soures, and R. S. Craxton, "Configuring NIF for Direct-Drive Experiments," in the *First Annual International Conference on Solid-State Lasers for Application to Inertial Confinement Fusion*, edited by M. André and H. T. Powell (SPIE, Bellingham, WA, 1995), Vol. 2633, pp. 170–182.

K. Green, W. R. Donaldson, R. Sobolewski, A. Okishev, M. D. Skeldon, S. A. Letzring, and W. Seka, "Transient Microwave Bandwidth Measurements of Illuminated Silicon Switches for Optical Pulse-Shape Control of Laser-Fusion Drivers," in the *First Annual International Conference on Solid-State Lasers for Application to Inertial Confinement Fusion*, edited by M. André and H. T. Powell (SPIE, Bellingham, WA, 1995), Vol. 2633, pp. 615–621.

J. Hecht, D. Ofer, U. Alon, D. Shvarts, S. A. Orszag, and R. L. McCrory, "Three-Dimensional Simulations and Analysis of the Nonlinear Stage of the Rayleigh-Taylor Instability," Laser and Particle Beams **13**, 423 (1995).

S. D. Jacobs, "Nanodiamonds Enhance Removal in Magneto-rheological Finishing," Finer Points **7** (4), 47 (1995).

E. M. Korenic, S. D. Jacobs, S. M. Faris, and L. Li, "Colorimetry of Fractured Cholesteric Liquid Crystal Polymers," in the *Proceedings of the IS&T/SID Color Imaging Conference: Color Science, Systems, and Applications* (IS&T, Springfield, VA, 1995), pp. 60–62.

W. Lang, W. Göb, W. Kula, and R. Sobolewski, "Anisotropic Magnetoresistance in the Normal State of Oxygen-Deficient $YBa2Cu_3O_{7-\delta}$ Thin Films Induced by Superconducting Fluctuations," Z. Phys. B **98**, 453 (1995).

K. L. Marshall, S. D. Jacobs, and J. E. Miller, "Midinfrared Modulation through the Use of Field-Induced Scattering in Ferroelectric Liquid Crystals," Appl. Opt. **34**, 6704 (1995).

J. Peatross and D. D. Meyerhofer, "Intensity-Dependent Atomic-Phase Effects in High-Order Harmonic Generation," Phys. Rev. A **52**, 3976 (1995).

B. E. Puchebner and S. D. Jacobs, "Development of New Bound Abrasive Polishers for Final Finishing of Optical Glasses," in *Optical Manufacturing and Testing* (SPIE, Bellingham, WA, 1995), Vol. 2536, pp. 256–264.

H. Shi and S.-H. Chen, "Effects of Stereochemistry, Mesogenic Core, and Spacer Length on Crystallization from Nematic and Isotropic Melts of Cyclohexane-Based, Glass-Forming Liquid Crystals," Liq. Cryst. **19**, 785 (1995).

H. Shi and S.-H. Chen, "Novel Glass-Forming Liquid Crystals. III. Helical Sense and Twisting Power in Chiral Nematic Systems," Liq. Cryst. **19**, 849 (1995).

A. Simon, "Parametric Excitation of Bernstein Modes in Laser-Produced Plasma," Phys. Plasmas **2**, 3832 (1995).

M. D. Skeldon, A. Okishev, A. Babushkin, and W. Seka, "Transient Stimulated Brillouin Scattering Pulse Compression for Photoconductive Switch Activation," in the *First Annual International Conference on Solid-State Lasers for Application to Inertial Confinement Fusion*, edited by M. André and H. T. Powell (SPIE, Bellingham, WA, 1995), Vol. 2633, pp. 422–429.

C. J. Twomey, T. N. Blanton, K. L. Marshall, S. H. Chen, and S. D. Jacobs, "Some Dynamic Features of the Preparation of Liquid Crystalline Elastomers," Liq. Cryst. **19**, 339 (1995).

M. Yu and C. J. McKinstrie, "Impulse Response of a Nonlinear Dispersive Wave," Phys. Rev. E **52**, 6826 (1995).

J. D. Zuegel and W. Seka, "Direct Measurement of $^4I_{11/2}$ Terminal-Level Lifetime in Nd:YLF," IEEE J. Quantum Electron. **31**, 1742 (1995).

Forthcoming Publications

E. L. Alfonso, S.-H. Chen, M. D. Wittman, S. Papernov, and D. Harding, "A Parametric Study of Microencapsulation Approach to the Preparation of Polystyrene Shells" to be published in Polymer Preprints.

R. Betti, V. N. Goncharov, R. L. McCrory, P. Sorotokin, and C. P. Verdon, "Self-Consistent Stability Analysis of Ablation Fronts in Inertial Confinement Fusion," to be published in Physics of Plasmas.

T. R. Boehly, D. L. Brown, R. S. Craxton, R. L. Keck, J. P. Knauer, J. H. Kelly, T. J. Kessler, S. J. Loucks, S. A. Letzring, F. J. Marshall, R. L. McCrory, S. F. B Morse, W. Seka, J. M. Soures, and C. P. Verdon, "Initial Performance Results of the OMEGA Laser System," to be published in Optics Communications.

S.-H. Chen, J. C. Mastrangelo, and H. Shi, "Novel Low Molar Mass, Glass-Forming Liquid Crystals: Molecular Design, Synthesis, and Morphological Stability," to be published in the Proceedings of Polymers for Advanced Optical Applications.

S.-H. Chen, H. Shi, J. C. Mastrangelo, and J. J. Ou, "Thermotropic Chiral Nematic Side-Chain Polymers and Cyclic Oligomers," to be published in Progress in Polymer Science.

C. T. Cotton, "Design Considerations for the OMEGA Upgrade Final Focus Lens," to be published in the Proceedings of SPIE's 1995 International Symposium on Optical Science, Engineering, and Instrumentation, San Diego, CA.

C. T. Cotton, "The Design of an All-Spherical, Three-Mirror, Off-Axis Telescope Objective," to be published in the OSA Proceedings of the International Optical Design Conference '94, Rochester, NY.

P. M. Fauchet, L. Tsybeskov, C. Peng, S. P. Duttagupta, J. von Behren, Y. Kostoulas, J. V. Vandyshev, and K. D. Hirshman, "Light-Emitting Porous Silicon: Materials Science, Properties, and Device Applications," to be published in the IEEE Journal of Selected Topics in Quantum Electronics.

D. Fried, R. E. Glena, J. D. B. Featherstone, and W. Seka, "Permanent and Transient Changes in the Reflectance of CO_2 Laser-Irradiated Dental Hard Tissues at λ = 9.3, 9.6, 10.3, and 10.6 μm and at Fluences between 1–20 J/cm^2," to be published in Lasers in Surgery and Medicine.

V. N. Goncharov, R. Betti, R. L. McCrory, P. Sorotokin, and C. P. Verdon, "Self-Consistent Stability Analysis of Ablation Fronts with Large Froude Numbers," to be published in Physics of Plasmas.

J. H. Kelly, T. R. Boehly, J. M. Soures, D. L. Brown, R. Boni, R. S. Craxton, R. L. Keck, T. J. Kessler, R. Kremens, S. A. Kumpan, S. A. Letzring, S. J. Loucks, R. L. McCrory, S. F. B. Morse, W. Seka, S. Skupsky, and C. P. Verdon, "The Activation of the Upgraded OMEGA Laser at the University of Rochester," to be published in the SPIE Proceedings of the 15th International Conference on Coherent and Nonlinear Optics, St. Petersburg, Russia, June 1995.

O. A. Konoplev and D. D. Meyerhofer, "Dynamic Range Limitations in High-Contrast, Noncollinear Autocorrelators," to be published in Generation, Amplification, and Measurement of Ultrashort Laser Pulses III.

Y. Kostoulas, K. B. Ucer, L. Waxer, G. W. Wicks, I. A. Walmsley, and P. M. Fauchet, "Ultrafast Carrier Lifetime in Low-Temperature-Grown GaAs, InP, and InGaP," to be published in the Proceedings of LEOS '94 7th Annual Meeting, Boston, MA, 31 October–3 November 1994.

T. Kotseroglou, C. Bamber, S. Boege, U. Haug, A. C. Melissinos, D. D. Meyerhofer, W. Ragg, C. Bula, K. T. McDonald, E. Prebys, D. L. Burke, P. Chen, R. C. Field, G. Horton-Smith, A. C. Odian, J. C. Spencer, D. Walz, S. Berridge, W. Bugg, K. Shmakov, and A. Weidemann, "Studies of Nonlinear QED with an Ultra-Intense Laser," to be published in Generation, Amplification, and Measurement of Ultrashort Laser Pulses III.

W. Kula, R. Adam, and R. Sobolewski, "Y-Ba-Cu-O Thin-Film Structures with a Nonuniform In-Depth Oxygen Concentration Profile," to be published in the Institute of Physics Conference Series.

J. C. Lambropoulos, T. Fang, B. Puchebner, and S. D. Jacobs, "The Effect of Coolant Surface Tension in Deterministic Microgrinding of Glass," to be published in the International Symposium on Manufacturing Practices and Technologies, New Orleans, LA, 5–8 November 1995.

Y. Lin, T. J. Kessler, and G. N. Lawrence, "Design of Continuous Surface-Relief Phase Plates by Simulated Annealing to Achieve Control of Focal Plane Irradiance," to be published in Optics Letters.

R. S. Marjoribanks, F. W. Budnik, H. Chen, and D. D. Meyerhofer, "Plasma Electron Temperature in Picosecond Laser Plasmas from Quasi-Steady Ratio of Isoelectronic Lines," to be published in the Journal of the Optical Society of America B.

J. C. Mastrangelo, T. N. Blanton, and S.-H. Chen, "Morphology and Its Stability of Cyclohexane and Biocyclooctene Rings Containing Pendant Disperse Red 1," to be published in Chemistry of Materials.

J. C. Mastrangelo and S.-H. Chen, "Novel Glass-Forming Organic Materials. 2. Cyclohexane and Bicyclooctene with Pendant Pyrenene and Carbazole," to be published in Chemistry of Materials.

S. M. McCormack, D. Fried, J. D. B. Featherstone, R. E. Glena, and W. Seka, "Scanning Electron Microscope Observations of CO_2 Laser Effects on Dental Enamel," to be published in the Journal of Dental Research.

R. L. McCrory, J. M. Soures, C. P. Verdon, T. R. Boehly, D. K. Bradley, R. S. Craxton, J. A. Delettrez, R. Epstein, P. A. Jaanimagi, S. D. Jacobs, R. L. Keck, J. H. Kelly, T. J. Kessler, H. Kim, J. P. Knauer, R. L. Kremens, S. A. Kumpan, S. A. Letzring, F. J. Marshall, P. J. McKenty, S. F. B. Morse, A. Okishev, W. Seka, R. W. Short, M. D. Skeldon, S. Skupsky, M. Tracy, and B. Yaakobi, "Direct-Drive Laser Fusion Experimental Program at the University of Rochester Laboratory for Laser Energetics," to be published in the Proceedings of the Conference on Plasma Physics and Controlled Nuclear Fusion Research, Madrid, Spain, September 1994.

R. L. McCrory, J. M. Soures, C. P. Verdon, T. R. Boehly, D. K. Bradley, R. S. Craxton, J. A. Delettrez, R. Epstein, P. A. Jaanimagi, S. D. Jacobs, R. L. Keck, J. H. Kelly, T. J. Kessler, H. Kim, J. P. Knauer, R. L. Kremens, S. A. Kumpan, S. A. Letzring, F. J. Marshall, P. W. McKenty, S. F. B. Morse, A. Okishev, W. Seka, R. W. Short, M. D. Skeldon, S. Skupsky, M. Tracy, and B. Yaakobi, "Experiments on the OMEGA to Validate High-Gain, Direct-Drive Performance on the National Ignition Facility," to be published in the Proceedings of the 12th International Conference on Laser Interaction and Related Plasma Phenomena, Osaka, Japan, April 1995.

D. D. Meyerhofer, J. P. Knauer, S. J. McNaught, and C. I. Moore, "Observation of Relativistic Mass Shift Effects during High-Intensity Laser-Electron Interactions," to be published in the Journal of the Optical Society of America B.

D. Ofer, U. Alon, D. Shvarts, R. L. McCrory, and C. P. Verdon, "Modal-Model for the Non-Linear Multi-Mode Rayleigh-Taylor Instability," to be published in Physics of Plasmas.

A. Okishev, M. D. Skeldon, S. A. Letzring, W. R. Donaldson, A. Babushkin, and W. Seka, "The Pulse-Shaping System for the 60-Beam, 30-kJ (UV) OMEGA Laser," to be published in the Proceedings of Laser Optics '95 Conference, St. Petersburg, Russia, 27 June–1 July 1995.

S. Papernov and A. W. Schmid, "A Comparison of Laser-Induced Damage Morphology in Three Model Thin-Film

Systems: HfO_2, Y_2O_3, and Ta_2O_5," to be published in the Proceedings of the XXVI Annual Symposium on Optical Materials for High Power Lasers, Boulder, CO, 24–26 October 1994.

J. Z. Roach, A. Ninkov, S. W. Swales, and T. Morris, "Design and Evaluation of a Screen CCD Imaging System," to be published in Optical Engineering.

H. Shi and S.-H. Chen, "Dynamic Mechanical Properties of Cyclohexane-Based Glass-Forming Liquid Crystals and a Linear Side-Chain Polymer Analogue," to be published in Liquid Crystals.

A. Simon, "Comparison Between SBS Theories and Experiment," to be published in the Proceedings of the La Jolla Summer School '95, Plasma Physics and Technology (AIP).

E. J. Turano, C. J. McKinstrie, and R. E. Giacone, "One-Dimensional Stimulated Raman Scattering of Short Laser Pulses," to be published in Physics of Plasmas.

C. P. Verdon and R. L. McCrory, "Direct-Drive Capsule Physics," to be published in the Proceedings of ECLIM '94, Oxford, England, September 1994.

C.-C. Wang, M. Currie, D. Jacobs-Perkins, R. Sobolewski, T. Y. Hsiang, and M. J. Feldman, "Electro-Optic Measurements of Single-Flux Quantum Pulses," to be published in the Institute of Physics Conference Series.

M. D. Wittman, R. Q. Gram, H. Kim, C. K. Immesoete, S. G. Noyes, and S. Scarantino, "Increased Retention Time for Hydrogen and Other Gases by Polymer Shells Using Optically Transparent Aluminum Layers," to be published in the Journal of Vacuum Science and Technology.

W. Xiong, Y. Kostoulas, X. Weng, P. M. Fauchet, and R. Sobolewski, "Femtosecond Study of the Electronic Structure in Semiconducting Y-Ba-Cu-O," to be published in Physical Review B.

B. Yaakobi, D. Shvarts, R. Epstein, and Q. Qu, "X-Ray Backlighting Imaging of Mixed Imploded Targets," to be published in Laser and Particle Beams.

B. Yaakobi, R. Epstein, C. F. Hooper, Jr., D. A. Haynes, Jr., and Q. Su, "Diagnosis of High-Temperature Implosions Using Low- and High-Opacity Krypton Lines," to be published in the Journal of X-Ray Science and Technology.

B. Yaakobi, Q. Su, R. S. Craxton, and R. Epstein, "Diagnosis of Core-Shell Mixing Using Absorption and Emission Spectra of a Doped Layer," to be published in the Journal of Quantitative Spectroscopy and Radiative Transfer.

X. Zhou, S. Alexandrou, and T. Y. Hsiang, "Monte Carlo Investigation of the Intrinsic Mechanism of Subpicosecond Pulse Generation by Nonuniform Illumination," to be published in Applied Physics Letters.

J. D. Zuegel and W. Seka, "Upconversion and Reduced $^4F_{3/2}$ Upper-State Lifetime in Intensely Pumped Nd:YLF," to be published in Optics Letters.

J. D. Zuegel and W. Seka, "Direct Measurements of Lower-Level Lifetime in Nd:YLF," to be published in the Bulletin of the American Physical Society.

Conference Presentations

S. A. Letzring, "Initial Results from the Upgrade to the OMEGA Laser Facility and Plans for a Cryogenic Target System," 42nd National Symposium of the American Vacuum Society, Minneapolis, MN, 16–20 October 1995.

S. Papernov, A. W. Schmid, J. Anzelotti, D. Smith, and Z. R. Chrzan, "AFM-Mapped, Nanoscale, Absorber-Driven Laser Damage in UV High-Reflector Multilayers," XXVII Annual Symposium on Optical Materials for High Power Lasers, Boulder, CO, 30 October–1 November 1995.

J. D. Zuegel and W. Seka, "Upconversion and Reduced $^4F_{3/2}$ Upper-State Lifetimes in Intensely Pumped Nd:YLF," LEOS '95 8th Annual Meeting, San Francisco, CA, 30 October–2 November 1995.

J. C. Lambropoulos, T. Fang, B. Puchebner, and S. D. Jacobs, "The Effect of Coolant Surface Tension in Deterministic Microgrinding of Glass," International Symposium on Manufacturing Practices and Technologies, New Orleans, LA, 5–8 November 1995.

The following presentations were made at the 37th Annual Meeting, APS Division of Plasma Physics, Louisville, KY, 6–10 November 1995:

R. Betti, S. Cowley, and J. P. Freidberg, "Kinetic Effects on the Resistive Wall Mode."

T. R. Boehly, D. L. Brown, R. S. Craxton, R. L. Keck, J. P. Knauer, J. H. Kelly, T. J. Kessler, S. J. Loucks, S. A. Letzring, F. J. Marshall, R. L. McCrory, S. F. B. Morse, W. Seka, J. M. Soures, and C. P. Verdon, "Initial Performance Results from the OMEGA Laser Facility."

R. Boni, R. L. Keck, T. R. Boehly, O. R. Lopez-Raffo, S. A. Letzring and S. Scarantino, "The Energy-Balance Diagnostic for the OMEGA Laser System."

D. K. Bradley, J. A. Delettrez, P. A. Jaanimagi, and P. M. Bell, "Time-Resolved Imaging on the Upgraded OMEGA Laser System."

A. V. Chirokikh, A. Simon, W. Seka, and R. S. Craxton, "Simulations of SBS in Long-Scale-Length Laser Plasmas of Variable Density: The Inability of Linear Theory to Explain Experimental Observations."

R. S. Craxton and S. Skupsky, "Two-Dimensional SSD and Polarization Wedges for OMEGA and the National Ignition Facility."

J. A. Delettrez, D. K. Bradley, and C. P. Verdon, "Comparison of a One-Dimensional Mix Model for the Linear and Weakly Nonlinear Regime of the Rayleigh-Taylor Instability with Two-Dimensional *ORCHID* Results."

R. Epstein, J. A. Delettrez, C. P. Verdon, U. Alon, and D. Shvarts, "Simulations in One Dimension of Fuel-Pusher Mixing in Laser-Driven Implosions."

V. Goncharov, R. Betti, R. L. McCrory, and C. P. Verdon, "Self-Consistent Cutoff Wave Number of the Ablative Rayleigh-Taylor Instability."

P. Jaanimagi, R. L. Kremens, P. W. McKenty, D. K. Bradley, K. Kearney, and C. P. Verdon, "Implosion Experiments on the Upgraded OMEGA Laser."

R. L. Kremens, K. Kearney, and M. A. Russotto, "Neutron Diagnostic Implementation on the OMEGA Laser System."

R. L. Kremens, D. L. Brown, J. T. Canosa, M. Litchfield, D. Lonobile, R. G. Roides, M. Thomas, and R. Weaver, "A Precision Electronic Timing System for the OMEGA Laser System."

S. A. Letzring, R. L. Fagaly, N. B. Alexander, R. A. Mangano, and C. R. Gibson, "Cryogenic Target System for the OMEGA Laser System."

J. S. Li and C. J. McKinstrie, "Effects of the Anti-Stokes Wave on Stimulated Brillouin Scattering."

F. J. Marshall, A. Hauer, J. Oertel, and R. Watt, "Monochromatic X-Ray Imaging of Laser-Fusion Targets Using a Kirkpatrick-Baez X-Ray Microscope."

F. J. Marshall, R. L. Keck, T. R. Boehly, J. P. Knauer, S. F. B. Morse, and J. M. Soures, "Uniformity Experiments on the University of Rochester's OMEGA 60-Beam, 30-kJ, UV Laser-Fusion Facility."

P. W. McKenty, C. P. Verdon, and D. K. Bradley, "Inertial Confinement Fusion Capsule Performance Under the Influence of Long-Wavelength Illumination Nonuniformities."

C. J. McKinstrie, R. E. Giacone, and H. X. Vu, "Interaction of Crossed Laser Beams in Homogeneous Plasma."

W. Seka, R. S. Craxton, C. Labaune, H. A. Baldis, N. Renard, E. Schifano, and A. Michard, "Characterization of a Long-Scale-Length Plasma Using SRS and Thomson Scattering."

R. W. Short and R. Grobe, "Diffractive Irradiation Patterns in a Spherically Symmetric Target Corona."

A. Simon, "Ion Jets and Recent Brillouin Experiments."

J. M. Soures, R. L. McCrory, C. P. Verdon, A. Babushkin, R. E. Bahr, T. R. Boehly, R. Boni, D. K. Bradley, D. L. Brown, J. A. Delettrez, R. S. Craxton, W. R. Donaldson, R. Epstein, P. A. Jaanimagi, K. Kearney, R. L. Keck, J. H. Kelly, T. J. Kessler, R. L. Kremens, J. P. Knauer, S. J. Loucks, S. A. Letzring, F. J. Marshall, P. W. McKenty, D. D. Meyerhofer, S. F. B. Morse, A. Okishev, G. Pien, W. Seka, M. D. Skeldon, S. Skupsky, S. Swales, M. Wittman, and B. Yaakobi, "Direct-Drive Laser-Fusion Experiments with the OMEGA, 60-Beam, > 40-kJ, UV Laser System" (invited).

E. A. Startsev and C. J. McKinstrie, "Relativistic Ponderomotive Force of a Light Wave."

E. J. Turano, C. J. McKinstrie, and R. E. Giacone, "Two-Dimensional Stimulated Raman Scattering of Short Laser Pulses."

B. Yaakobi, R. Epstein, C. F. Hooper, Jr., D. A. Haynes, Jr., and Q. Su, "Diagnosis of High-Temperature Implosions Using Low- and High-Opacity Krypton Lines."

B. Yaakobi, D. Shvarts, R. Epstein, and Q. Su, "X-Ray Backlighting Imaging of Mixed Imploded Targets."

E. M. Korenic, S. D. Jacobs, S. M. Faris, and L. Li, "Colorimetry of Fractured Cholesteric Liquid Crystal Polymers," 3rd Color Imaging Conference: Color Science, Systems, and Applications, Scottsdale, AZ, 7–10 November 1995.

S.-H. Chen, J. C. Mastrangelo, and H. Shi, "Novel Low Molar Mass, Glass-Forming Liquid Crystals: Molecular Design, Synthesis, and Morphological Stability," Fourth Pacific Polymer Conference, Koloa, Kauai, HI, 12–16 December 1995.